WA School of Mines: Minerals, Energy
and Chemical Engineering

Experimental Study of Down-the-Hole Percussive Drilling

Joao Victor Borges Dos Santos

0000-0003-0776-7135

This thesis is presented for the Degree of
Doctor of Philosophy
of
Curtin University

January 2024

To the best of my knowledge and belief this thesis contains no material previously published by any other person except where due acknowledgement has been made. This thesis contains no material which has been accepted for the award of any other degree or diploma in any university.

Joao Victor Borges Dos Santos

29^{th} January 2024

"*Nothing in this world can take the place of persistence. Talent will not: nothing is more common than unsuccessful men with talent. Genius will not: unrewarded genius is almost a proverb. Education will not: the world is full of educated derelicts. Persistence and determination alone are omnipotent.*"

— Calvin Coolidge

Acknowledgements

This PhD research was an experimental study that required specialised and costly equipment; highly qualified and skilful professionals from different areas were also brought together to accomplish a challenging and innovative project. This was only possible due to the funds provided by the *Minex CRC*. Thanks for the financial support.

My research supervisors—Dr. Thomas Richard, Dr. Yevhen Kovalyshen, and Dr. Masood Mostofi—encouraged, supported, and guided me throughout my PhD journey. I want to acknowledge and express my sincere gratitude to them. A special thanks to Thomas, who envisioned the outcomes of this ambitious project; he was my main supervisor and was an incredible mentor from whom I have had a never-ending learning experience. Thanks also to Yevhen, who never hesitated to provide me with technical support whenever I found myself in a difficult situation. We had numerous interesting and insightful discussions that helped me understand the experiments carried out in this project. I am undoubtedly extremely privileged to be mentored by all of them; their extensive knowledge in physics, drilling engineering, and rock mechanics is extraordinary.

Andrew Wurst and Michael McKenzie were also extremely important in accomplishing this project; I cannot forget to thank them. Andrew was the principal mechanical designer and fitter responsible for the assembly, modification of components, and commissioning of the equipment used during field tests and laboratory experiments. Mike was the LabVIEW specialist responsible for the design of the data acquisition and control software. Apart from the technical support

both gave me during the experiments, we also had interesting and fun discussions about non-work related topics, such as card games and video games. Thanks for everything, and I will never forget all the funny and entertaining moments.

I also received technical and maintenance support from Luke Lans and Ryan Foster during the laboratory experiments in the workshop. In several instances, they managed to act quickly and help me overcome technical issues on the equipment that could have delayed the schedule of the experiments. Thanks for the help and support. I acquired important and useful skills after working with them in the workshop.

Last but not least, I would like to thank all of my colleagues from the *Drilling Analysis and Research Team (DART)*. Without our funny conversations and jokes, the journey throughout this research project would have been much more stressful and difficult. They are highly appreciated as well.

Abstract

Down-the-hole (DTH) percussive drilling is an excavation method widely used in the mining industry due to its high efficiency in fragmenting hard rock formations. A DTH hammer system consists of a fluid-driven (air or water) piston and a drill bit; the reciprocating movement of the piston transmits its kinetic energy to the drill bit by means of stress waves that propagate through the drill bit towards the rock formation.

In the literature on percussive drilling, the existence of an optimum drilling state is reported in some laboratory and field experimental studies. An optimum rate of penetration is achieved for a specific range of axial thrust (or weight-on-bit) beyond which the rate of penetration decreases. Several authors advance different explanations as possible root causes of the occurrence of the *Optimum Drilling State* (ODS) phenomenon, but a universal explanation or consensus does not yet exist. The main objective of this research project is to determine experimentally whether the occurrence of the ODS phenomenon is intrinsic to the bit-rock interface or attributed to the system dynamics.

The experimental investigation for this work was initiated with drilling experiments conducted at a mining site. A full-scale drilling rig (equipped with a DTH hammer system) was instrumented with high-precision and high-resolution sensors strategically installed on the machinery. Data was collected over the excavation of two boreholes; an in-depth analysis of the recorded data confirmed that an optimum performance could be achieved for specific ranges of input thrust (weight-on-bit). Moreover, due to the high sampling rate and extremely high

resolution of the sensors, the recording showed the ability to capture the bit penetration at each piston impact. This level of detail provides a unique insight into the different drilling responses.

The second stage of the experimental investigation was conducted in a laboratory environment with custom-built equipment dubbed *Woody*, that can drill shallow holes with only discrete events (one impact at a time) while controlling the weight-on-bit, indexing angle, and piston impact energy independently. The main difference between *Woody* and a full-scale drilling apparatus is the fact that the initial conditions are guaranteed to be re-established before each impact of the piston on the drill bit; in other words, the desired weight (or axial load) will always be properly applied to the drill bit before the arrival of the piston during the drilling process.

The learning acquired from the analysis of the data collected at the mining site, together with the results of the extensive experimental program carried out on *Woody* helped us to draw the following conclusion: the occurrence of the ODS phenomenon is not intrinsic to the bit-rock interface, but it is rather related to the system dynamics (piston-bit-barrel interaction). The laboratory experiments showed that the mean weigh-on-bit does not affect the mean rate of penetration. Conversely, the results showed that the WOB does affect the time required for the outer shaft (or barrel) to re-establish contact with the drill bit at each percussive cycle.

Contents

List of Figures

Chapter 1

Introduction and Objectives

Rotary percussive drilling is an excavation method widely used in the mining industry for exploration and drill-and-blast applications (Taheri et al., 2016). Figure 1.1 shows two types of percussive drilling tools, commonly designated as Top-Hammer (TH) or Down-the-Hole (DTH) depending on the location where the impact force is supplied (Kim et al., 2020). In the case of TH drilling, the force is generated by a pneumatically or hydraulically driven piston (or hammer) that continuously impacts a rotating drill rod (or shank) with a drill bit installed at its end. For DTH drilling, however, the hammer is located just above the drill bit and strikes it directly (Song, 2020).

The focus of this work is to gain a better understanding of the mechanisms associated with the drilling action of a DTH hammer assembly. This research project is part of the Mineral and Exploration Cooperative Research Centre (*MinEx CRC*) whose activities are funded by the Cooperative Research Centre Program of the Australian Government. *MinEx CRC* is a research consortium that brings together Government and Industry across Australia and aims to address the declining discovery rates of major mineral deposits within Australia, which significantly contribute to the Australian export economy (MinEx, 2018).

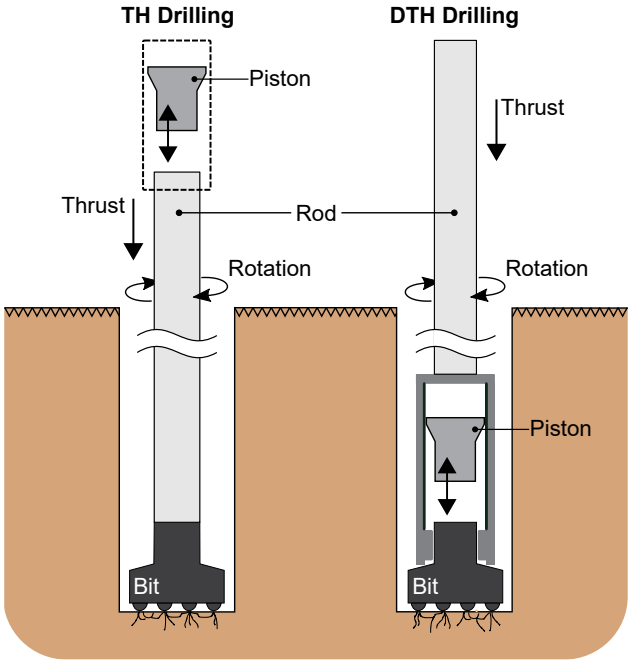

Figure 1.1: Percussive drilling methods: top-hammer drilling and down-the-hole hammer drilling.

1.1 Percussive Drilling in Mineral Exploration

The purpose of mineral exploration is to acquire detailed information on the subsurface rock formation. Among all exploration procedures, drilling can be considered one of the vital operations and it is substantially expensive to be carried out (Marjoribanks, 1997). It is paramount to know rapidly whether the explored area is mineable (or not) during the exploration phase of the drilling program (Caers et al., 2022).

1.1.1 Reverse Circulation System

A drilling rig equipped with a reverse circulation system is commonly used during the drilling exploration phase. As illustrated in Figure 1.2, the main mechanical components of such a system consist of a rotating device (or rotary head) that provides angular velocity to the drilling assembly, drill rods equipped with dual-wall pipes, a DTH hammer system, and a cyclone separator.

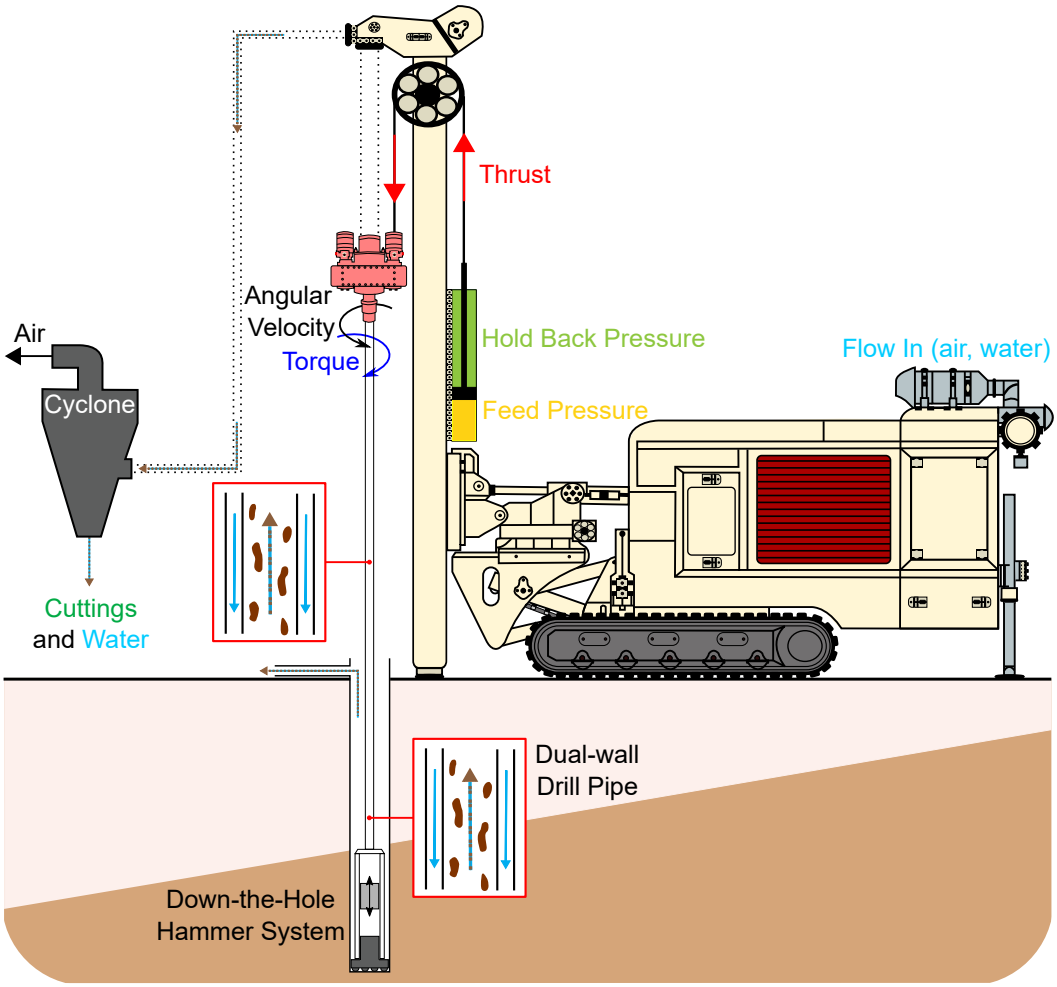

Figure 1.2: Drilling rig equipped with a reverse circulation drilling system.

In a reverse circulation drilling system, a drilling fluid (mixture of air and water) is pumped down the dual-wall drill pipe, in the annular space between its inner and outer walls, until it reaches the down-the-hole hammer system (refer to Figure 1.2). The fluid is then discharged in the borehole and flows with high velocity into the central passage of the drill bit, decreasing the pressure of its surroundings. As a result, the rock cuttings are sucked into its central passage and transported upward to the surface through the central part (inner tube) of the dual-wall pipe and collected at the cyclone separator (Luo et al., 2016; Cao et al., 2018).

1.1.2 Down-the-Hole Hammer System

Figure 1.3 depicts a sketch of a DTH hammer system. It consists of a piston (or hammer)—driven by compressed air or water—located directly above the drill bit. The pressure difference inside the rear and front chambers leads to a reciprocating movement of the piston (Zhao et al., 2014). Once the moving piston strikes the shank (top) of the drill bit, an impulsive loading force is generated (Depouhon, 2014). At the moment of impact, the kinetic energy carried by the piston is transformed into compressive stress waves that propagate to the bit-rock interface. A portion of this energy is absorbed by the rock formation, which causes its breakage by chipping and crushing (Hustrulid & Fairhurst, 1971b). The portion of energy not absorbed by the rock reflects back to the entire hammer assembly—drill bit, piston, outer shaft, and other internal components—also in the form of stress waves. As a result, it can cause the rebound of the drill bit and piston as well as the vibration of the complete DTH hammer assembly (Amjad, 1996).

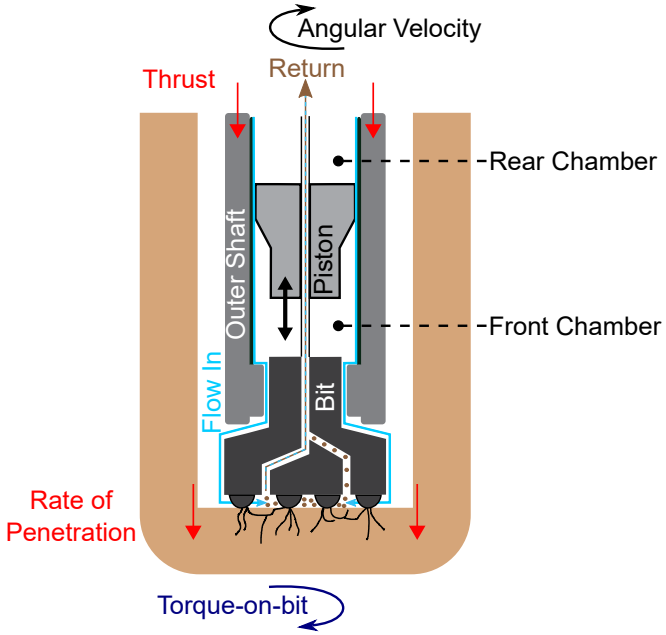

Figure 1.3: Down-the-hole hammer system.

A thrust force applied by the hydraulic feeding system of the drilling rig—transmitted

to the drill bit through the outer shaft—gives stability to the entire DTH drilling assembly and maintains the drill bit in contact with the rock formation during each impact cycle (refer to Figure 1.3). Furthermore, the entire DTH hammer system is continuously rotated to ensure that the percussive action completely fragments the borehole bottom and, consequently, the hole is excavated forward.

1.1.3 Drilling Operating Parameters

The operating parameters, also referred to as drilling variables, can be classified into two categories: (1) *independent* or (2) *dependent* parameters. The independent parameters are controlled by the drill operator throughout the drilling activities (Barr, 1985; Peck, 1989):

- Angular velocity - This parameter controls the indexing (or rotation) of the drill bit between successive piston impact cycles, which enables the buttons of the drill bit to damage new parts of the borehole bottom.
- Thrust - It is the downward force generated by the hydraulic feeding system, which is applied to the drilling assembly.
- Percussive pressure - It is the pressure of the fluid that drives the reciprocating movement of the piston. The control system of the drilling rig adjusts the fluid flow rate accordingly in order to increase or decrease the percussive pressure.

On the contrary, the dependent parameters are mainly the response of the system to the variable inputs (independent parameters) and they are affected by the rock formation as well as by the drilling conditions inside the borehole (Barr, 1985; Peck, 1989):

- Weight-on-bit (WOB) - It is the reactive force resulting from the applied thrust. The purpose of WOB is to maintain the drill bit in contact with the bottom of the borehole, which guarantees the transmission of the percussion energy to the rock formation (Schunnesson, 1998).

- Torque-on-bit (TOB) - It is related to the resistance of the drill bit to rotation.
- Hammer frequency - It is the number of piston impacts on the drill bit per unit time.
- Rate of penetration (ROP) or feed rate - It measures how fast the borehole propagates forward.

1.1.4 Optimum Drilling State (ODS)

The knowledge and experience of the drill operator dictate the drilling performance (Shen et al., 2022), which is commonly measured by the rate of penetration. In the literature on percussive drilling, several results from experimental studies show that there exists a set of control parameters—input variables—for which the ROP is maximised (Cheetham & Inett, 1953; Lundquist, 1968; Hustrulid & Fairhurst, 1972b; Unger & Fumanti, 1972; Amjad, 1996; Schunnesson, 1998; Kivade et al., 2015; Ghosh et al., 2017; Shen et al., 2022). Figure 1.4 shows an example where the ROP increases with thrust up to an optimal value, beyond which it decreases with a further increase in thrust. This phenomenon is commonly called *Sweet Spot* (Depouhon, 2014). In this thesis, however, such a term will be referred to as *Optimum Drilling State* (ODS). Published results from laboratory and field experiments assist us in understanding the probable key factors contributing to the occurrence of the ODS phenomenon:

1. indexing angle between impacts,
2. reduced indexing due to torque capacity limitation,
3. minimum WOB for optimum energy transfer efficiency and bit-rock interface pseudo stiffness.

In the next chapter, the body of works related to the occurrence of the ODS is examined in more detail.

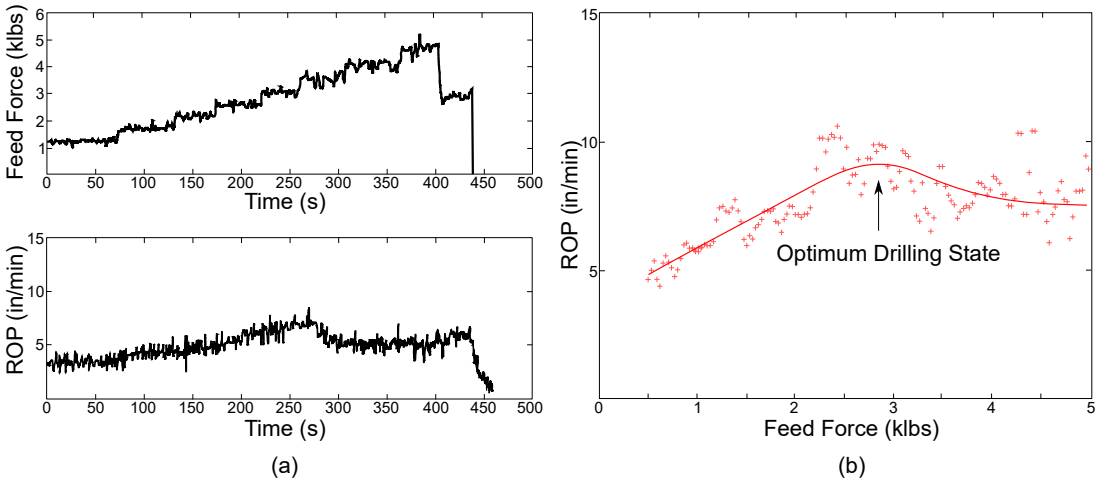

Figure 1.4: Results from field experiments: (a) feed and penetration rate relation, (b) evidence of the ODS (adapted from (Amjad, 1996)).

Although numerous studies have addressed the probable causes of the ODS, there is no consensus or clear explanation for the occurrence of this phenomenon. The absence of an accurate understanding of the relationship between the drilling parameters and the ODS occurrence hinders the development of optimisation and control algorithms that seek to maximise the ROP while borehole conditions are changing (Song et al., 2019a).

1.2 Research Objectives

The overarching goal of this research project was to gain a better understanding of the mechanisms associated with the drilling action of a down-the-hole hammer assembly. In order to achieve this, two types of experimental procedures were conducted throughout this study:

1. **Full-scale Drilling Experiments** - a full-scale drilling rig was equipped with high-precision and high-resolution sensors installed strategically on the machinery. Then, drilling data was acquired at a mining site while boreholes were being excavated by a DTH hammer system. The objectives of the full-scale drilling experiments are:
    - To develop and test a data recording system and a methodology to acquire relevant data to characterise drilling performance.
    - To identify key variables that must be measured to monitor efficiently the drilling performance in percussive drilling applications.
    - To find evidence of the ODS phenomenon.
    - To analyze the influence of operating parameters on the system response.
    - To identify and document effective drilling practices and incorporate the learning into autonomous interpretation algorithms.

2. **Single Impact Experiments** - a special custom-made piece of equipment was built and used for these experiments. Initially, a specific weight is applied to a drill bit, which rests on the surface of a rock sample. Then, a piston is accelerated towards the drill bit; after impact, the drill bit penetration is recorded with high-precision laser sensors. Finally, the rock sample is indexed and the procedure is repeated. The objectives of the single impact experiments are:
    - To investigate how the average rate of penetration is influenced by (a) the initial static force applied to the drill bit (WOB) before the

impact, (b) the piston impact energy, and (c) the indexing angle (rock rotation between impacts; the ratio of the angular velocity over the piston activation frequency).

- To investigate whether the ODS phenomenon stems from an intrinsic property of the bit-rock interface or is related to the system dynamics.

1.3 Project Significance

Despite the fact that DTH percussive drilling is a widely used technique for mineral exploration, there is still a lack of understanding of what leads to an optimal drilling condition during the drilling process. The success of the operations is greatly dependent on the experience of the drill operator (Shen et al., 2022) and it is questionable whether even the most experienced operators can achieve optimum performance of the drilling rig at all times.

The learning acquired in this research project—from tailored experiments conducted in the laboratory and field—can be used as a basis for developing appropriate monitoring systems, control algorithms, and optimisation strategies to seek performance improvement in DTH percussive drilling.

1.4 Thesis Organisation

This thesis consists of five chapters and is organised as follows:

- **Chapter 2** starts with the fundamentals of DTH percussive drilling. Then, the various time scales presented in the drilling process are examined, considering a single percussive activation. Moreover, the published results from several experimental studies relevant to this research project are also presented.

- **Chapter 3** presents the results of full-scale drilling experiments carried out at a mining site. The unique data collected by our custom-built acquisition system revealed the occurrence of novel drilling regimes, characterised by distinct patterns of the rotary head displacement. A detailed analysis and interpretation of such data are presented in this chapter.

- The results of the single impact experiments are shown in **Chapter 4**. First, the special and customised experimental setup is explained, and then a detailed analysis and discussion of the results of the experiments are provided.

- Finally, **Chapter 5** presents the conclusion of this work as well as recommendations for possible future investigations. It also summarises all key research findings acquired throughout this work.

Chapter 2

Literature Review

This chapter starts with a breakdown of the processes involved in percussive drilling, focusing on pneumatically driven DTH hammer: (1) the piston activation, (2) the energy transfer from the piston to the drill bit and rock, and (3) the interaction of the drill bit with the rock formation. The different time scales presented in one percussive cycle of a DTH hammer are also examined. Then, the results of studies relevant to this research project are presented, with a special focus on the experimental works that reported the existence of the Optimum Drilling State (ODS) and the works that discuss probable root causes for the occurrence of such a phenomenon. Finally, the chapter ends with several remarks from the Author that justify the significance of the present research.

2.1 Main Processes in Percussive Drilling

The mechanism of percussive drilling involves the interaction of several processes (Depouhon, 2014):

- the percussive activation,
- the energy transfer (impact dynamics) from the piston to the drill bit and the rock,

- and the interaction between the drill bit and the rock.

2.1.1 Hammer Activation

The origination of percussive energy is the predominant mechanism incorporated in percussive drilling (Islam & Hossain, 2020), regardless of whether the method applied is TH or DTH hammer drilling. The percussion cycle starts with the activation of the piston, generated from the conversion of pressurised fluid energy into piston kinetic energy.

In pneumatic DTH percussive drilling, compressed air—provided by a pump and compressor located at the surface—is pumped down in the borehole to feed the hammer. Due to the increased length of the drill string, pressure losses increase and result in less efficient hammer activation and borehole cleaning (Ghosh et al., 2017). Figure 2.1 depicts a schematic of a typical pneumatically driven DTH hammer, which has the following operating sequence within a single activation cycle (Lyons, 2000):

1. Assuming that the entire hammer system is initially in the borehole and suspended off-bottom, the compressed air passes freely from the pin connection to the drill bit without activating the piston.

2. When the drill bit face touches the rock surface and a weight is applied to the hammer system, the bit shank moves up inside the hammer housing also pushing the piston upward. As a result, one of the piston ports lines up with one of the control rod windows.

3. Then, compressed air flows to the front chamber and forces the piston to move upward inside the hammer housing.

4. Once the top of the stroke is reached, another port of the piston lines up with one of the control rod windows, and compressed air flows to the rear chamber. As a result, the piston moves downward until it strikes the drill

bit shank, and the air is exhausted in the borehole. It is important to emphasise that the reflected energy after impact affects the piston return velocity, piston stroke length, and cycle duration (Chiang & Stamm, 1998).

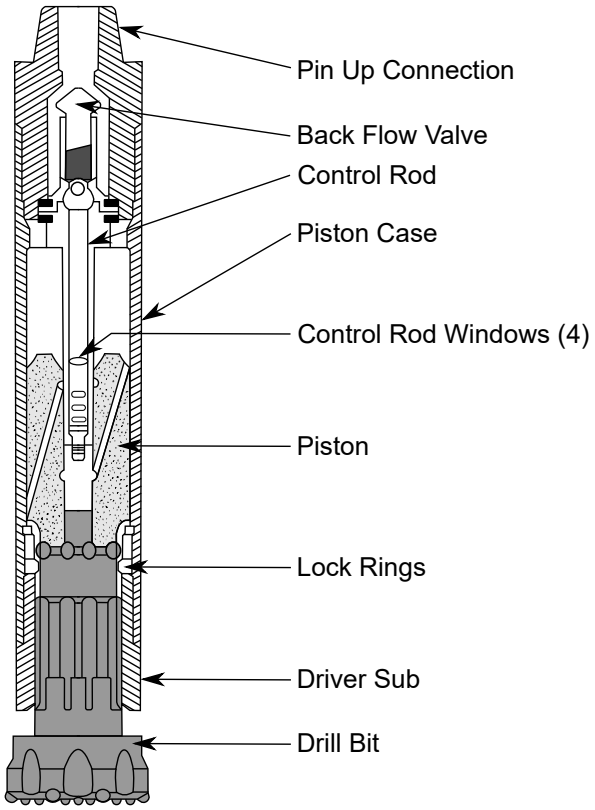

Figure 2.1: Schematic of a typical pneumatically driven DTH hammer (redrawn from (Lyons, 2000)).

The reciprocating movement of the piston affects the flow path, flow rate, and thermodynamics of the fluid that powers the hammer system (Zhao et al., 2014). Chiang & Stamm (1998) developed a thermodynamic model that allows the computation of the impact energy and frequency, as well as the raw power developed by the pneumatic hammer system. Their methodology was validated with laboratory and field tests and can be used to optimise hammer design parameters—for instance front and rear chamber sizes, piston mass, and stroke—under a set of constraints (Chiang & Stamm, 1998).

Furthermore, Zhao et al. (2014) developed a model to simulate percussive

drilling of air-driven hammers operating in different deviation angles. Their thermodynamic model can be used to estimate piston impact frequency and kinetic energy, as well as to simulate the internal motion and working status of the hammer. Laboratory tests conducted with a DTH hammer operating at different deviation angles (0°, 15°, 30°, 45°, 60°, 75°, 90°), not only validated the proposed model but also revealed that the working frequency, impact velocity, and effective output power decrease with an increase in the deviation angle (Zhao et al., 2014).

Kim et al. (2019) established and validated a simulation model to predict the impact frequency, energy, and power of pneumatic DTH hammers. Such a model consists of equations for internal orifice areas (which define the flow path of compressed air), piston motion, and drill bit flushing channels. The proposed approach was validated with laboratory scale experiments and its results suggest that the percussion power can be improved by optimising internal design factors (Kim et al., 2019).

2.1.2 Transfer of Energy

The impact of the moving piston on the shank (top) of the drill bit generates an impulsive loading force (Depouhon, 2014). At the moment of impact, the momentum and kinetic energy carried by the piston are transferred to the drill bit in the form of a compressive stress wave that propagates to the bit-rock interface (Hustrulid, 1965; Hustrulid & Fairhurst, 1971b). The work presented by Simon (1963) revealed that the conversion of piston kinetic energy into the stress wave energy has an efficiency above 90%, for geometries of piston and drill bit anvil commonly used in percussive drilling. The residual energy is associated with the rebound kinetic energy of the piston and with the energy that is dissipated into heat before the next impact occurs (Simon, 1964).

The shape of the incident stress wave is the result of the superposition of several partial reflections and transmissions at different locations within the hammer assembly, originating from discontinuities and differences in cross-section areas

(Simon, 1964). Fischer (1959) showed how to determine the shape of the stress wave using a graphodynamic method. Simon (1963) and Dutta (1968) developed computer programs to determine the interactions of reflected waves (throughout the propagation path) and to determine characteristics of the incident stress wave for pistons of different geometries, respectively. Additionally, Chiang & Elías (2008) studied the effect of complex piston geometries on percussive drilling and modelled the impact dynamics and rock fragmentation with three-dimensional isoparametric elements.

The work presented by Lundberg (1973b) shows that the energy transfer efficiency depends on the shape of the incident stress wave. Lundberg & Collet (2010) further investigated it to study the optimal wave of finite duration to maximise energy conversion efficiency (Lundberg, 1973b; Lundberg & Collet, 2010).

Impact Dynamics Modelling

A considerable amount of studies focus on the *one-dimensional wave theory* and specific bit-rock interaction laws in order to analyze the impact dynamics and interactions between the hammer, drill bit, and rock (Simon, 1964; Hustrulid & Fairhurst, 1971b; Lundberg, 1973a,b, 1985; Chiang & Elıas, 2000; Tuomas, 2004; Lundberg & Collet, 2010; Lundberg & Huo, 2017; Song et al., 2021). Such an approach implies that there is negligible attenuation and dispersion (no internal damping) of the elastic pulse during propagation, and it also assumes that originally plane cross-sections remain plane during deformation (Fischer, 1959; Simon, 1964).

The *one-dimensional wave theory* approach is used to estimate forces, displacements, and particle velocities at the piston-bit and bit-rock interfaces (Goldsmith, 2001):

- The longitudinal wave equation that governs the propagation of elastic disturbances in a given material is:

$$\frac{\partial^2 u_{(x,t)}}{\partial t^2} = c^2 \frac{\partial^2 u_{(x,t)}}{\partial x^2} \tag{2.1}$$

with the longitudinal wave velocity $c = \sqrt{\frac{E}{\rho}}$, where E is the modulus of elasticity and ρ is the mass density of the material. Equation 2.1 is a non-dispersive wave (Goldsmith, 2001) and $u_{(x,t)}$ represents the longitudinal displacement of a cross-section x as a function of time t.

- The wave equation is solved by D'Alembert's general solution, which introduces two superposed waves travelling in opposite x-directions (Graff, 2012):

$$u_{(x,t)} = g(x - ct) + h(x + ct) \tag{2.2}$$

- The strain ε_x, stress σ_x, and particle velocity v are obtained from successive differentiation of Equation 2.2:

$$\left.\begin{aligned} \varepsilon_x &= \tfrac{\partial u_x}{\partial x} = g'(x - ct) + h'(x + ct) \\ \sigma_x &= E\varepsilon_x = E[g'(x - ct) + h'(x + ct)] \\ v &= \tfrac{\partial u_x}{\partial t} = c[-g'(x - ct) + h'(x + ct)] \end{aligned}\right\} \tag{2.3}$$

- At the piston-bit and bit-rock interfaces (for instance)—where the stress wave encounters discontinuity of material and cross-section areas (refer to Figure 2.2)—the equality of particle velocity and force are the conditions to be satisfied:

$$\begin{aligned} v_{incident} - v_{reflected} &= v_{transmitted} \\ A_1(\sigma_{incident} + \sigma_{reflected}) &= A_2\sigma_{transmitted} \end{aligned} \tag{2.4}$$

where A_1 and A_2 are two different cross-section areas.

Several authors considered three-dimensional effects to investigate the stress wave propagation in percussive drilling (Chiang & Elías, 2008; Lundberg & Okrouh-

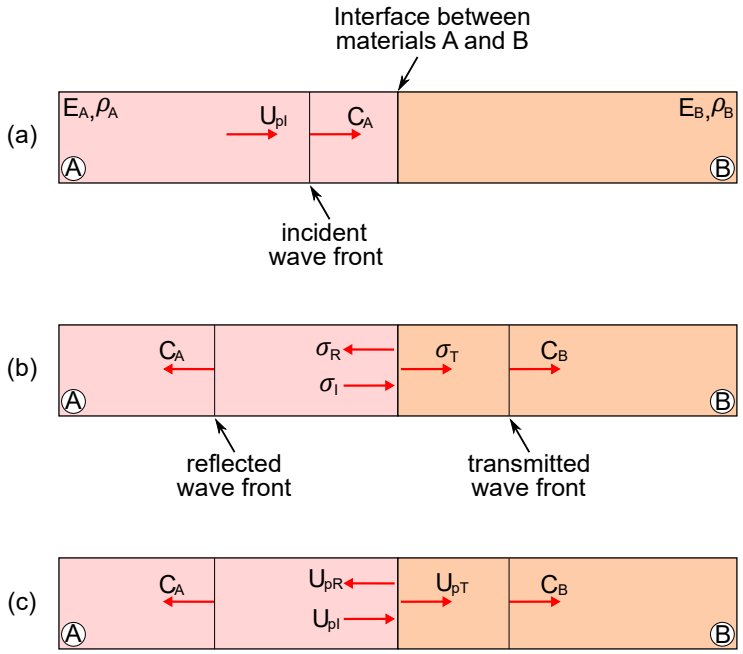

Figure 2.2: Stress wave propagation at an interface with a discontinuity of area and material: (a) incident wave before arriving at the interface, (b) reflected and transmitted waves, and (c) reflected and transmitted particle velocities (adapted from (Karimi Bakhshandi et al., 2022)).

lik, 2001, 2006). Lundberg & Okrouhlik (2001) conducted a finite element study in order to compare the efficiencies obtained from 3D and 1D analyses. It was found that the efficiencies considering 3D effects are slightly higher. However, these authors conclude that there is no need to account for 3D effects for DTH hammer systems (Lundberg & Okrouhlik, 2001).

2.1.3 Bit-Rock Interaction

Once the incident stress—generated from the impact of the piston on the drill bit—arrives at the bit-rock interface, a portion of the wave energy is absorbed by the rock, causing its breakage (Hustrulid & Fairhurst, 1971b). The remaining portion of the wave energy reflects back to the entire hammer assembly, which causes the rebound of the drill bit and piston as well as the vibration of the entire DTH hammer assembly (Amjad, 1996).

The instantaneous force F developed by the interaction of the drill bit with

the rock formation is represented by (Simon, 1964; Hustrulid & Fairhurst, 1971b):

$$F = A(\sigma(t)_{incident} + \sigma(t)_{reflected}) + F_o \tag{2.5}$$

where A is the cross-section area of the drill bit (at the interface) and F_o is any initial force acting on the bit-rock interface prior to the stress wave arrival. Additionally, the velocity of the drill bit into the rock formation (or particle velocity) is represented by (Simon, 1964; Hustrulid & Fairhurst, 1971b):

$$\frac{dy}{dt} = \frac{c}{E}(\sigma(t)_{incident} - \sigma(t)_{reflected}) + v_o \tag{2.6}$$

where c is the longitudinal wave velocity in steel, E is the modulus of elasticity, and v_o is any velocity of the drill bit prior to the stress wave arrival. Equations 2.5 and 2.6 can be combined to obtain:

$$\frac{dy}{dt} + \frac{c}{AE}(F(y) - F(y_o)) = \frac{2c}{E}\sigma(t)_{incident} + v_o \tag{2.7}$$

The function $F(y)$ in Equation 2.7 characterises the relationship of the force (F) acting at the bit-rock interface and the displacement of the drill bit into the rock formation (y). Such function depends upon the rock fragmentation process while the drill bit (with a specific shape and size) penetrates the rock formation (Simon, 1964).

Bit-Rock Interface Relationships

The rock fragmentation system under a single button is depicted in Figure 2.3. There exist distinct zones underneath the button after impact: (1) a zone with re-compacted or disintegrated material, (2) a crushed zone, and (3) a cracked zone that mainly consists of side, median, and radial cracks (Tan et al., 1998; Liu et al., 2008; Saksala, 2011; Li et al., 2021). The size of these zones, as well as the shape of the numerous cracks, are primarily dependent on the indenter geometry, rock properties, and the magnitude and rate of loading (Tan et al., 1998; Saksala,

2011). In the indentation process, from 70% to 90% of the available energy is consumed during the formation of the crushed zone (Mishnaevsky, 1995), which is an exceptionally micro fractured and inelastically deformed area that presents a hemispherical shape (Saksala, 2011).

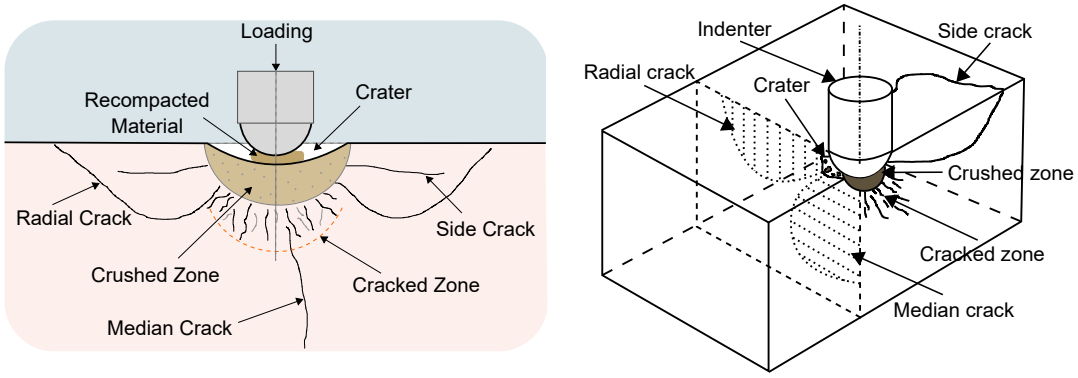

Figure 2.3: Illustration for the rock fragmentation system in rock indentation (redrawn from (a) (Li et al., 2021) and (b) (Saksala, 2011)).

Several experimental works were conducted to investigate the relationship between force and penetration at the bit-rock interface (Stephenson, 1963; Haimson, 1965; Hustrulid & Fairhurst, 1971a, 1972a,b; Pang et al., 1989; Karlsson et al., 1989). Some authors approximate this relationship as a bilinear law (Lundberg, 1982; Karlsson et al., 1989; Hustrulid & Fairhurst, 1971b; Li et al., 2000; Lundberg & Okrouhlik, 2001; Chiang & Elías, 2008; Saksala, 2011, 2013; Depouhon et al., 2013; Lundberg & Collet, 2015; Song et al., 2018), as shown in Figure 2.4.

The following mathematical equation represents the idealised force-penetration relationship from Figure 2.4 (a) (Li et al., 2000):

$$F = \begin{cases} Ky & \text{(for loading)} \\ F_{max} - \gamma K(y_{max} - y) & \text{(for unloading)} \end{cases} \tag{2.8}$$

where K determines the rock resistance to the drill bit penetration, and γ is the unloading rate coefficient, which characterises the amount of energy stored elastically in the rock and returned to the drill bit after penetration. For the loading process, the following equations are obtained (Li et al., 2000):

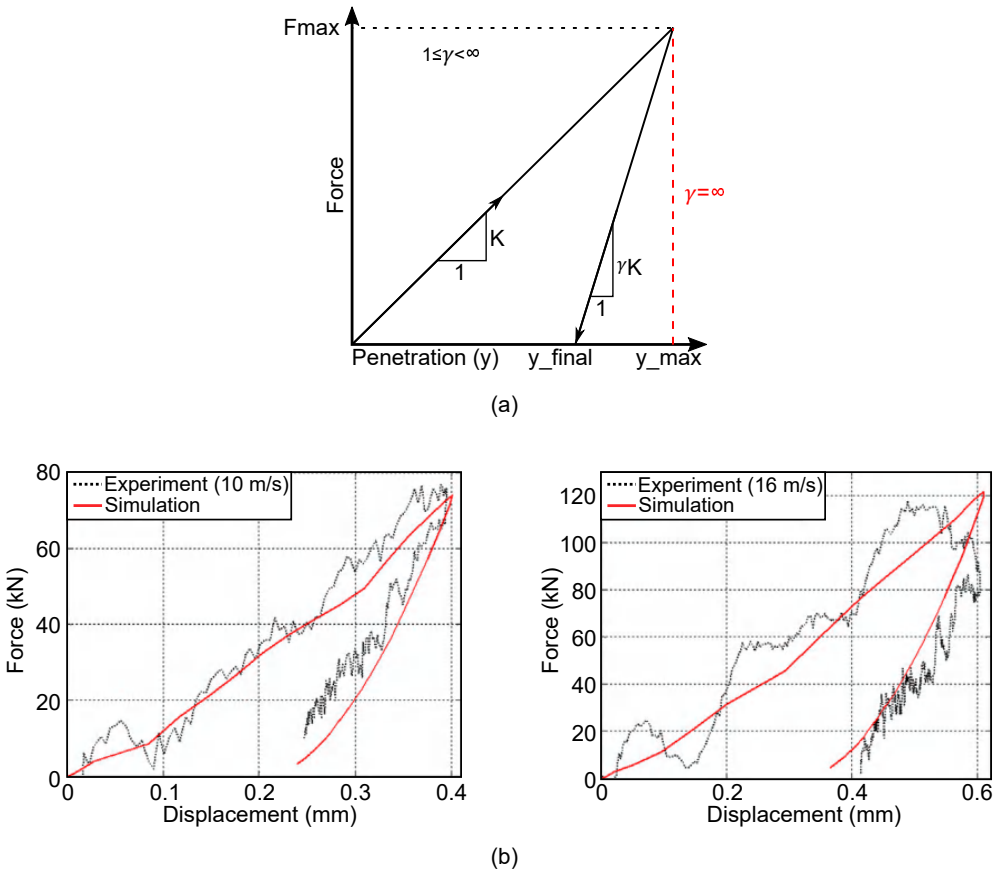

Figure 2.4: Relationship between the drill bit and the rock at the bit-rock interface: (a) idealised representation by a bilinear law, and (b) dynamic indentation results (in Kuru Granite) confirming the bilinear characteristic of the force-penetration curve (Saksala et al., 2014). The results of other studies also support the bilinear approximation (Liu et al., 2008; Wang et al., 2011; Saksala, 2011, 2013).

$$\left.\begin{aligned} A(\sigma_{incident} + \sigma_{reflected}) &= F && \text{(Equation 2.5)},\\ \tfrac{dy}{dt} &= \tfrac{c}{E}(\sigma_{incident} - \sigma_{reflected}) && \text{(Equation 2.6)},\\ F &= Ky && \text{(with initial conditions: } t = 0, F = 0). \end{aligned}\right\} \quad (2.9)$$

Additionally, the unloading process is represented by the following mathematical equations (Li et al., 2000):

$$\left.\begin{aligned} A(\sigma_{incident} + \sigma_{reflected}) &= F && \text{(Equation 2.5)}, \\ \tfrac{dy}{dt} &= \tfrac{c}{E}(\sigma_{incident} - \sigma_{reflected}) && \text{(Equation 2.6)}, \\ F &= F_{max} - \gamma K y_{max} + \gamma K y && \text{(with initial conditions:} \\ & && t = \tau, F(t) = \lim_{t \to \tau^-} F(t)). \end{aligned}\right\} \tag{2.10}$$

Considering the idealised relationship between the drill bit and the rock shown in Figure 2.4 (a), the penetration process can be explained as follows (Hustrulid & Fairhurst (1972a)):

1. The penetration process initiates when the first incident stress ($\sigma_{incident}$) arrives at the bit-rock interface. As a consequence, a bit force (F) and a reflected stress wave ($\sigma_{reflected}$) are generated (refer to Figure 2.5).

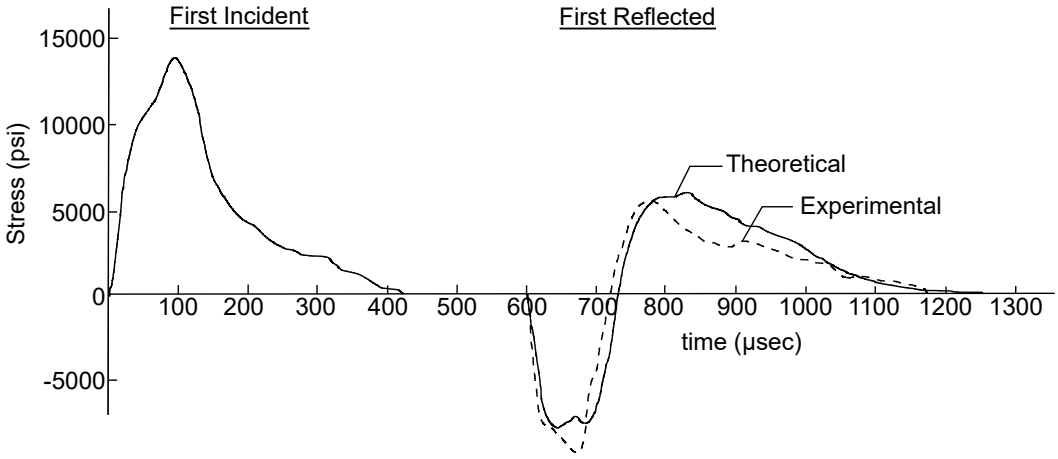

Figure 2.5: Strain wave captured during indentation test (using long rod) on Indiana limestone (redrawn from (Hustrulid & Fairhurst, 1972a)).

2. The reflected stress wave ($\sigma_{reflected}$) gradually changes from tensile to compressive. The penetration ceases once the amplitude of the reflected and incident waves become equal, which corresponds to the instant when the maximum force (F_{max}) and displacement (y_{max}) are achieved.

3. Then, the rock expands elastically under the drill bit—due to the decrease in force on the drill bit—and the stored elastic energy (in the rock) is released

back to the drill bit. As a consequence, it appears as added energy in the tail of the compressive reflected wave.

4. Finally, the drill bit rests in contact with the rock at a constant depth (y_{final}) once the elastic expansion is complete (Hustrulid & Fairhurst, 1972a).

Some of the energy of the reflected stress wave ($\sigma_{reflected}$) goes into the piston (at the piston-bit interface), while part of the reflected wave can be reflected back towards the rock formation as a secondary incident wave (Lundberg & Collet, 2015). Hustrulid & Fairhurst (1972a) accounted for the effect of the secondary incident wave in their study. However, the secondary wave does not contribute substantially to the work performed on the rock formation, due to the fact that it contains little energy (Lundberg & Collet, 2015). Moreover, the work conducted by Changming (1991) introduced an analytical model to study the energy transfer efficiency of hydraulic rock drills. It was found that the secondary incident stress wave has an insignificant effect on the energy transfer efficiency (Changming, 1991).

2.2 Analysis of One Percussive Cycle in Terms of Time Scales

This section will examine the various time scales presented in the percussive drilling process of a DTH hammer assembly.

The Start of the Percussive Cycle

In this analysis, the start of the percussive cycle ($t = 0$) will be considered as the moment when the piston starts moving upwards due to increased pressure inside its front chamber (refer to Figure 2.6).

The time scale T_1 represents the time duration from the start of the cycle

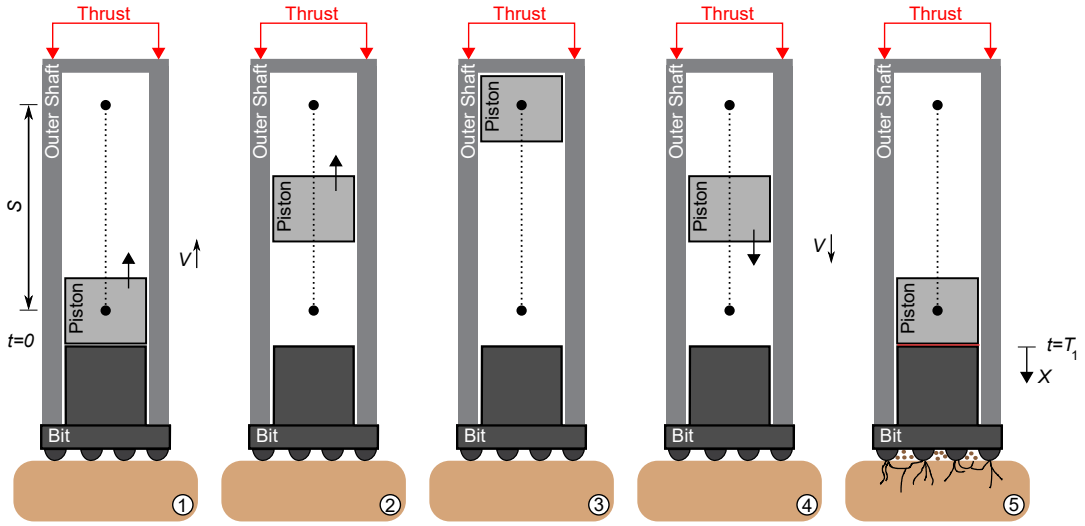

Figure 2.6: Piston starts moving upwards at $t = 0$ until it strikes the drill bit at $t = T_1$.

until the piston strikes the drill bit:

$$T_1 = \frac{2S}{V} \tag{2.11}$$

where S is the piston stroke length and V is the piston velocity. The time between two consecutive impacts is about 0.05 seconds for a 20 Hz hammering frequency (common in pneumatic DTH percussive drilling). Therefore, T_1 is in the order of O(0.01)s.

After Piston Impact ($t > T_1$)

The impact of the piston on the drill bit originates elastic perturbations that travel in opposite directions away from the interface (refer to Figure 2.7) with the following travel times:

$$\begin{aligned} T_2 &= \frac{L_p}{c_p} \\ T_3 &= \frac{L_b}{c_b} \end{aligned} \tag{2.12}$$

where T_2 is the time for the perturbation to reach the other extreme of the piston, T_3 is the time for the perturbation to reach the rock, and c is the stress wave

velocity in the material (approximately 5000 m/s in steel). Since both lengths are in the order of O(0.1)m, then both time scales T_2 and T_3 are in the order of O(10^{-5})s.

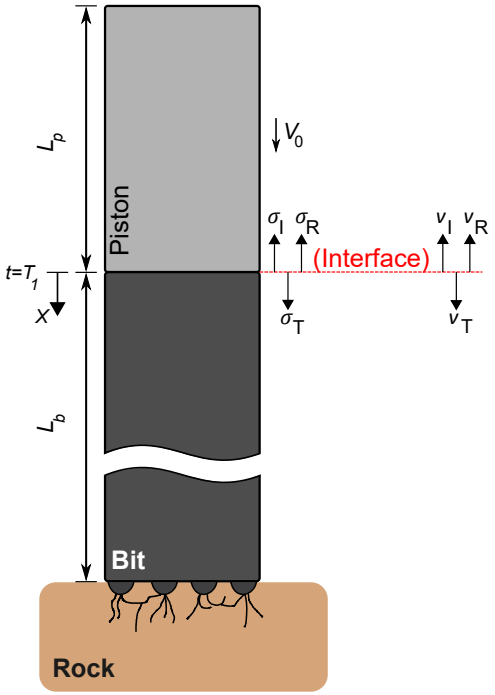

Figure 2.7: One-dimensional model to represent a DTH hammer system, where L_p is the piston length, L_b is the drill bit length, V_0 is the piston initial velocity prior to impact, σ the stress, and v the particle velocity.

At the piston-bit interface, the longitudinal compressive force wave resulting from the impact is represented by the following expression (Graff, 2012):

$$F_{incident} = -\frac{EAV_0}{c} exp^{(-\frac{EA}{cm_p}t)}, (t > T_1) \tag{2.13}$$

where m_p is the mass of the piston. Equation 2.13 reveals T_4, which characterises the rate of change in the incident force at the interface (Song, 2020):

$$T_4 = \frac{cm_p}{EA} \tag{2.14}$$

Results from experimental studies showed that the time scale (T_4), related to the decay of the incident impulse force, is in the order of O(10^{-4}), as shown in

Figure 2.8.

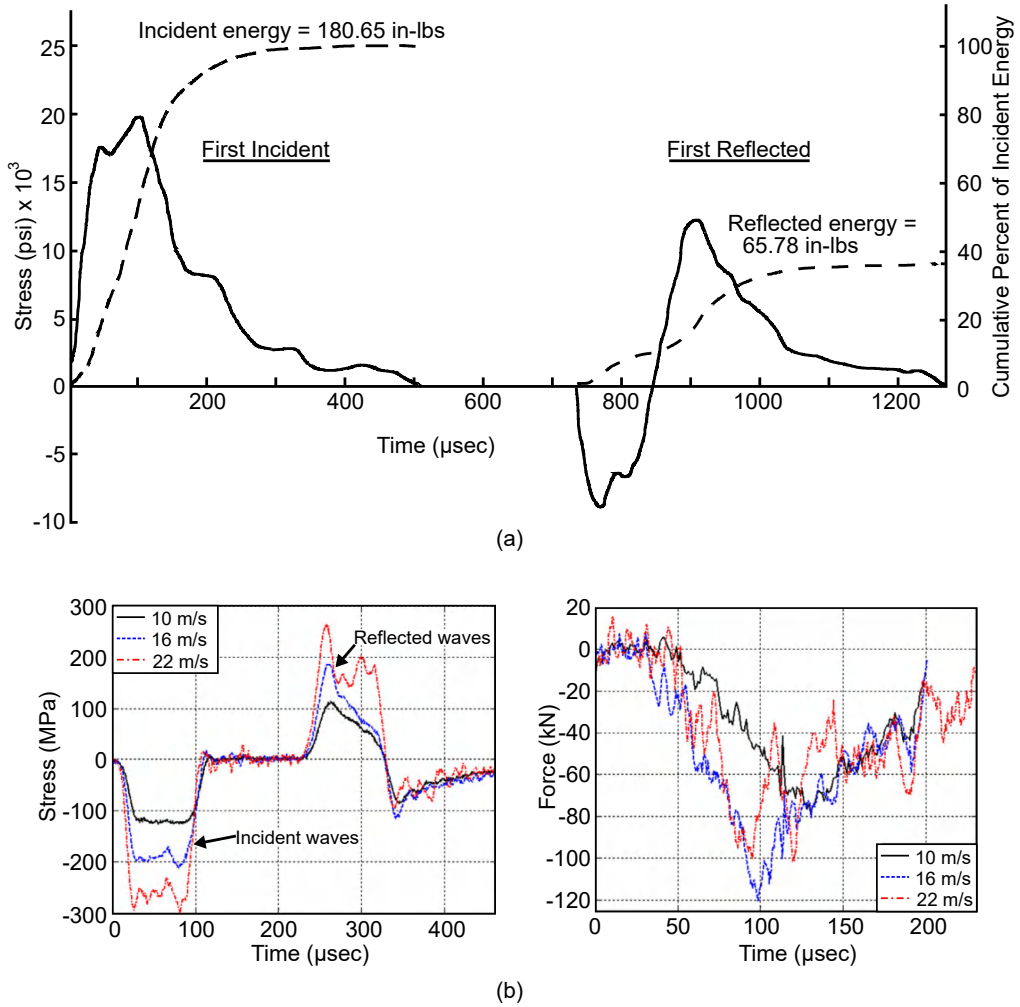

Figure 2.8: Results from percussive drilling experiments: (a) analysis of stress waves for a typical percussive blow; experiments carried out with a jackleg-type drill on Pink Tenessee marble for a thrust of 1171 N and machine air pressure of 3.44 bar (redrawn from (Hustrulid, 1965)), and (b) percussive drilling with a triple-button bit on Kuru granite; stress signals and corresponding force as a function of time for different impact velocities (Saksala et al., 2014).

After Rock Destruction

At the bit-rock interface, a minimum thrust force must be applied in order to ensure that the drill bit is in adequate contact with the rock at the moment of arrival of the first incident wave (Hustrulid & Fairhurst, 1971b). Once the drill bit penetrates the rock, the outer shaft (hammer case) needs to become

reconnected to the drill bit before the next piston impact (refer to Figure 2.9); this guarantees that an appropriate thrust will be reapplied to the drill bit before the incident wave from the subsequent impact arrives. Therefore, the time T_5 for the reconnection of the outer shaft and drill bit is desired to be:

$$T_5 < T_1 \tag{2.15}$$

which is in the order of O(0.01)s.

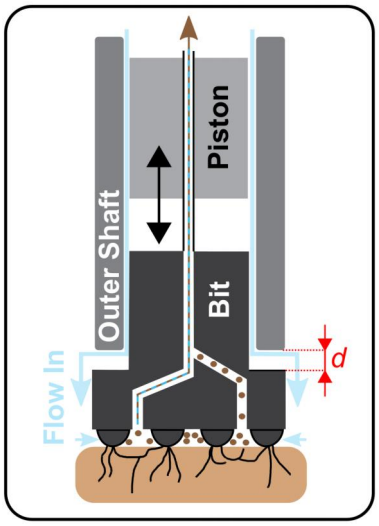

Figure 2.9: Gap d between the drill bit and outer shaft.

Table 2.1 presents a summary of the different time scales in DTH percussive drilling, from the moment the piston is activated until the end of the percussive cycle.

Description	**Time Scale**	
Duration from piston activation until impact	$T_1 = \frac{2S}{V}$	O(0.01)s
Travel time of elastic perturbation on the piston	$T_2 = \frac{L_p}{c_p}$	O(10^{-5})s
Travel time of elastic perturbation on the drill bit	$T_3 = \frac{L_b}{c_b}$	O(10^{-5})s
Stress pulse duration induced by the piston impact	$T_4 = \frac{cm_p}{EA}$	O(10^{-4})s
Time to reconnect outer shaft and drill bit	$T_5 < T_1$	O(0.01)s

Table 2.1: Different time scales in DTH percussive drilling.

2.3 Experimental Investigation

This section presents the results of experimental investigations that are relevant to this research project.

2.3.1 Observations on Force-Penetration Relationship

Hustrulid (1965) conducted a series of drop tests[1] using a 4-wing drill bit on Pink Tennessee marble rock samples in order to investigate the influence of surface roughness (underneath the bit) on the force-penetration relationship curve. During the experiments, the drill bit was indexed by a fixed angle of 34°, and the cuttings were removed with compressed air after each impact. The results from his experiments showed that the surface roughness affects the initial portion of the force-penetration curve due to the fact that it determines whether the bit is in adequate contact with the rock or not, which in turn influences the transmission of energy to the rock. As shown in Figure 2.10, the smoothness of the contact region between the rock and the drill bit affects the rate of change of the force during loading.

Such observations are in agreement with results from experiments conducted by Fourmeau et al. (2015) on Kuru granite rock samples. Using a seven-button drill bit, these authors carried out a series of drop tests at a fixed impact energy (13 J or 33 J), flushing with compressed air the surface of the rock sample as well as indexing the relative position between the bit and the rock by a fixed angle (10° or 20°) after each impact. The aim of their investigation was to assess the influence of the indexing angle and impact energy on the bit-rock interface law. The results of the test series (refer to Figure 2.11) show a considerable non-linearity on the bit-rock interface during loading, where the drill bit displacement increases rapidly with relatively slight resistance at the beginning (before the stiffness tran-

[1]Drop Test - Initially a lumped mass attached to a drill bit is brought to a specific height. Then, the drill bit is released onto a rock specimen and its kinetic energy (before and after impact) and the volume of the generated crater are measured (Song et al. (2019a)).

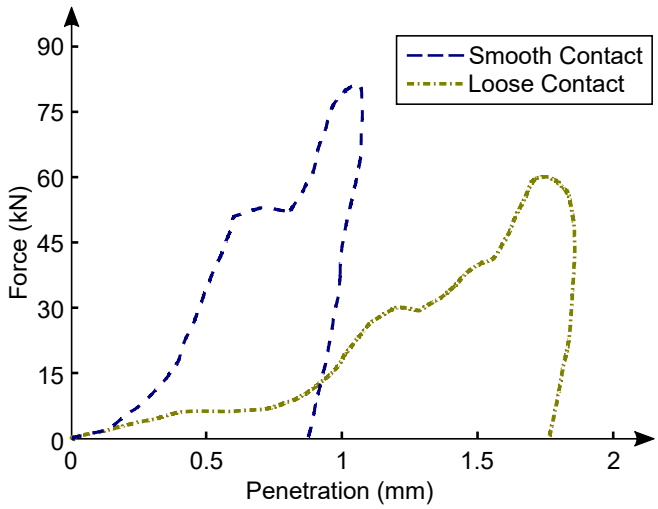

Figure 2.10: Influence of the surface smoothness underneath the drill bit on the force-penetration relationship (adapted from (Hustrulid, 1965)).

sition). Moreover, not only such regions before the stiffness transition but also the peak force and the indentation penetration are affected by the indexing angle and impact energy. Fourmeau et al. (2015) fitted a trilinear bit-rock interaction law for each test series according to the shape of the force-penetration curves observed in Figure 2.11. However, these authors acknowledge the importance of further experimental studies to establish reliable functions for the bit-rock interaction laws.

2.3.2 Influence of WOB on energy transmission

Hustrulid (1965) performed drilling experiments on Pink Tenessee marble using a horizontally mounted jackleg-type drill. His experimental setup was comparable to TH drilling since a 3-meter steel rod was used in order to avoid overlapping of reflected and incident strain waves during the experiments. He recorded strain waveforms for different values of machine air pressure (2, 2.75, 3.44, 4.13, and 4.82 bar) and thrust (360, 781, 1171, and 1562 N). Figure 2.12 shows strain waves that were recorded during percussive drilling tests for a given machine air pressure and different values of applied thrust. It is noticeable that the incident wave (initial part) is nearly identical among all waves. However, the tensile portion of

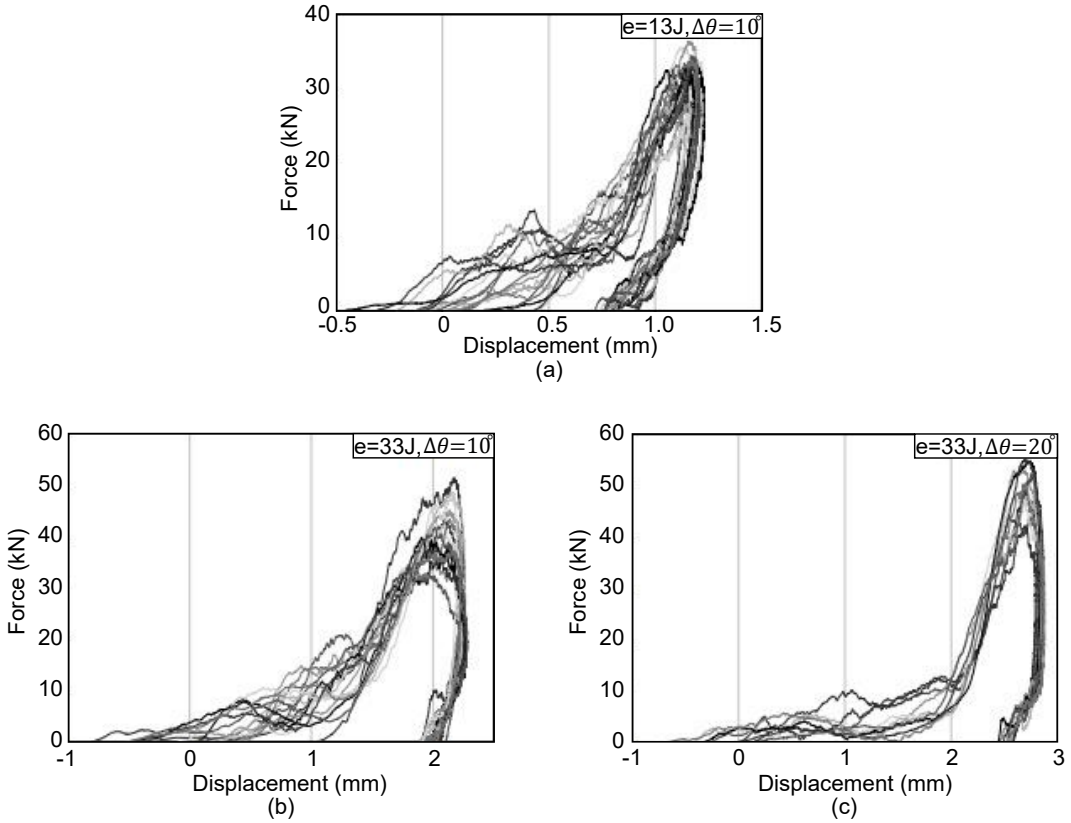

Figure 2.11: Force-penetration curves for drop tests carried out on Kuru granite: (a) 17 impacts overlapped considering impact energy of 13 J and indexing angle of 10°, (b) 16 impacts overlapped considering impact energy of 33 J and indexing angle of 10°, and (c) 10 impacts overlapped considering impact energy of 33 J and indexing angle of 20° (adapted from Fourmeau et al. (2015)).

the reflected waves decreases—as WOB becomes larger—while the compressive portion increases. A low value of WOB does not guarantee adequate contact of the drill bit with the rock surface; therefore, the energy transmission to the rock is affected.

2.3.3 Optimum Drilling State (ODS) in Percussive Drilling

Several results from laboratory and field experiments (Cheetham & Inett, 1953; Lundquist, 1968; Hustrulid & Fairhurst, 1972b; Unger & Fumanti, 1972; Amjad, 1996; Schunnesson, 1998; Kivade et al., 2015; Ghosh et al., 2017; Shen et al., 2022) have demonstrated that there exists a set of control parameters—input

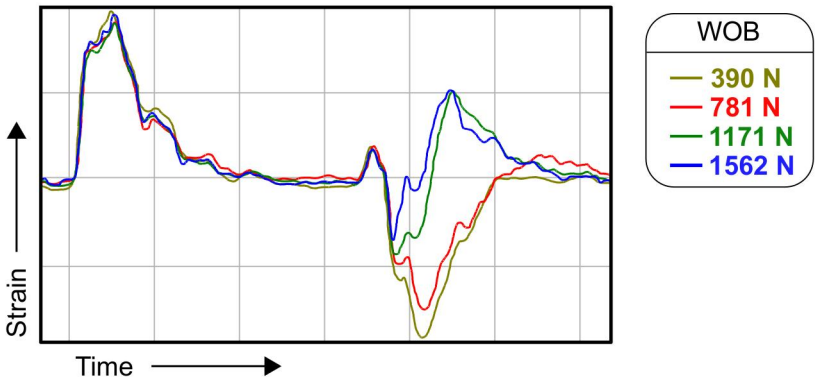

Figure 2.12: Superimposed strain waves recorded during percussive drilling experiments for a fixed machine air pressure (3.44 bar) and different values of applied thrust. For WOB of 390 N, the incident wave resembles as it has been exposed to a free end reflection at the bit-rock interface (adapted from (Hustrulid, 1965)).

variables—for which the ROP is maximised. The most common example is when the ROP increases with thrust up to an optimal value, beyond which it decreases with a further increase in thrust. The results of the work conducted by Hustrulid (1971) exemplify the occurrence of the ODS, as shown in Figure 2.13.

The results of different experimental studies assist us in understanding the probable key factors responsible for the ODS occurrence. It is important to emphasise that there is no consensus in the literature pertaining to the root causes of such a phenomenon.

Influence of the Indexing Angle on the ROP

Cheetham & Inett (1953) carried out drilling experiments on Darley Dale sandstone using a percussive drill machine with internal (rifle-bar) rotation. One of the tests was to investigate the effect of the indexing angle on the ROP. They considered three different rifle-bar rotations: 18°, 24°, and 30° (angular displacement between blows). As shown in Figure 2.14, the ROP was maximised for different values of thrust for each rifle-bar rotation, with the highest ROP being obtained from the 18° indexing angle.

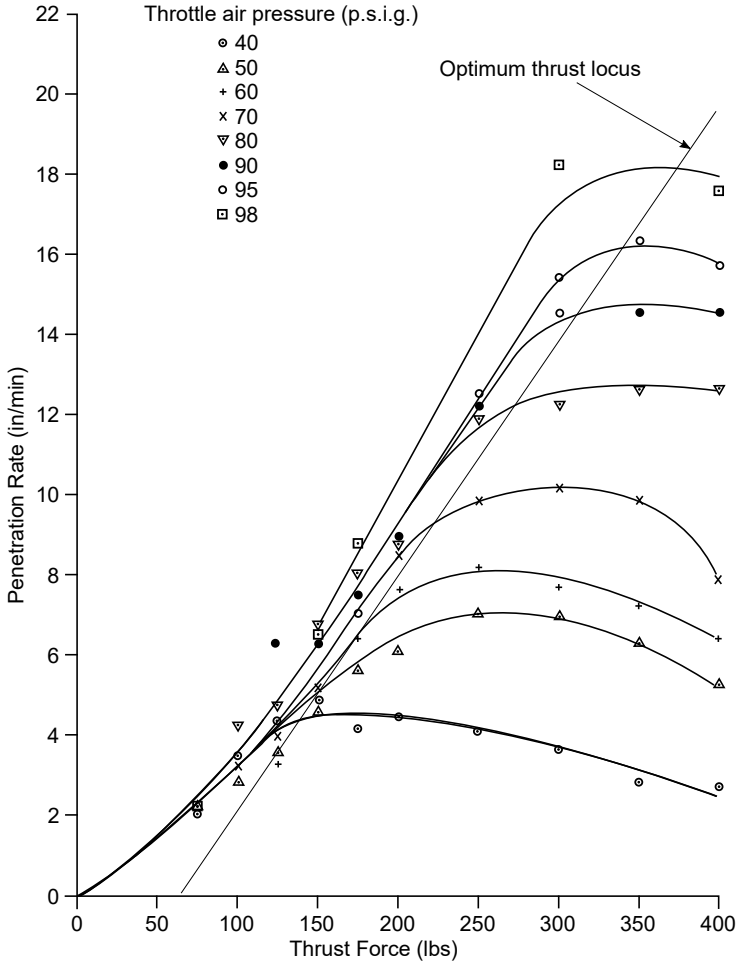

Figure 2.13: ODS phenomenon for different machine throttle air pressures. Experiments conducted with a rock drill at Robinson Deep Gold Mine (redrawn from (Hustrulid, 1971)).

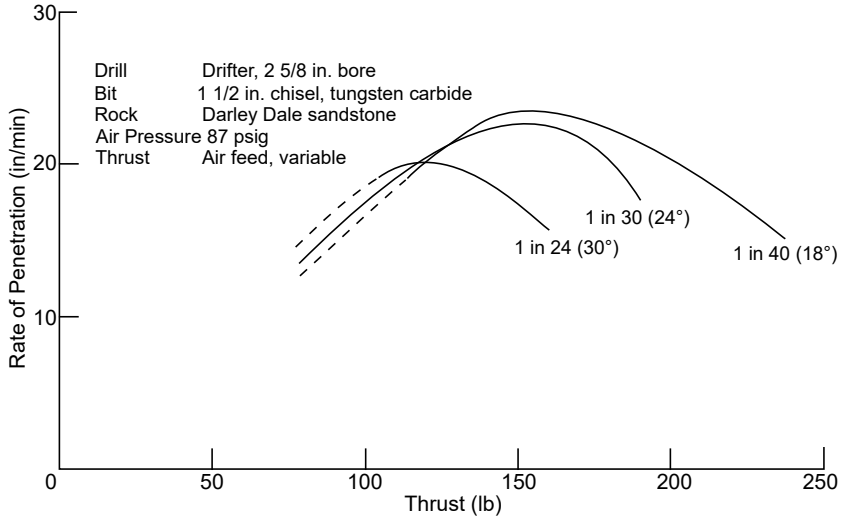

Figure 2.14: Effect of indexing angle on the ODS occurrence (adapted from (Cheetham & Inett, 1953)).

Shaw (1965) conducted similar drilling experiments to what Cheetham & Inett (1953) carried out. The results presented in Figure 2.15 show that the rifle-bar with angular displacement of 18° presented a higher optimum ROP. The results of both experiments indicate that the indexing angle between blows does affect the overall drilling performance. However, there was no attempt to isolate the parameters hammer frequency, blow energy, and change in stroke, which were probably varying during the experiments and could also be responsible for the overall drilling response.

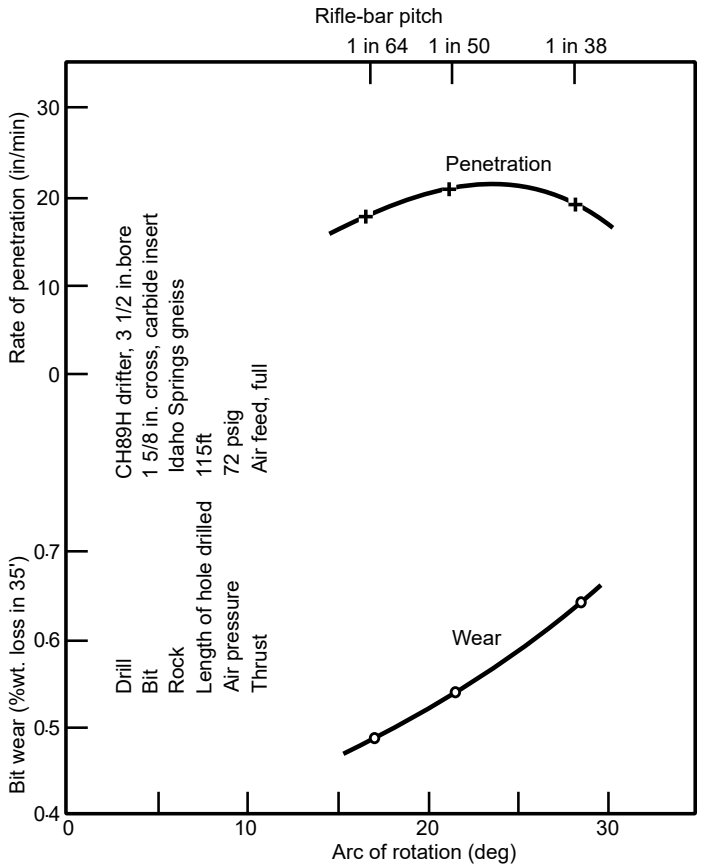

Figure 2.15: Effect of indexing on the rate of penetration (adapted from (Shaw, 1965)).

Decrease in Drilling Performance not Related to Bit Wear

The results from the series of experiments conducted by Shaw (1965) (refer to Figure 2.15) also show that bit wear had already taken place when the optimum

ROP (for indexing angle of 18°) was obtained, indicating that the ODS occurrence is not related to the increased bit wear. This is confirmed by the results of several field experiments carried out at a mining site by Amjad (1996), which were conducted in different locations using sharpened drill bits that were frequently changed to minimise the effect of bit wear; the ODS phenomenon was observed nonetheless, as shown in Figure 2.16.

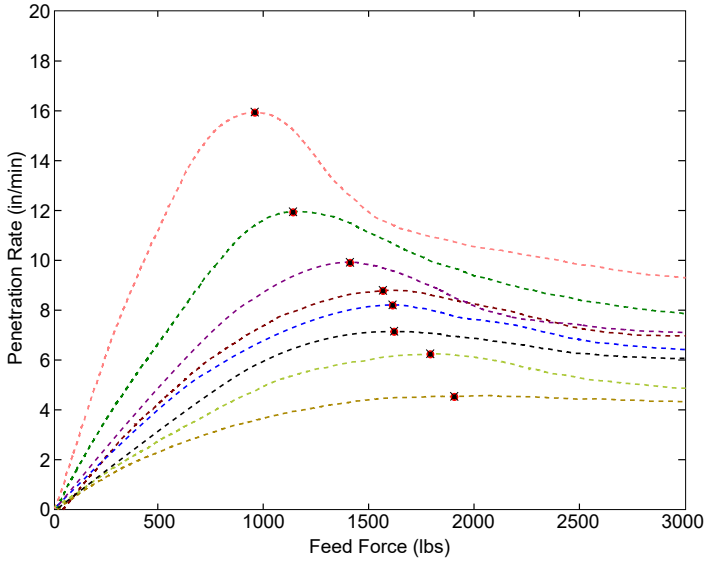

Figure 2.16: Results from field experiments carried out in different locations. Results indicate that the ODS phenomenon is also dependent on rock formation (redrawn from (Amjad, 1996)).

Limited Torque Capacity of the Machine Affects Drilling Performance

Hustrulid (1965) also observed the occurrence of the ODS while performing field experiments on Pink Tenessee marble using a jackleg-type drill. Figure 2.17 shows the effect that the applied thrust had on both ROP and RPM during the tests. This author attributed the reduction of the drilling performance to the reducing indexing for excessive values of applied thrust (refer to Figure 2.17 (b)).

However, the results of the work conducted by Unger & Fumanti (1972) showed that the decrease in ROP with the increase in applied thrust can still take place even when the RPM of the machine is maintained constant, as shown

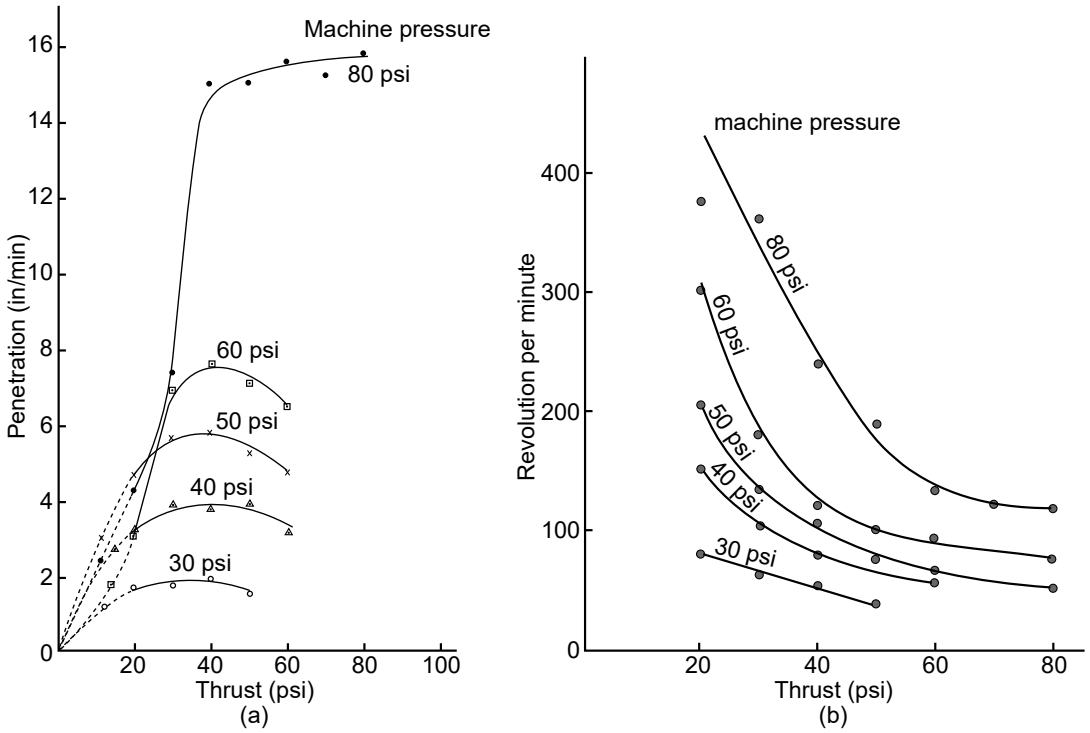

Figure 2.17: Drilling experiments on Pink Tenessee marble: (a) ROP varying with thrust for various machine pressures, and (b) RPM varying with thrust for different machine pressures (adapted from (Hustrulid, 1965)).

in Figure 2.18. These authors carried out laboratory experiments using a horizontally mounted percussive drill machine equipped with an air motor to provide independent rotation; the air pressure provided to the motor was constantly readjusted during the experiments in order to maintain consistent rotation speed.

Bit-rock Interface Pseudo-stiffness as Probable Cause of the ODS

Song et al. (2019b) developed a phenomenological model to investigate the influence of the WOB on the pseudo-stiffness k at the bit-rock interface (refer to Figure 2.19). These authors propose that the parameter WOB can induce an optimal pseudo-stiffness k that maximises the transmission of energy from the drill bit to the rock during the first impulsive wave (provided a small bit-rock impedance ratio). Even though it was a theoretical work without confirmation through experiments, these authors suggest that the occurrence of the ODS phenomenon is

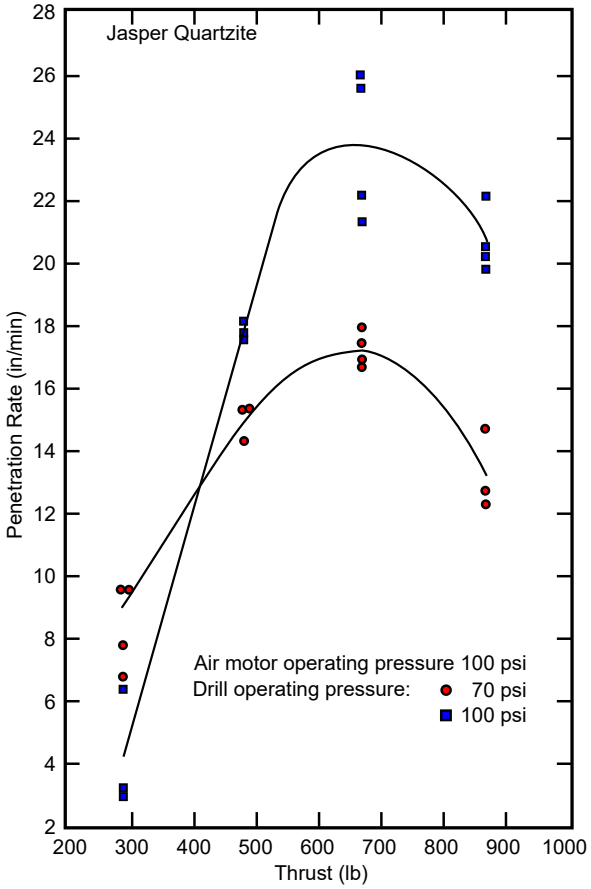

Figure 2.18: Drilling experiments on Jasper Quartzite: ROP varying with thrust; air motor operating pressure set as 100 psi at the start of the experiments for both drill operating pressures (70 and 100 psi) (redrawn from (Unger & Fumanti, 1972)).

intrinsic to the bit-rock interaction laws (Song et al., 2019a,b).

2.4 Concluding Remarks and Research Gap

In this chapter, the fundamentals of down-the-hole percussive drilling were presented as well as the results from relevant experimental studies that are related to this research project. The following observations can be made:

- DTH percussive drilling presents multiple processes that have different time scales. Breaking down a single percussive cycle and understanding the different processes that occur, assisted us to have a better insight into the

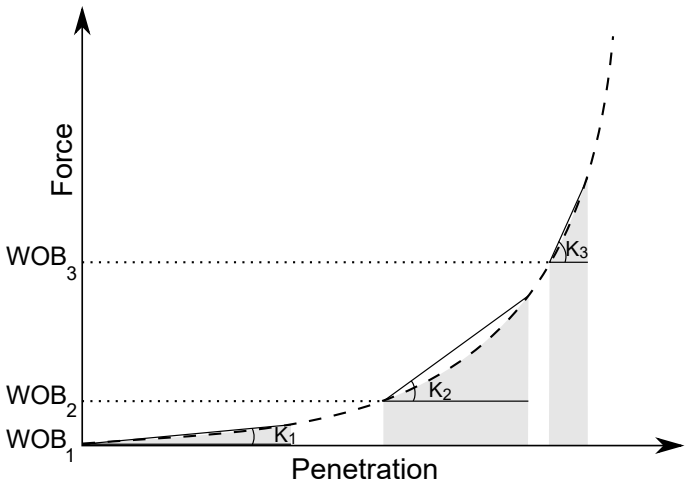

Figure 2.19: Pseudo-stiffness increasing with WOB. The resistance to penetration at the bit-rock interface is represented as the secant slope (pseudo-stiffness), and the force/energy transfer is the area below the curve (redrawn from (Song et al., 2019a)).

mechanisms of percussive drilling. Furthermore, it was also fundamental during the planning phase of our experimental investigation described in the next chapters, especially for the selection of hardware; for instance, high-precision and high-sampling rate sensors to monitor specific drilling parameters during drilling.

- The force-penetration relationship is commonly investigated by conducting drop tests. However, the nature of such experiments does not allow investigation of the effect of pre-stress (static thrust) on the force-penetration relationship and, therefore, it is not representative of the process involved in down-the-hole percussive drilling.

- There is no consensus or clear explanation for the occurrence of the ODS phenomenon. Several hypotheses must be investigated further:

    1. Indexing angle - the effect of this parameter must be investigated while other parameters are kept constant (for instance, thrust, piston stroke, blow energy, and frequency).

    2. Pseudo-stiffness at the bit-rock interface (Song et al., 2019a,b) - the

hypothesis that the ODS occurrence is intrinsic to the bit-rock interface must be investigated through experiments. There is no evidence of single-blow experiments with initial static force (thrust) applied to the drill bit prior to piston impact.

Therefore, this project will be focused primarily on experimental work:

- **Full-scale drilling experiments with a DTH hammer system** - the entire hammer system must be appropriately monitored, and drilling data must be collected for analysis.

- **Single impact experiments** - a special experimental setup must be designed to allow us to apply an initial static force on the drill bit (prior to piston impact) and different indexing angles between impacts. After each impact, several parameters must be quantified: the piston velocity before and after impact, the impact energy, the drill bit displacement, the outer shaft displacement, and the time required for the outer shaft to re-establish contact with the drill bit.

Chapter 3

Field Tests: Drilling Data Collection and Analysis

To better understand the mechanisms associated with the drilling action of a DTH hammer system, the research group involved in this work visited a mining site and collected drilling data with the assistance of McKay Drilling personnel (refer to Figure 3.1). A heavy-duty truck-mounted drilling rig (Schramm T685WS) was equipped with a custom-built monitoring system to collect data while the drilling crew conducted operations using a DTH hammer system. Two boreholes, approximately 200 metres deep, were excavated.

This chapter details our approach to collecting, preprocessing, and interpreting down-the-hole hammer activities. First, the sensors and data acquisition system as well as the rationale behind their selection are presented. Then, the algorithms I developed to process the data are introduced. They were used to estimate several drilling parameters, such as the bit and hole depths, the weight and torque applied to the drill bit, the rate of penetration, the bit penetration at each piston impact, and the piston impact frequency.

Finally, the outcomes of the data analysis are provided. Evidence of the ODS phenomenon was found in several instances, even though the drill operators were applying excessive weight-on-bit throughout the drilling operations. Moreover,

Figure 3.1: Drilling rig being mobilised to the desired location. Rio Tinto mining site area located near Newman (approximately 1177 kilometres from Perth (capital of Western Australia)).

the data analysis also revealed the occurrence of different drilling regimes characterised by distinct patterns of the rotary head displacement.

3.1 Drilling Rig and Instrumentation

The main objective of the field tests is to study the mechanisms associated with the drilling action of a DTH hammer system. To accomplish such a task, our team designed and built a monitoring system and installed it on a truck-mounted drill rig prior to the drilling tests, aiming to acquire the following information and key variables:

1. To estimate the precise location of the drill bit and how deep the borehole has been drilled (bit depth and hole depth parameters).

2. To identify precisely the instant when the drill bit touches the borehole

bottom and also the moment when the hammer system becomes active.

3. To estimate several drilling parameters, such as ROP, WOB, and TOB.

4. To capture the piston impact frequency—that normally ranges from 15 to 100 Hz—and the drill bit penetration after each piston impact.

5. To capture events that occur between each piston impact on the drill bit.

3.1.1 Drilling Rig and Monitoring System

The Schramm truck-mounted rotary drilling rig T685WS (refer to Figure 3.2) consists of five main sub-systems:

- **Hoisting System** - The mast hosts the actuating mechanisms (hydraulic cylinders) that move the drill string and apply thrust to the drill bit. The hydraulic rotary head rotates the drill string.

- **Handling System** - A hydraulically driven mechanism handles the rods, adding or removing them from the drill string.

- **Fluid Circulation System** - The drilling rig was equipped with an 1150 CFM (at 24.1 bar) air compressor booster installed in series with a standard 1350 CFM (at 35.5 bar) air compressor. A water pump with a capacity of 95 l/min was also utilised.

- **Return System** - A cyclone separates the cuttings from the carrying medium (air and water) that transports the cuttings from the borehole bottom to the surface through an inner tube inside the drilling rods.

- **Down-the-hole Hammer System** - A pneumatic DTH hammer assembly was utilised to excavate the rock formation. The drilling assembly consisted of a Schramm AD124RC hammer with a 133-millimetre drill bit (refer to Figure 3.3).

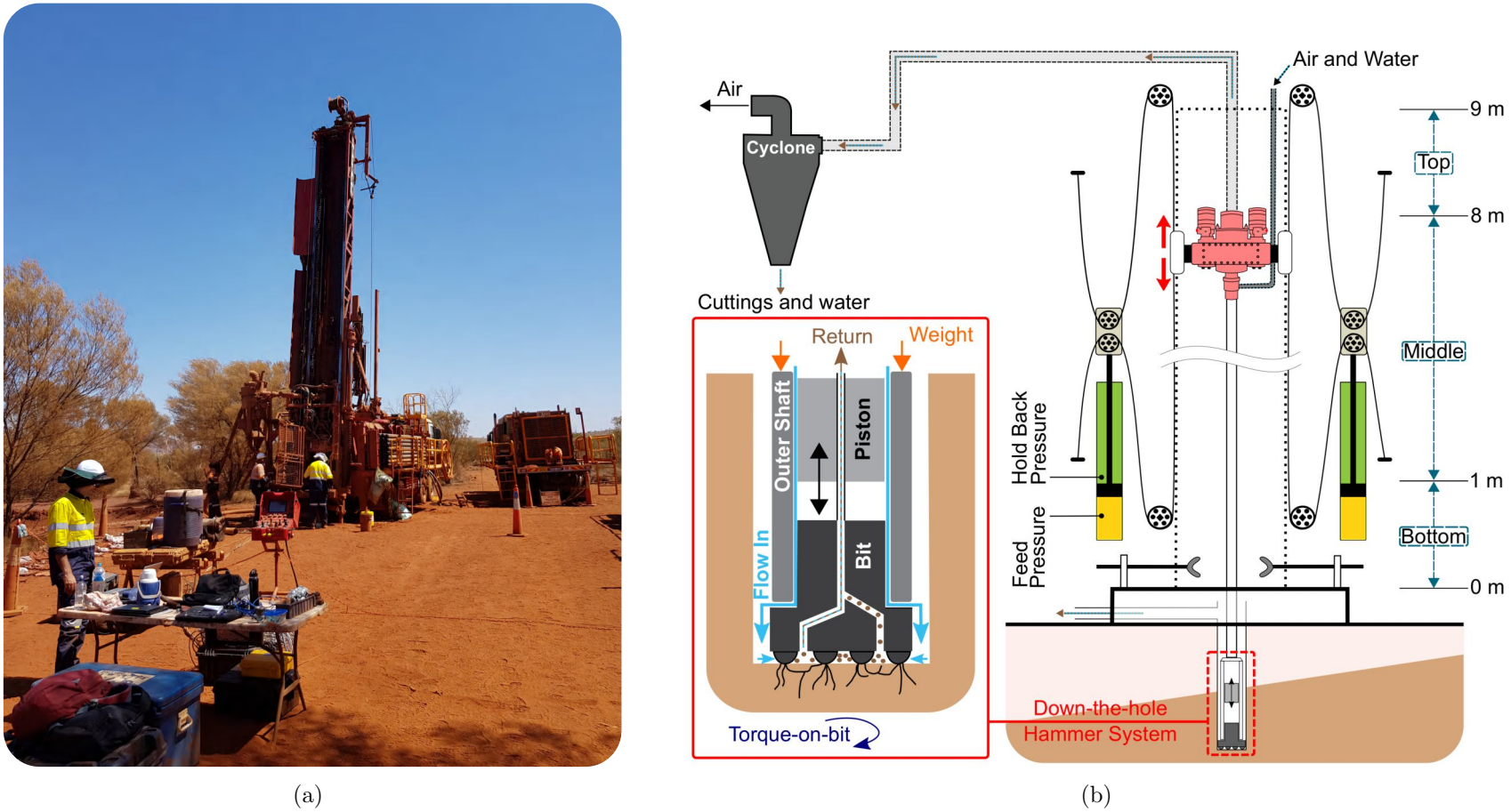

(a) (b)

Figure 3.2: Schramm rotary drilling rig T685WS: (a) drilling crew preparing the equipment prior to the start of operations, and (b) illustration of the reverse circulation drilling system of the rig.

Figure 3.3: Down-the-hole hammer system utilised during the drilling operations: Schramm AD124RC hammer with a 133-millimetre (⌀) drill bit.

Figure 3.4 shows the complete custom-built monitoring system installed on the drilling rig, composed of both standard and high-resolution analog and digital sensors that were installed in strategic locations (refer to Table 3.1 for more details).

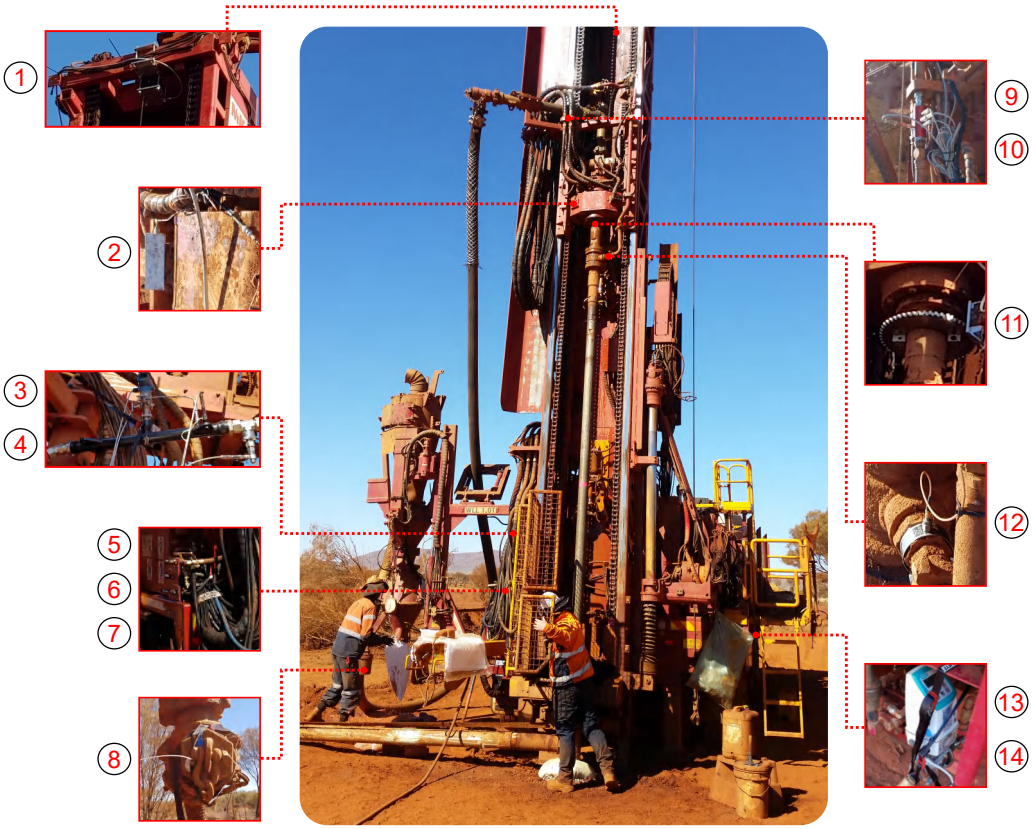

Figure 3.4: Schramm rotary drilling rig T685WS and location of sensors.

ID	Sensor	Parameter	Range	Precision
1	Draw Wire	Rotary Head Position	0-15 m	±0.15%
2	Accelerometer 2	Hammer Harmonics	0-10 g (peak)	±5%
3	Flow (air)	Airflow	0-1500 scfm	±3%
4	Pressure (air)	Air Pressure	0-400 bar	±0.1%
5	Pressure (oil)	Feed Pressure	0-400 bar	±0.1%
6	Pressure (oil)	Hold-Back Pressure	0-400 bar	±0.1%
7	Pressure (oil)	Foot Clamp	0-400 bar	±0.1%
8	Accelerometer 3	Cuttings Return	0-10 g (peak)	±5%
9	Pressure (oil)	Rotational Pressure A	0-400 bar	±0.1%
10	Pressure (oil)	Rotational Pressure B	0-400 bar	±0.1%
11	Rotational Speed	RPM	0-1.7 mm	±10%
12	Accelerometer 1	Hammer Harmonics	0-10 g (peak)	±5%
13	Flow (water)	Water Flow	0-4800 l/min	±0.4%
14	Pressure (water)	Water Pressure	0-400 bar	±0.1%

***** All sensors had 3 distinct data recording protocols that were configured by software: 10 Hz, 1024 Hz (1280 Hz for the accelerometers), and 20 kHz.

Table 3.1: List of sensors installed on the drilling rig.

The rotary head was instrumented with two IEPE accelerometers and also with an SSI (Synchronous Serial Interface) draw wire position sensor that offers a resolution of 38 microns over a full range of 5 metres (refer to Figure 3.5). Furthermore, a rotational speed sensor (1 kHz) with a detection range of 1.7 millimetres was also installed on the rotary head along with a module toothed wheel (with 54 teeth); they were used to estimate the angular velocity of the drill string.

The annulus return flow was not instrumented due to the risk of mechanical damage to the sensors by an air/water flow charged with rock fragments at high velocity.

3.1.2 Data Acquisition System

The standalone modular controller cRIO-9056 (from *National Instruments*) was selected. It runs a Linux real-time operating system with embedded programmable features (field-programmable gate array (FPGA)), and its chassis hosts eight slots

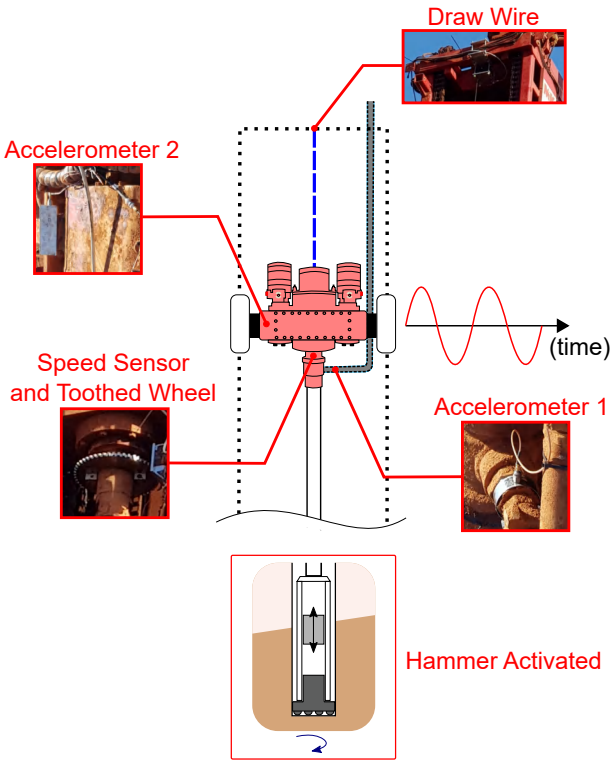

Figure 3.5: Sensors installed on the rotary head. The draw wire sensor and accelerometers were used to capture the drill string dynamics with the intention of detecting the hammer's dominant frequencies.

that support industrial I/O modules. The modular nature of the system provides flexibility to select a variety of sensor types: standard analog, digital, or even specific SSI or IEPE sensors. An Ethernet port allows the system to be connected to a network with all associated communication features and protocols (WebSocket, TCP/IP, etc.). Furthermore, the chassis can also accommodate specific industrial communication modules (CAN and Modbus), or controllers essential in the perspective of automation of the drilling operations.

Figure 3.6 shows the data acquisition system used to record the data. The chassis was mounted inside a robust carry-on case with bulk-head connectors on the outer shell of the case. Table 3.2 presents the modules installed on the cRIO-9056 controller's chassis and the information about the sensors connected to each module:

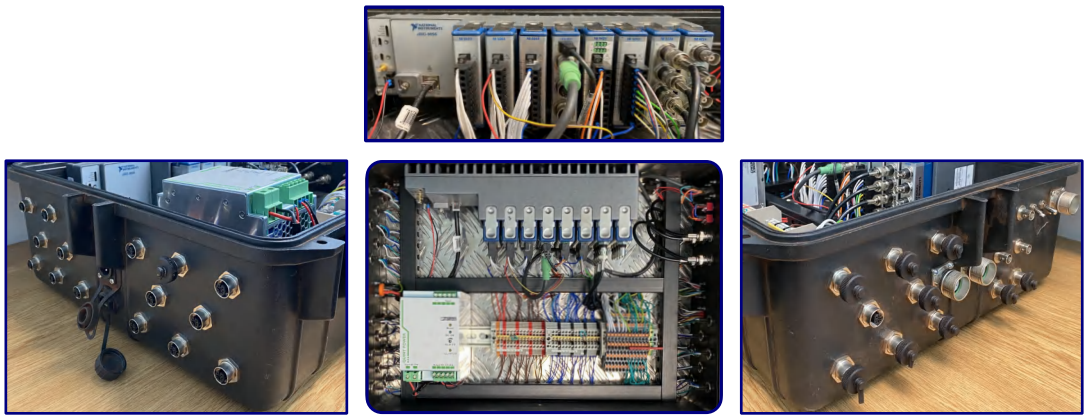

Figure 3.6: Data acquisition system with I/O modules and bulkhead connectors.

Module	Parameter	Sensor	Sensor Type
SEA-9521	Rotary Head Position	Draw Wire	Position
NI-9234	Hammer Harmonics	Accelerometer 1	Accelerometer
	Hammer Harmonics	Accelerometer 2	Accelerometer
	Cuttings Return	Accelerometer	Accelerometer
NI-9421	RPM	Rotational Speed	Hall Efeect
NI-9234	Airflow	Flow (air)	Magnetic Flow
	Air Pressure	Pressure (air)	Pressure
	Feed Pressure	Pressure (oil)	Pressure
	Hold-Back Pressure	Pressure (oil)	Pressure
	Foot Clamp	Pressure (oil)	Pressure
	Rotational Pressure A	Pressure (oil)	Pressure
	Rotational Pressure B	Pressure (oil)	Pressure
	Water Flow	Flow (water)	Magnetic Flow
	Water Pressure	Pressure (water)	Pressure

Table 3.2: Information about the sensors connected to each module installed on the cRIO-9056 controller.

Data Recording

The drilling data was recorded following three distinct protocols:

- all data were recorded continuously at 10 Hz,
- selected data[1] were recorded for two minutes at 1 kHz,
- and selected data were recorded for 30 seconds at 20 kHz.

[1]The drill operator selected the data to be recorded (while drilling).

A dedicated LabVIEW real-time engine software was developed in order to operate the cRIO-9056 controller. The code records the data into binary TDMS (Technical Data Management Streaming) format files and communicates via the Ethernet port to the network. Additionally, a LabVIEW user interface was also created, and the application program was installed on a laptop to communicate with the real-time engine and display the data in live charts.

In order to reduce the risk of possible file corruption during the data recording, the software logged the real-time data into binary files with a maximum size of 1 MB. The file name indicates the type of data (low (10 Hz), medium (1 kHz), or high (20 kHz) sampling rate), as well as the start day and time.

3.2 Data Pre-processing

As mentioned previously, the data were recorded at different sampling rates and saved into numerous files. Before starting the data analysis, the first step was to merge all files under a single platform. The software DREAM (EPSLOG, 2023) was used to process the recorded data.

3.2.1 Drilling Parameters Estimation

Algorithms and functions implemented in the software MATLAB (MathWorks, 2023) were used to estimate the following drilling parameters:

- bit depth and hole depth,
- rate of penetration (ROP),
- weight-on-bit (WOB) and torque-on-bit (TOB).

The parameters angular velocity (RPM), inlet flow and inlet pressure (water and air) were measured directly with sensors (refer to Table 3.1).

Bit Depth and Hole Depth

The algorithm to estimate the bit depth and hole depth parameters is detailed in Appendix A. Such parameters were derived (i) from the rotary head position measurements and by detecting (ii) when a rod is added to (or removed from) the drill string and (iii) when the drill bit touches the borehole bottom (immediately before drilling starts).

Figure 3.7 shows an example of data associated with the drill operator adding and removing a rod, step by step:

1. The drill string is not attached to the rotary head (indicated by the foot clamp sensor). In that instance even if the rotary head moves, the bit and hole depths remain unchanged.

2. Angular rotation and a steep increase in torque indicate that the drill operator is making up a connection.

3. With the drill string attached to the rotary head, the drill operator releases the foot clamp. He then turns on the airflow and rotates the drill string, indicating that he is about to move the drill string downwards to resume drilling.

4. The drill operator moves the drill string downwards.

5. The rotary head is moving downwards, and eventually the bit depth equates to the hole depth, from which any downward movement of the rotary head indicates that the borehole is being drilled forward.

6. The drill operator stops drilling and moves the drill string upwards.

7. A decrease in the foot clamp pressure indicates that the foot clamp is engaged in order to hold the drill string.

8. The drill operator breaks down the connection between the rotary head and drill string. Rotation combined with a negative value of torque indicates that the rotation direction is anticlockwise.

9. The drill operator moves the rotary head upwards (preparing to add an extra rod to the drill string).

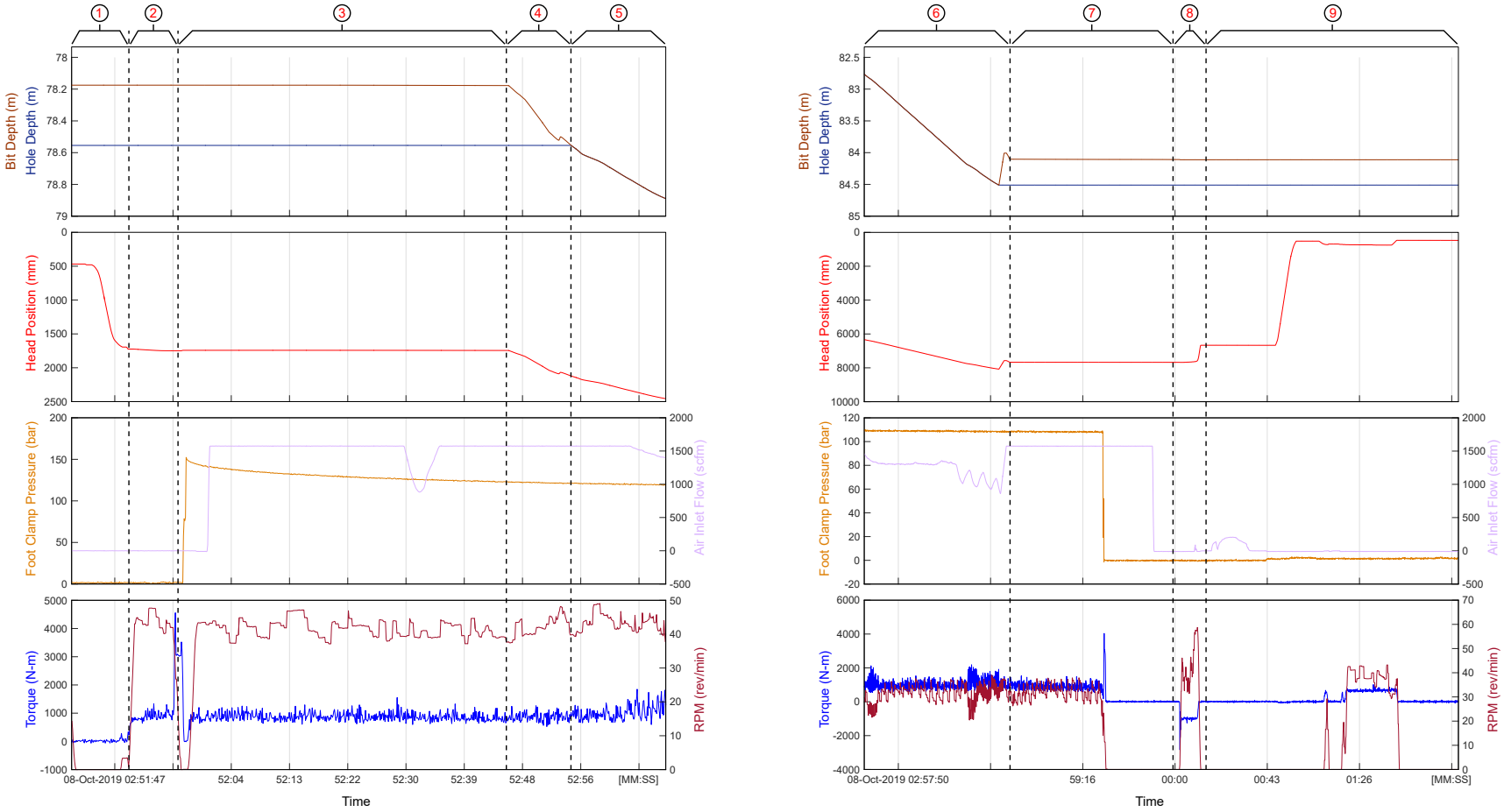

Figure 3.7: Step-by-step procedure to add (left figure) and remove (right figure) a rod. The algorithm detects each step to update the bit depth and the hole depth parameters; it also detects when the drill bit is in contact with the borehole bottom.

Rate of Penetration

The rate of penetration (ROP) is derived from a best linear fit between the hole depth and time over a time window equivalent to one drill bit revolution (refer to Figure 3.8), which varies with the mean angular velocity. In real time, the gradient is computed with a moving point-by-point linear fit. The high resolution and considerably low noise-to-signal ratio of the SSI sensor mean that a moving linear fit yields a robust estimate of the surface feed rate with small dispersion.

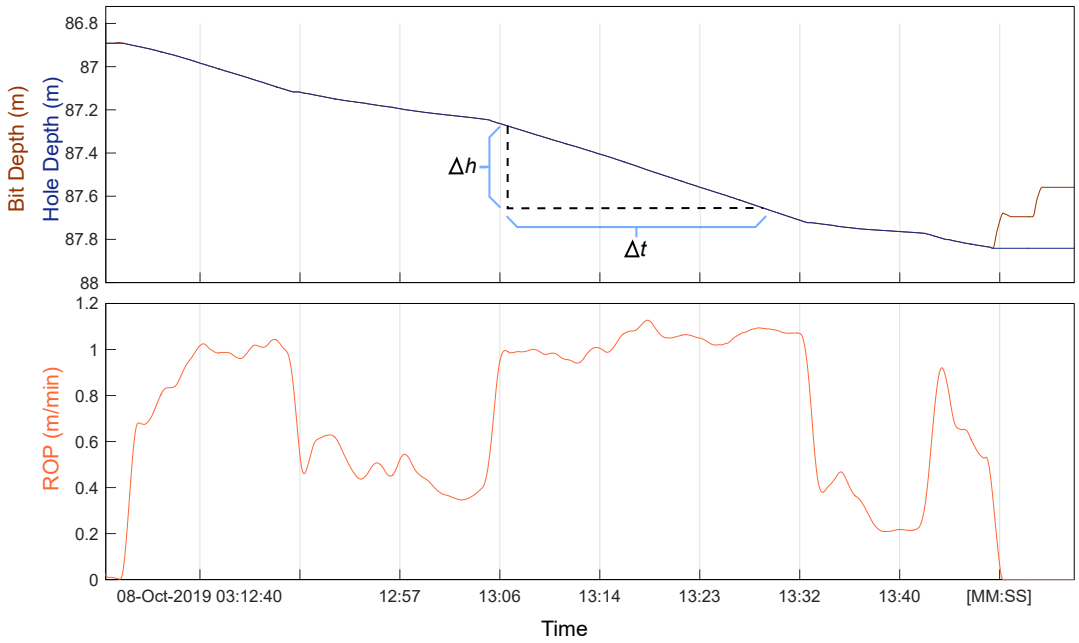

Figure 3.8: Rate of penetration estimated from the hole depth parameter.

Weight-on-Bit and Torque-on-Bit

To estimate the weight and torque applied to the bit, the thrust and torque applied by the rotary head to the drill string (at the surface) are initially calculated.

The thrust N reads:

$$N = 2(F_f - F_h) \tag{3.1}$$

where the feed force F_f and the hold-back force F_h are defined as

$$F_f = p_f \left(\frac{\pi (D_1)^2}{4} \right) \tag{3.2}$$

$$F_h = p_h \frac{\pi}{4} \left(D_1^2 - D_2^2 \right) \tag{3.3}$$

with p_f and p_h being the feed and hold-back pressures, respectively.

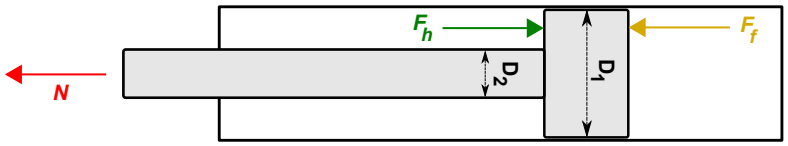

Figure 3.9: Forces acting on the hydraulic piston (refer to Figure 3.2 (b)).

The output torque T generated by the rotary head reads:

$$T = \frac{(p_A - p_B)G}{2\pi} n \frac{H_2}{H_1} \eta \tag{3.4}$$

where p_A and p_B correspond to the hydraulic pressures at ports A and B of the motor, G the geometric displacement of the motor ($G = 0.000629 m^3/rev$), n the number of motors mounted in parallel ($n = 2$), H_2/H_1 the hydraulic motor-to-rod string drive ratio (H_2/H_1=68/18), and η the overall motor efficiency ($\eta = 0.8$).

The weight-on-bit W and torque-on-bit T at time t read:

$$W(t) = N(t) - N_0 \tag{3.5}$$

$$T(t) = T(t) - T_0 \tag{3.6}$$

where N_0 and T_0 are the thrust and torque off-bottom just before the drill bit touches the borehole bottom, ideally with air and water flow rates as well as angular velocity steady and set to target values.

Figure 3.10 illustrates the evolution of the thrust and torque over time, from the moment the drill bit is still off-bottom until the drill string starts moving

downwards and drilling occurs:

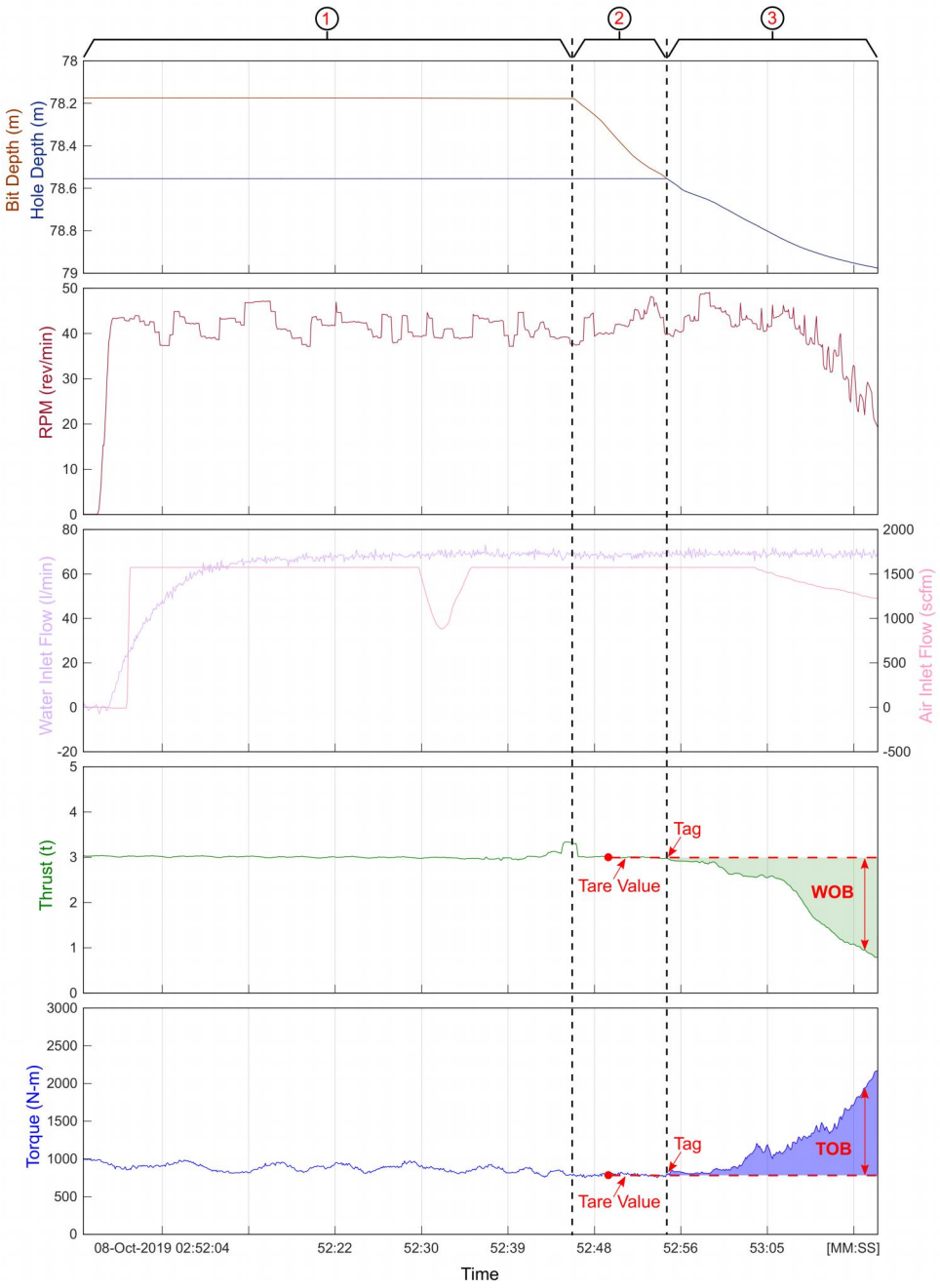

Figure 3.10: Example of thrust (N) and torque (T) measurements while the drill bit touches the borehole bottom and drilling commences. The thrust (N_0) and torque (T_0) measured off-bottom are used to estimate the WOB and TOB, respectively.

1. After adding a new rod to the drill string, the drill operator starts rotating

the drill string, and he also turns on the airflow and water flow.

2. Then, the drill operator lowers the drill string in order to start the drilling process. Before the drill bit touches the borehole bottom, the thrust (N_0) and torque (T_0) tare values are recorded.

3. Finally, the parameters weight-on-bit and torque-on-bit are simply derived from Equations 3.5 and 3.6.

The algorithm to estimate the weight and torque applied to the bit is detailed in Appendix B.

3.3 Results

This section presents the outcomes of the drilling data analysis.

3.3.1 Energy Consideration to Flush Rock Cuttings

The overall flow of water and air through the system was monitored by measuring pressure and flow rate at the inlets (water and air), and pressure on the inner tube return line (just before the hydrocyclone). However, the annulus flow rate and pressure were not monitored, as mentioned previously. Also, the inlet airflow sensor saturated during experiments at 1500 SCFM while the booster system (compressor) operated at a flow rate considerably higher, meaning that for some period of time, it can only be inferred that the inlet flow rate is larger or equal to 1500 SCFM.

The water flow rate varied between 50 and 100 l/min, interestingly about twice the value that the drill operator expected (within a range between 20 and 30 l/min). Figure 3.11 shows how the air and water inlet pressures evolved proportionally with depth while drilling an equivalent of one-rod length (6 metres). The air and water inlet flow rates take a few seconds to set to the target value. As expected, the air inlet flow rate sensor became saturated at around 1500 SCFM, but the flow rate was presumably higher.

The steady-state value of the air pressure—before touching the borehole bottom—is likely to represent the pressure required to push the air and the water through the system (inner pipes, hammer system, and annulus) with the hammer system in flushing mode, and one can legitimately assume that the inner pipe and annulus are free of cuttings. However, with no reliable measure of the airflow rate, one cannot draw a comprehensive explanation. Interestingly, the pressure increases steadily as the bit drills ahead until the drill operator pulls the hammer system off-bottom to flush the cuttings to the surface, refer to Figure 3.12.

The drill operator systematically flushes the borehole three times (every 2 metres) while drilling an equivalent of one-rod length, with the air pressure response

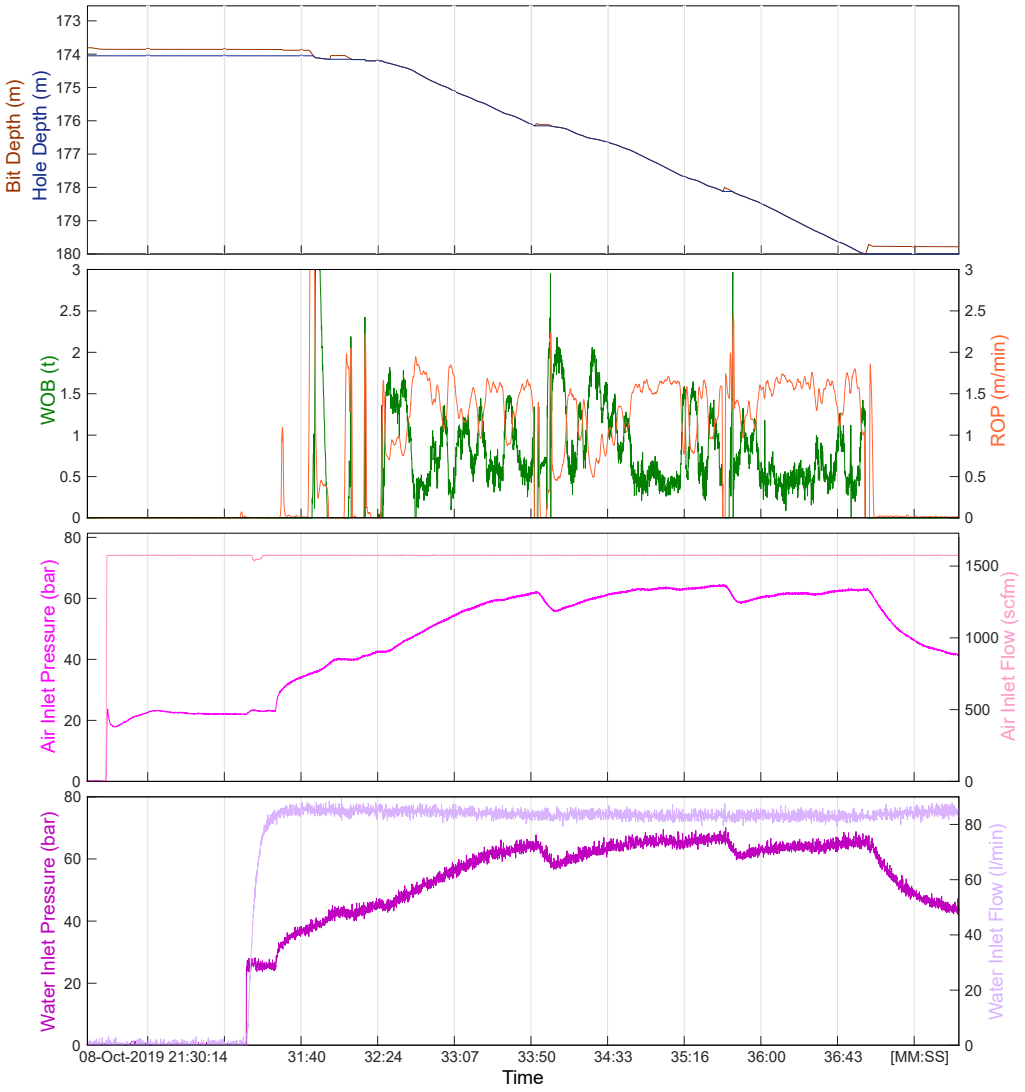

Figure 3.11: Air and Water inlet pressures evolving with depth while drilling an equivalent of one-rod length.

being consistent from rod to rod. One would expect the response to vary with depth, as the power required to flow air through the rods and annulus should increase with depth. Unfortunately, the sensor for measuring airflow became saturated for an extended period of time and it is not possible to compute a measure of power. However, as the operator drills ahead, a steady and significant pressure increase suggests that the energy required to flush cuttings and water increases steadily.

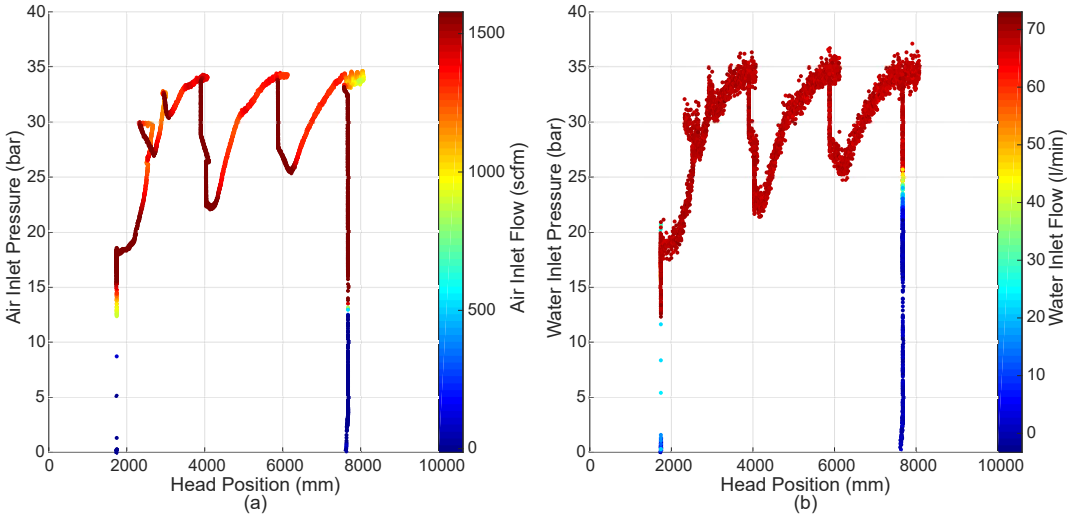

Figure 3.12: Data pertaining to Hole 1 (from the depth of 78 to 84 metres): (a) air inlet pressure as a function of head position, and (b) water inlet pressure as a function of head position.

Flushing the Rock Cuttings

As the bit drills ahead, the accumulation of cuttings tends to increase around the drill bit face and stagnate in the inner tube or annulus on the return path. In order to flush the cuttings to the surface, the drill operator moves the drilling assembly upwards (off-bottom) until the hammer becomes inactive, which in turn increases the airflow velocity inside the drill pipe.

Figure 3.13 shows an example of the data referring to the accelerometer and pressure transducer on the return line, before the hydrocyclone, immediately after the flushing mode was activated. The increase in the signal amplitude is attributed to impacts (disturbances) associated with the arrival of cuttings at the surface.

The steady-state value of pressures—for air and water—is approximately 40 bar for both holes (for the section of the holes drilled with the booster activated). The saturation of the airflow sensor limited the data analysis; assuming that the airflow rate ranges from 2000 to 2500 SCFM, the power consumption is estimated to be from 350 kW to 430 kW to push the drilling fluid through the reverse circulation system of the drilling rig, in order to bring the cuttings to the surface.

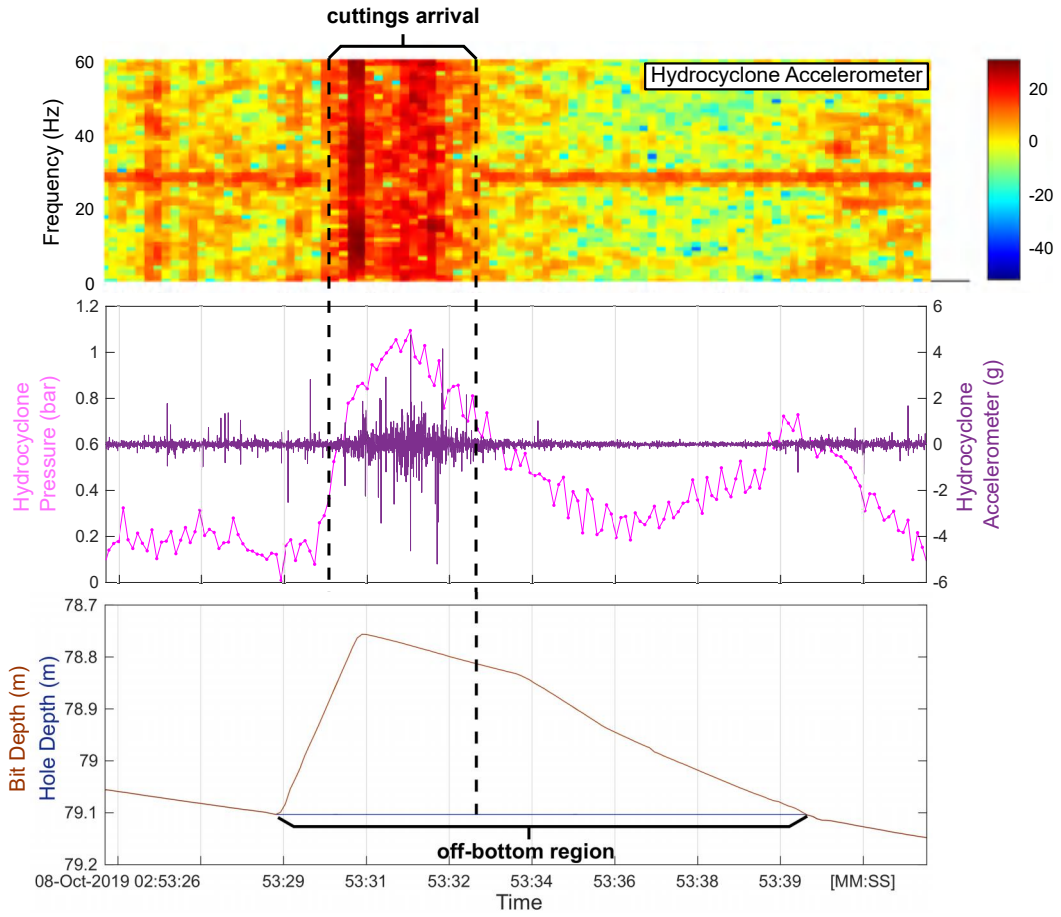

Figure 3.13: Example of data recorded while the drill operator pulls the drilling assembly off-bottom. The arrival of cuttings at the surface is linked to an increase in the energy associated with the accelerometer readings immediately before the hydrocyclone.

Furthermore, both parameters air and water inlet pressures increase steadily with depth (time) up to around 65 bar, as the bit drills ahead. The power consumption to compress the air (in the drill pipe) is estimated to be from 390 kW to 490 kW.

3.3.2 DTH Hammer System Activation

Figure 3.14 illustrates the moment when the drill bit touches the borehole bottom. The WOB and TOB increase, and the hammer becomes active after a short period of time. The measurements referring to the rotary head acceleration already hint that the system dynamic response changes once the hammer is activated; the

amplitudes of the accelerometer readings grow, and a clear dominant frequency arises. The hammer system becomes active once an initial weight is applied to the bit; this weight is required to close the distance between the drill bit and the outer shaft of the hammer. Figure 3.15 shows what occurs from the moment the drill bit touches the borehole bottom until the hammer system is activated:

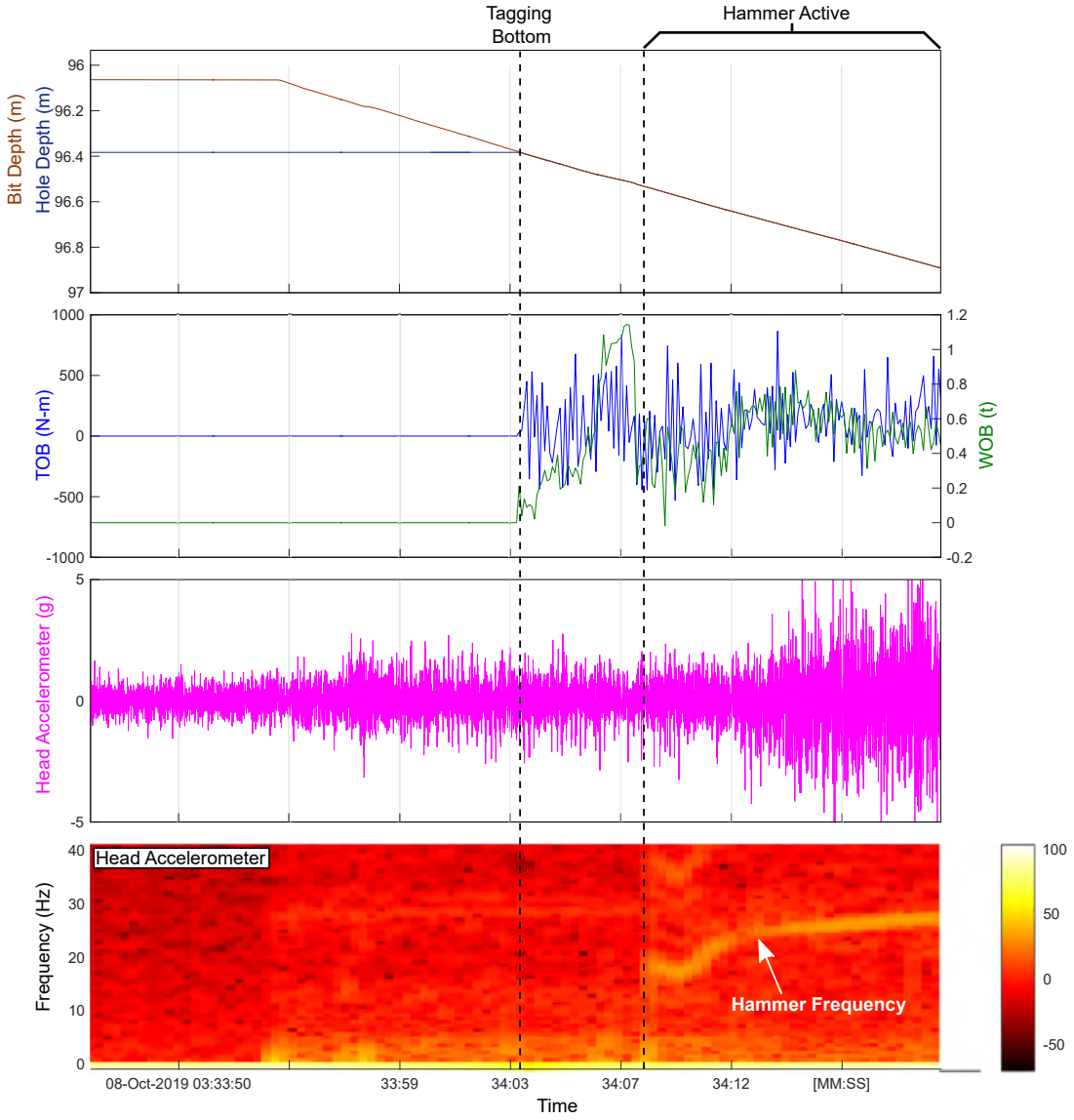

Figure 3.14: The estimated parameters *bit depth*, *hole depth*, *WOB* and *TOB* assist on the identification of down-hole activities. Note that the hammer system does not become active immediately after the drill bit touches the borehole bottom.

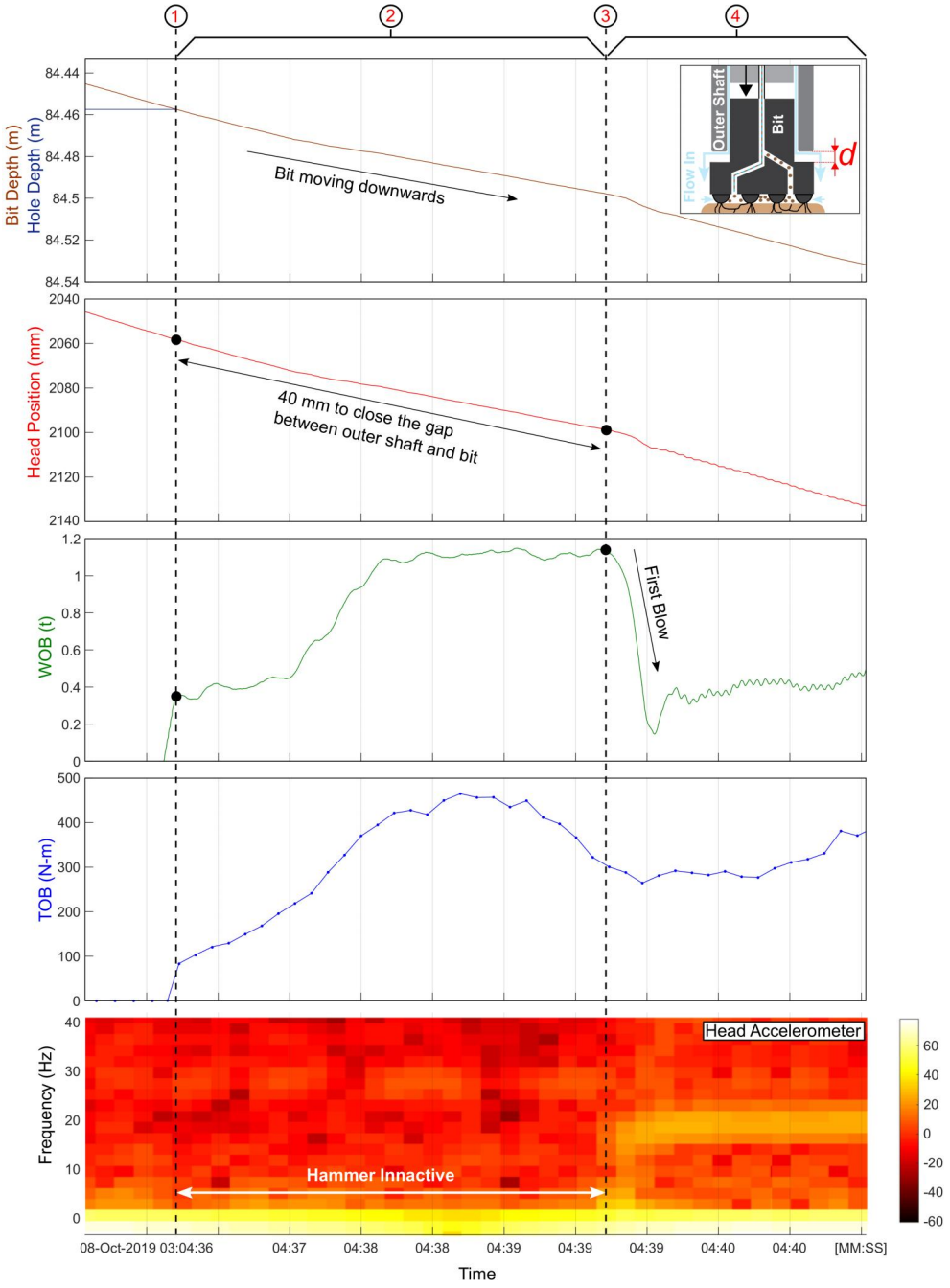

Figure 3.15: Evolution of parameters from the moment the drill bit touches the borehole bottom until the hammer becomes active.

1. Before touching the borehole bottom, the drill bit is hanging off the hammer and air flows freely through it (flushing mode). Then, the drill operator lowers the rotary head. Note that there is an increase in weight-on-bit once the bit touches the borehole bottom, as part of the drilling assembly weight

is transferred to the borehole bottom.

2. The drill operator continues to lower the rotary head, and the bit shaft slides into the hammer housing. The weight-on-bit initially remains constant while the rotary head is lowered over a distance of about 20 mm. Then, the weight-on-bit increases and stabilises at about 1 ton, which is considerably larger than the weight of the bit itself (which is around 20 kg). This weight-on-bit is likely to correspond to the force required to overcome the force exerted by the fluid jet (on the bit), which can be defined as the fluid rate of change of momentum in the direction of the force (refer to Figure 3.16):

$$F_x = \frac{p_{Initial} - p_{Final}}{t} = \dot{m}[V_{0_{fluid}} - V_{fluid}] = \rho A V^2 \tag{3.7}$$

where p is the fluid momentum, $\dot{m}$ is the mass flow rate, ρ is the fluid density, A is the area of the nozzle, and V is the fluid velocity.

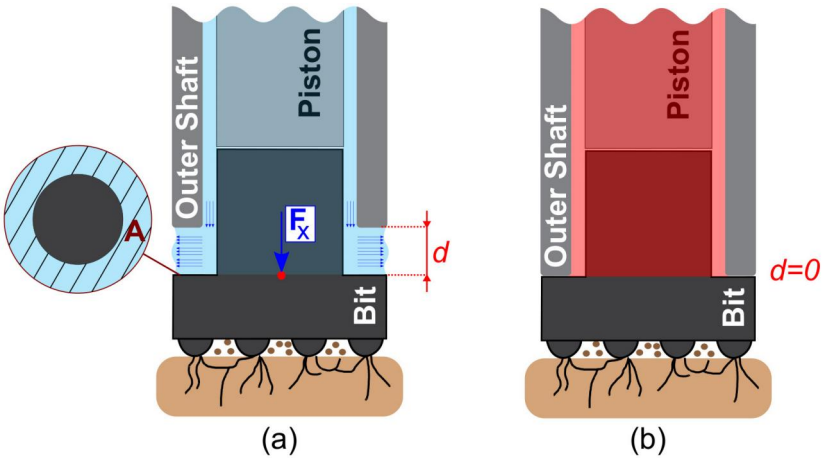

Figure 3.16: Distance between outer shaft and drill bit. (a) Drill bit on flushing mode, and (b) hammer system about to become active due to the increase of pressure in its front chamber.

3. Eventually, after a relative stroke of about 40 mm—consistent with a standard bit shank stroke—the distance gap between the outer shaft and drill bit is closed; during such period of time, the pressure builds up inside the front chamber of the hammer system (refer to Figure 3.16). As a result, the

weight-on-bit drops to almost zero and the hammer becomes active. As the hammer is activated, the force required to cease the fluid flow vanishes.

4. The rotary head continues to move downwards and the borehole is excavated forward by the DTH hammer system. Interestingly the torque-on-bit follows a pattern similar to the weight-on-bit, suggesting that while "closing the hammer" the bit buttons are scrapping/cutting the rock surface.

3.3.3 Down-hole System Dynamics from Surface Measurements

Due to the high precision and sampling rate of the draw wire sensor (1024 Hz)[2], its recorded signal reveals a unique signature in which a clear periodic step response is observed during drilling (refer to Figure 3.17). The dominant frequency of the signal not only closely resembles the dominant frequency of the rotary head acceleration (acquired with the accelerometers), but it also matches closely with the expected piston impact frequency (ranging between 20 and 30 Hz). Therefore, it is possible to claim with confidence that the rotary head position captures the drill bit displacement at each piston impact cycle. A literature search revealed no similar outcomes, meaning this result is unique. It further emphasises the added value of using a high sampling rate data acquisition system. Furthermore, it opens up the opportunity for the development of data-driven strategies to monitor in real time the operational statuses and parameters of the DTH hammer system during drilling.

[2]The 20 kHz signal of the draw wire sensor did not reveal any additional relevant information in comparison to the 1024 Hz signal (during drilling). Therefore, the data sampled at 1024 Hz was selected for the analysis.

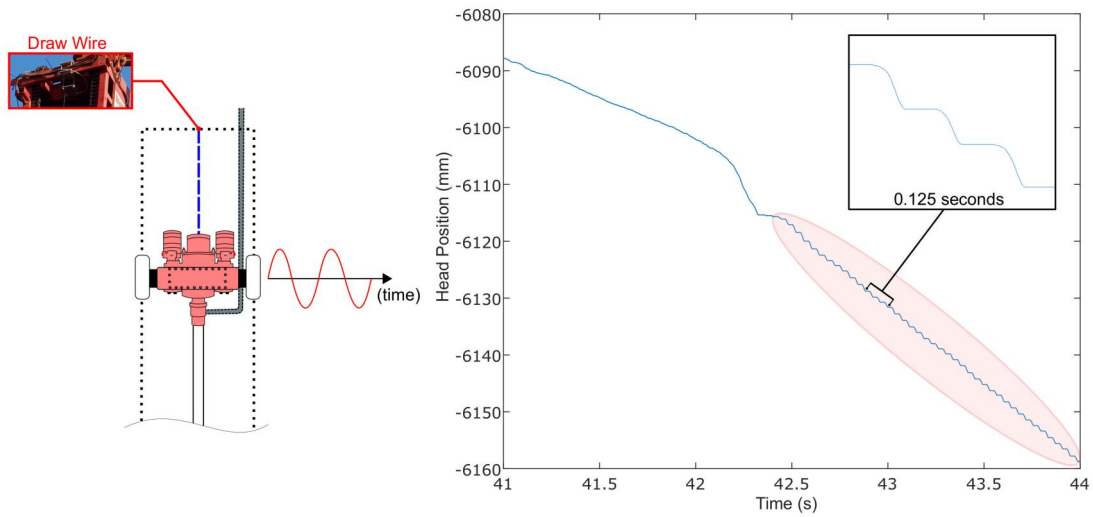

Figure 3.17: Rotary head position signal reveals a periodic step response during drilling.

3.3.4 Proposed Method for Real-Time Monitoring of the DTH Hammer System

For our research group, it is of great interest to be able to detect precisely (in real time) the moment the hammer system becomes active and to estimate operational parameters, such as piston impact frequency and bit penetration per piston impact. Providing such information for the drill operator during the drilling operations would be of great benefit, or it could even be used as input on data-driven drilling optimisation strategies developed in the future. The algorithm I developed for real-time monitoring of the DTH hammer system is detailed in Appendix C. Figure 3.18 shows how the algorithm's output is comparable to the time-frequency representation of the signal from one of the accelerometers installed on the rotary head.

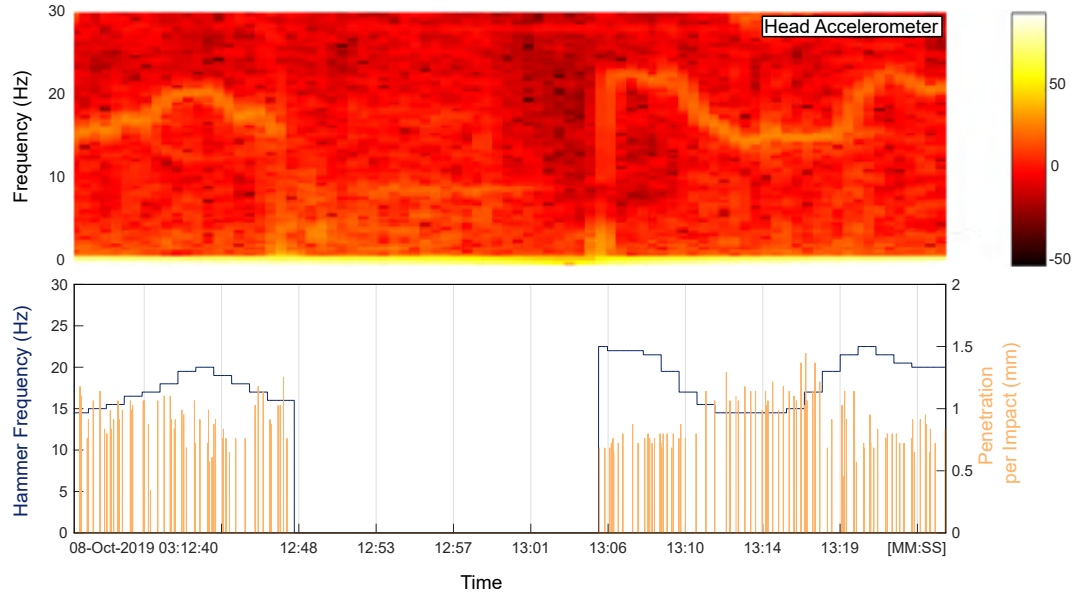

Figure 3.18: Comparison between the time-frequency representation of the signal pertaining to the accelerometer installed on the rotary head and the output of the proposed algorithm to estimate the piston impact frequency and bit penetration per impact.

3.3.5 Evidence of the ODS Phenomenon

The analysis of the drilling data revealed that the drill operators consistently applied excessive weight-on-bit throughout the entire drilling operations. Nonetheless, it was possible to observe the ODS phenomenon in several instances.

Figure 3.19 represents two distinct extensive sections of Hole 1, where the rate of penetration decreases with the increase of weigh-on-bit. The drill operator was incapable of maintaining the drilling rig operating at its optimum level of performance. Furthermore, Figure 3.19 also shows the effect that lithology can have on the drilling performance; the rate of penetration appears to be related to the shale content (wireline gamma ray readings)[3]. This result stresses that drilling optimisation requires not only a holistic approach with real-time monitoring and tuning but also post-mortem analysis that can help refine real-time strategies from one borehole to another.

[3]Gamma ray readings were available only for Hole 1.

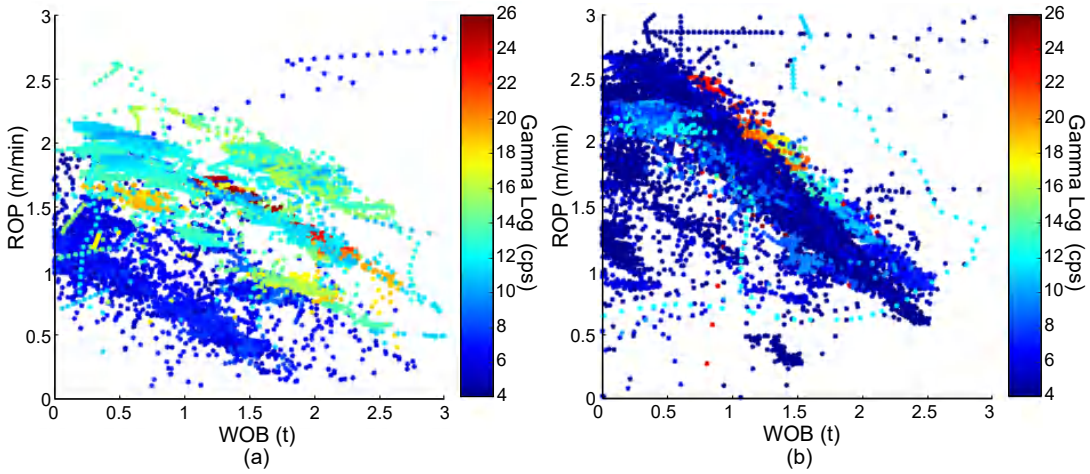

Figure 3.19: WOB versus ROP with respect to the gamma-ray readings (colour spectrum) (Hole 1): (a) section from the depth of 86 to 97 metres, and (b) section from the depth of 134 to 150 metres.

Another example of the ODS phenomenon occurrence is shown in Figures 3.20 and 3.21; both examples pertain to the same drilled section[4]. The ROP is maximised for a specific WOB and then starts to decrease while the drill operator continues increasing the weight applied to the bit; the TOB also increases with the WOB (refer to Figures 3.20 (a) and (b)). As shown clearly from the data, a change in the input thrust influences the drilling response of the down-hole system. Note in Figure 3.20 (c), for instance, that the angular velocity was affected by the excessive axial load applied to the down-hole system, indicating an insufficient capacity of the equipment to maintain the desired angular velocity set by the operator.

Figures 3.21 (a) and (b) show how the hammer frequency and indexing angle parameters changed throughout the drilling process. It can be inferred that the piston impact energy varies according to the piston impact frequency; moreover, a change in hammer frequency or angular velocity affects the drill bit indexing angle[5]. One can argue that both parameters could be related to the occurrence

[4]Area highlighted in Figure 3.21.

[5]Indexing angle (I_a) is the angular displacement of the drill bit between two subsequent piston impacts: $I_a(^\circ) = \frac{\Delta\theta}{f_p}$, where $\Delta\theta$ ($\frac{degrees}{s}$) is the angular velocity of the drill bit and f_p (Hz) is the piston impact frequency.

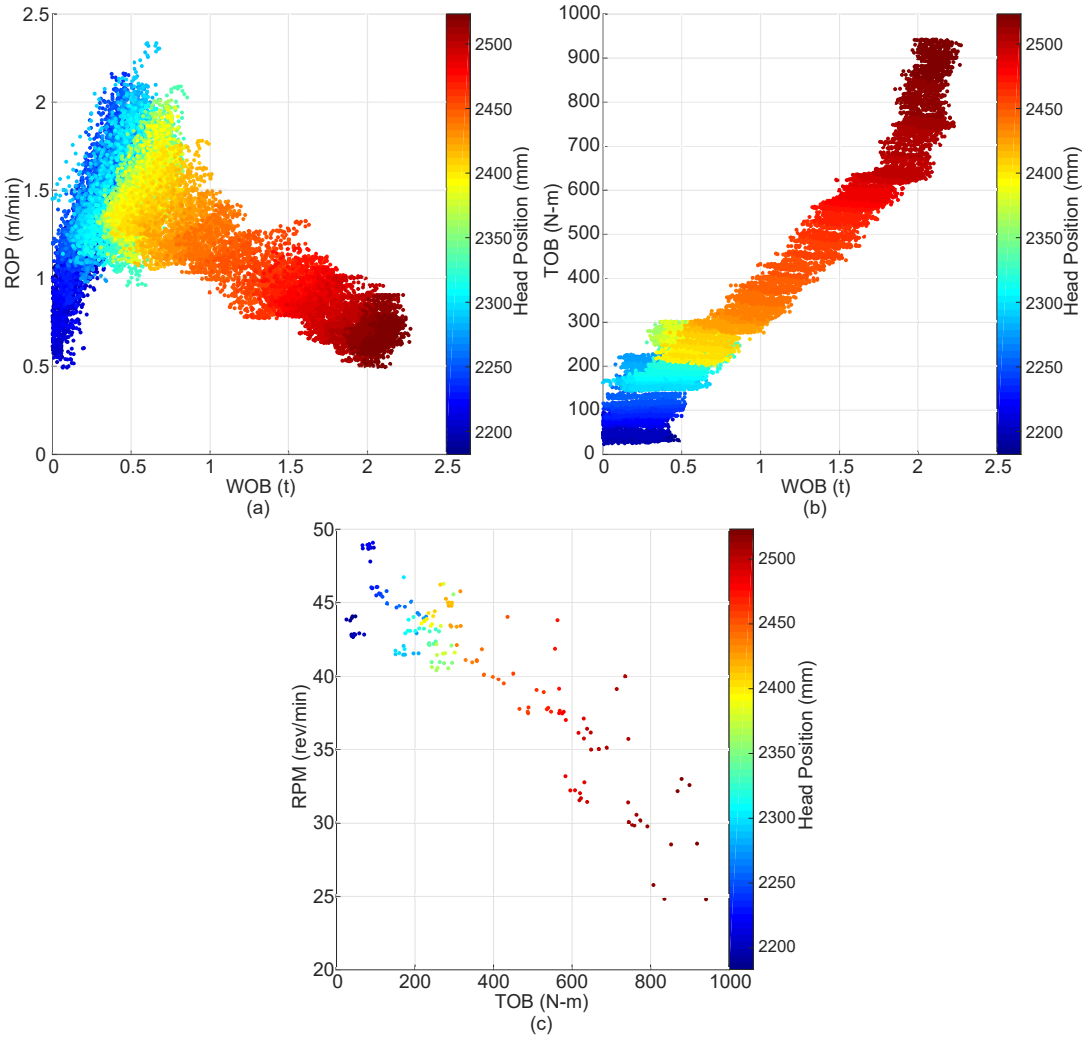

Figure 3.20: (a) Example of the ODS phenomenon; WOB versus ROP with respect to the head position (colour spectrum). (b) TOB versus WOB with respect to the head position (colour spectrum), and (c) angular velocity decreasing due to excessive TOB; RPM versus TOB with respect to the head position (colour spectrum).

of the ODS phenomenon; however, while the hammer frequency and the indexing angle change monotonically during the drilling process, the rate of penetration has a fourfold increase up to the peak— at about 2.2 m/min—then it decreases back to approximately 0.5 m/min.

The accumulation of loose material (cuttings) inside the borehole could be affecting the overall drilling performance. As shown in Figure 3.21, the signals from the sensors installed on the hydrocyclone (pressure transducer and accelerometer)

do not indicate any significant arrival of cuttings at the surface during the drilling process (highlighted area in Figure 3.21). During the same period of time, the air and water inlet pressures increase, as shown in Figures 3.21 (c) and (d). An excessive weight applied to the bit may influence the discharge of drilling fluid from the hammer system to the borehole, affecting the borehole cleaning process; an accumulation of loose material between the drill bit and the borehole bottom could affect the transmission of energy (from the bit to the rock formation) during each percussive cycle. Note that the signals of the accelerometer and pressure transducer installed on the hydrocyclone only increase when the drill operator pulls the drill bit off-bottom (refer to Figure 3.21), which indicates the arrival of cuttings at the surface.

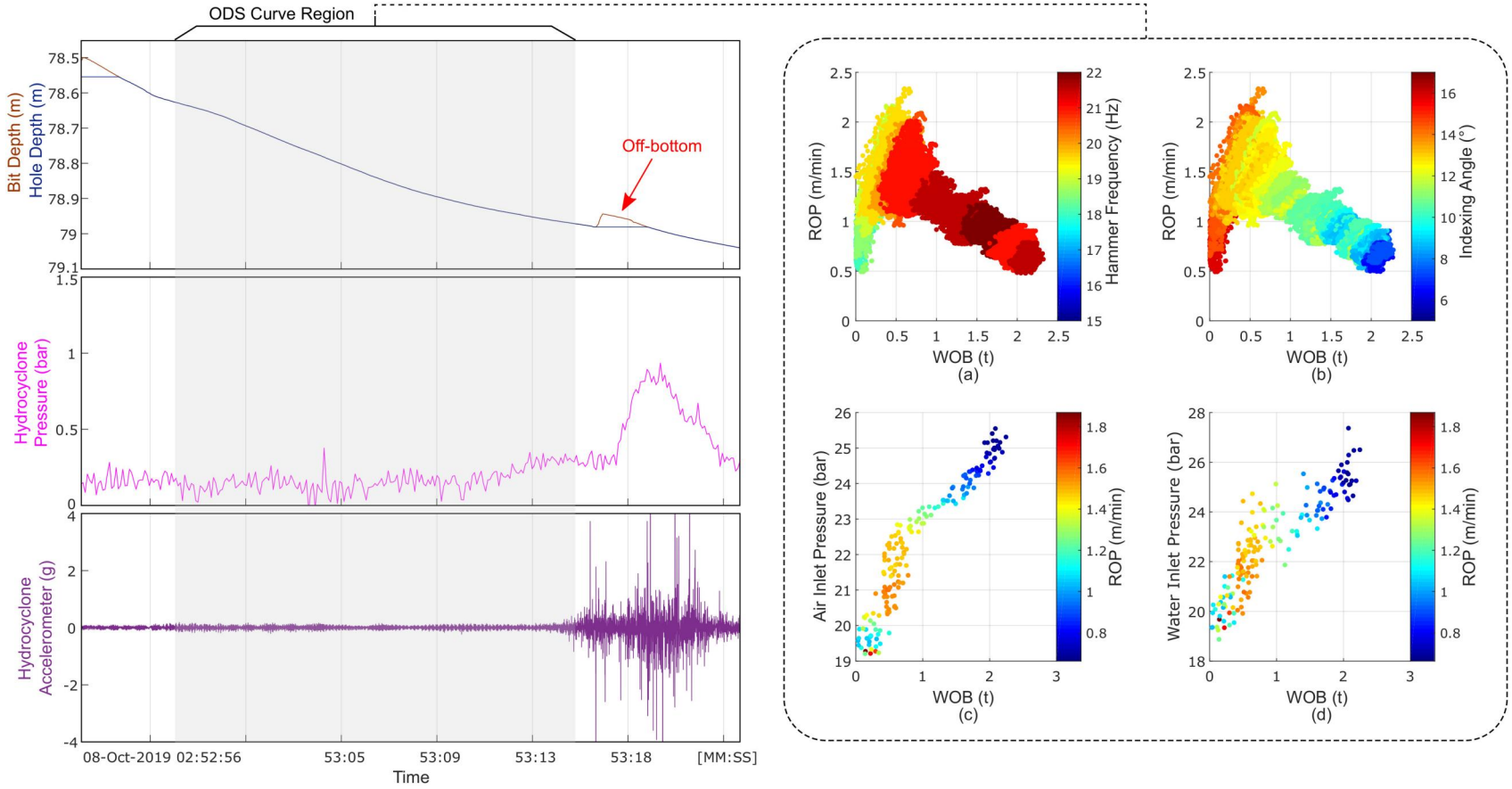

Figure 3.21: Bit depth, hole depth, and the signals from the pressure transducer and accelerometer installed on the hydrocyclone (parameters evolving in time). The ODS curves pertain to the highlighted section: curves with respect to the (a) indexing angle and (b) piston impact frequency readings (colour spectrum), respectively. (c) Air and (d) water inlet pressures increasing with WOB (while drilling), which could indicate a restriction of fluid flow inside the drill pipes due to excess material (cuttings) inside the borehole.

3.3.6 Distinct Drilling Responses

A meticulous analysis of the rotary head position signal revealed several drilling regimes:

- **Regime 1** - As shown in Figure 3.22, this regime is characterised by a clear hammer activity with a periodic motion and distinct plateaus with the rotary head at full rest between impacts. This type of signature could be related to well-consolidated and hard formations. In some instances, when excessive weight is applied to the bit, the *penetration per impact* parameter becomes inconsistent.

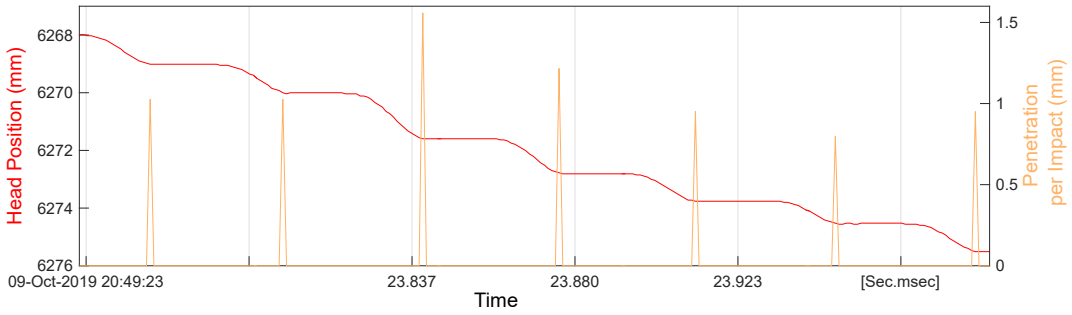

Figure 3.22: Evolution of the rotary head position in time during drilling: **Regime 1**.

- **Regime 2** - This drilling regime is characterised by inconsistent and occasionally reduced hammer activity, with the bit still drilling ahead between successive impacts, probably by shearing the rock as suggested by an increase in the mean torque (refer to Figure 3.23). It normally occurs when excessive weight is applied to the bit. In some cases, however, this regime leads to high ROP or takes place within the *optimum state* region of the ODS curve, which could indicate soft or unconsolidated formation.

- **Regime 3** - As shown in Figure 3.24, this drilling regime presents hammer activity accompanied by vertical rebound of the rotary head—upward movement of the rotary head opposite to the direction of drilling—most

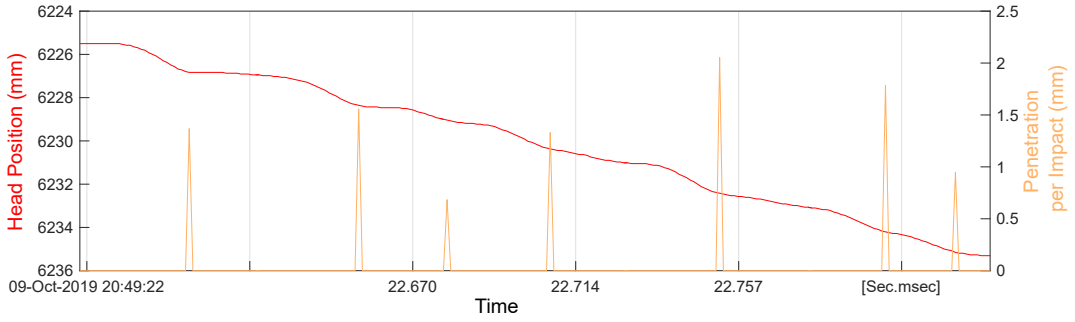

Figure 3.23: Evolution of the rotary head position in time during drilling: **Regime 2**.

probably due to the low weight applied to the bit, which leads to inadequate contact of the drill bit with the rock formation, resulting in high hammer assembly vibration (rebound-type signature). This drilling regime could be detrimental to the drilling rig (refer to Figure 3.26).

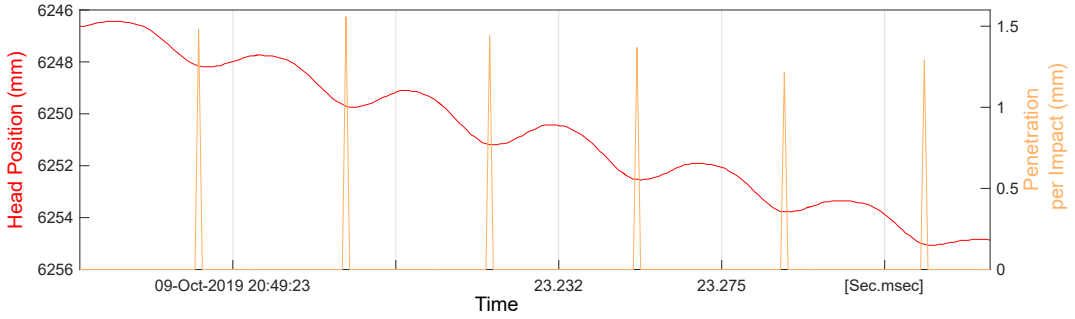

Figure 3.24: Evolution of the rotary head position in time during drilling: **Regime 3**.

- **Regime 4** - This drilling regime occurs when the hammer system suddenly becomes inactive and, consequently, the bit drills purely by shearing the rock. Such a regime was observed taking place on different occasions. For example, Figure 3.25 shows how the applied weight-on-bit can affect the drilling response. Due to an increase in WOB, the hammer became inactive, and the rate of penetration decreased. For a period of time, the drilling process occurred without the percussion action of the hammer system.

Figure 3.26 shows the rotary head position signal in different regions of the ODS curve. **Regime 3** occurred for low WOB, before the peak of the curve

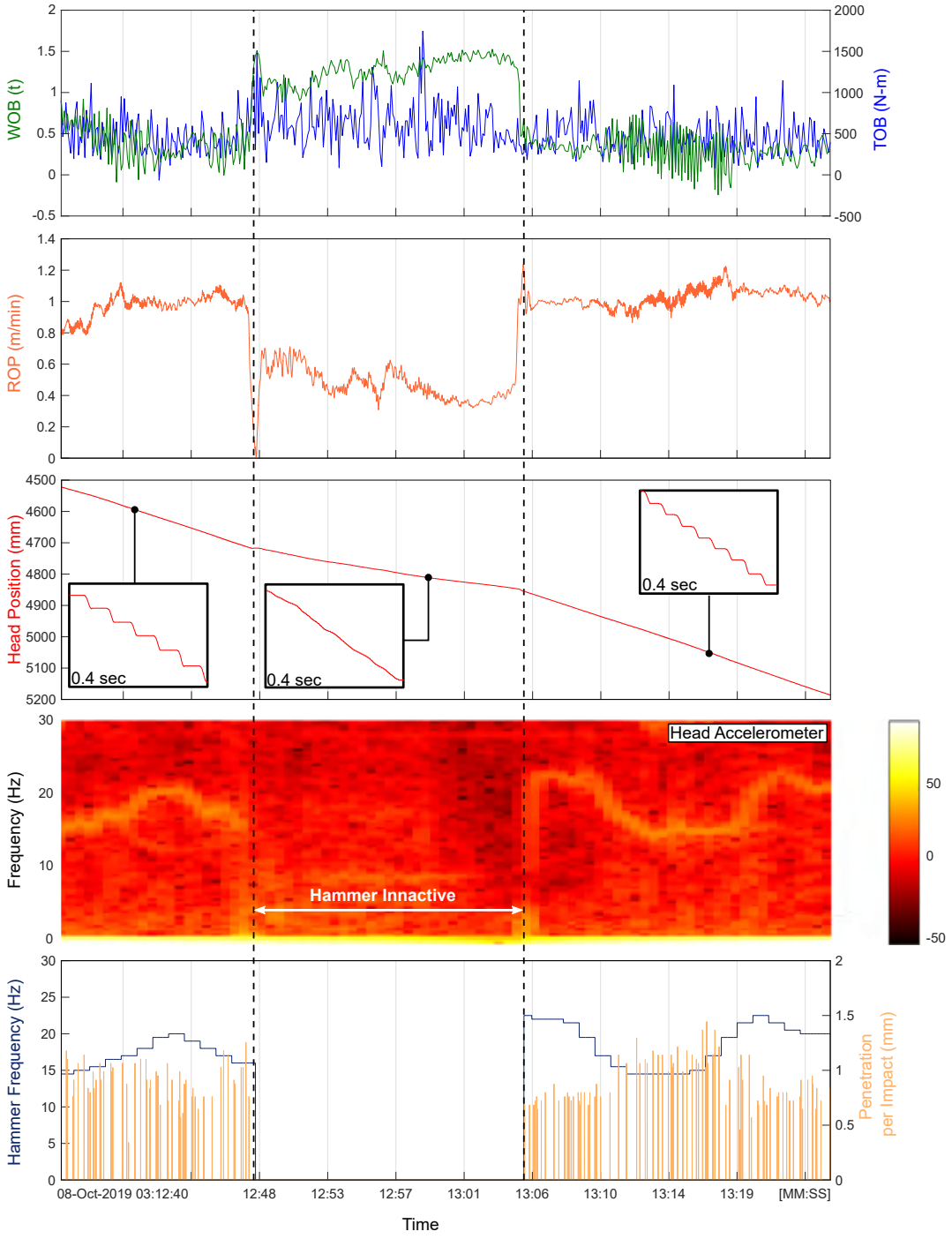

Figure 3.25: Influence of WOB on the drilling performance. Hammer activity was ceased due to excessive weight applied to the bit.

was reached. Then, **Regime 1** was observed not only within the *optimum state* region but also in the final section of the curve, where the penetration per impact decreased and became inconsistent.

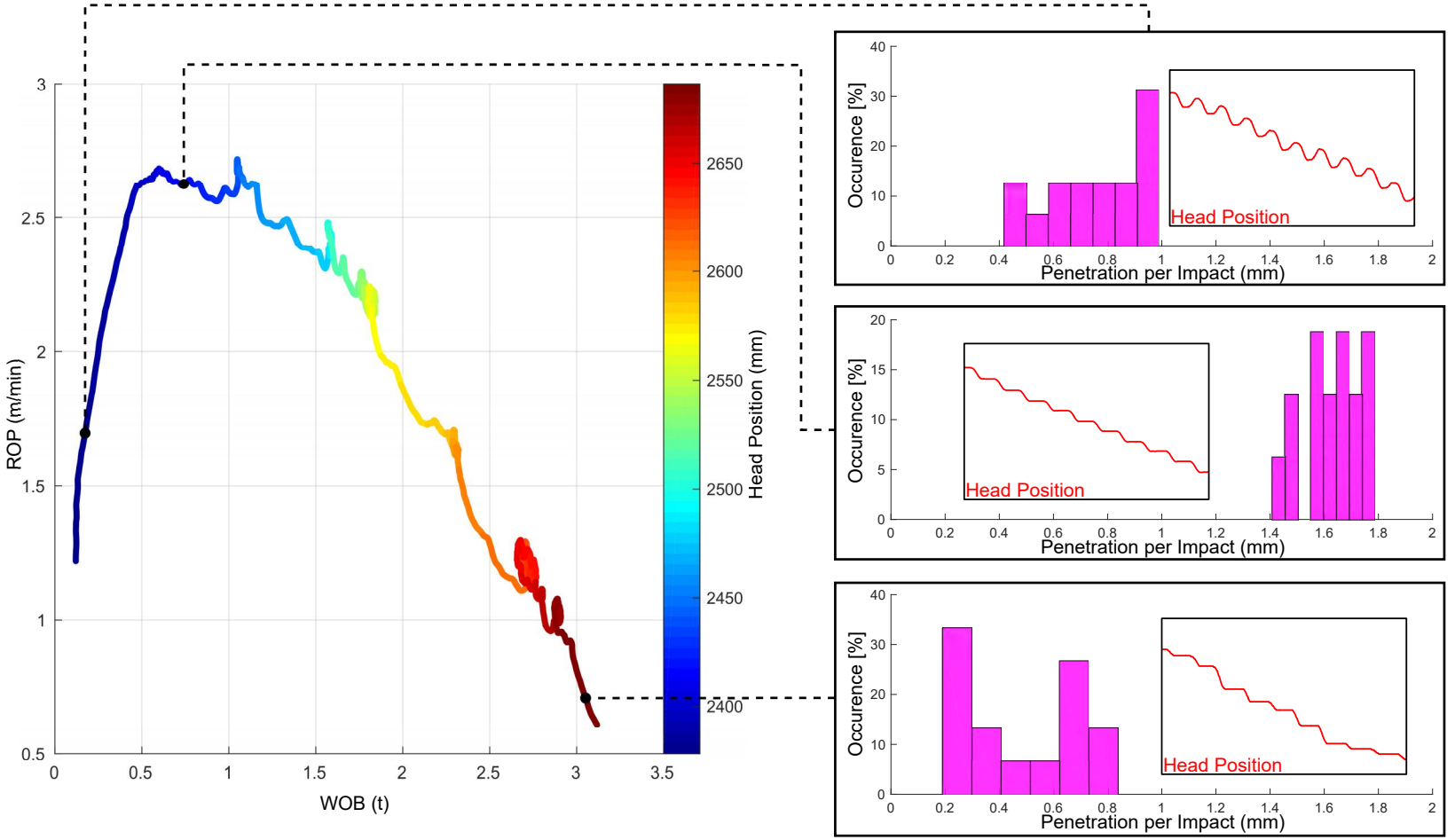

Figure 3.26: Penetration per impact and drilling regimes in different regions of the *ODS* curve. The rotary head position signal could be used as an indication of whether the current applied weight-on-bit is proximate to the optimum one.

3.4 Concluding Remarks

In order to gain a better understanding of the mechanisms associated with down-the-hole percussive drilling, our team visited a mining site and deployed our custom-built monitoring system to collect drilling data:

- A truck-mounted drilling rig was instrumented with high-precision and high-sampling rate sensors installed strategically on its machinery.
- More than 12 GB of data was recorded using three distinct protocols: all data was recorded continuously at 10 Hz, and selected data were recorded for short periods of time at 1 kHz and 20 kHz. The analysis of the data revealed that 1 kHz sampling sufficiently detailed the signature of the hammer dynamics. Therefore, recording data at 20 kHz in future field tests is unnecessary.
- Several algorithms were developed to compute the following parameters: bit depth, hole depth, WOB, TOB, ROP, bit penetration per impact, and piston impact frequency. The algorithms were instrumental in the data processing phase and allowed us to extract distinctive information from the data set.

One of the most outstanding outcomes of the field tests is evidence that every single piston impact (on top of the drill bit) can be identified from measurements of surface equipment. High-precision rotary head position measurements reveal the ability to estimate the rotary head displacement following each piston impact. This result opens up a wide range of opportunities to monitor parameters related to the DTH hammer system, such as piston impact frequency and drill bit penetration per piston impact. Furthermore, it is also possible to estimate the angular displacement of the drill bit between subsequent piston impacts and the piston impact energy in real time. These parameters can be used as input in data-driven optimisation algorithms developed in the future.

Another significant outcome was to find evidence of the existence of *Optimum Drilling States*, which are characterised by an optimum rate of penetration that is achieved for a given rock-bit-hammer configuration and a set of drilling parameters, such as (1) the indexing angle, (2) the piston impact energy, and (3) the weight-on-bit. It is still unclear how each of these parameters individually affects the overall drilling performance.

Moreover, the data analysis further revealed the occurrence of distinct drilling regimes, characterised by different patterns of the rotary head displacement: (i) periodic step-type motion with the rotary head at full rest between impacts, (ii) periodic motion with the bit drilling between impacts, (iii) periodic motion with the rotary head moving upward (vertical rebound) after each piston impact, and (iv) hammer inactive and bit drilling by shearing the rock.

Chapter 4

Discrete Percussive Drilling Experiments

The analysis of the drilling data collected during the field tests revealed evidence of the existence of *Optimum Drilling States* in several instances (refer to Chapter 3). The next stage of this research project is to isolate—from the system dynamics—the effect of the WOB on the average drilling performance. The aim is to investigate in a controlled environment (laboratory) whether the occurrence of the ODS phenomenon is intrinsic to the bit-rock interface or related to the system dynamics. To accomplish this task, our team designed and built a unique laboratory apparatus that can drill shallow holes in rock samples with only discrete events—a single impact at a time—and independently controlling the WOB, the piston impact energy and the indexing angle between subsequent impacts during the experiments. The idea is to mimic precisely the percussive drilling process, but with the hammer system dynamics decoupled from the bit-rock interface.

The main difference between our experimental setup and a full-scale percussive drilling apparatus (or rig) is the fact that the initial conditions are guaranteed to be re-established before the impact of the piston on the drill bit occurs; the desired axial load (weight) will always be appropriately applied to the bit before the arrival of the piston at each percussive cycle during drilling.

This chapter initially presents the equipment, its functionalities, and how it is monitored and controlled. Then, the entire experimental procedure is detailed. A series of experiments were conducted on rock samples considering different drilling parameters, such as piston impact energy, static WOB, and indexing angle between impacts. Finally, the results of the experiments and the conclusion of the chapter are presented.

4.1 Discrete Impact Experiments

In discrete percussive drilling experiments, a shallow hole is drilled (in a rock sample) with one single piston activation at a time. After each impact of the piston on the drill bit, the bit penetration is recorded, and the initial conditions are re-established before the subsequent piston activation occurs. Figure 4.1 illustrates schematically the entire procedure of the discrete percussive experiment:

- **(1)** - Before the experiment starts, a rock sample is fixed in position in front of the drill bit.
- **(2)** - The barrel and drill bit are advanced towards the rock sample, and a constant axial load (weight) is applied to the bit. At this stage, the piston rests on the other end (opposite to the drill bit) inside the barrel at its initial position.
- **(3)** - Then, the piston is accelerated towards the drill bit reaching a specific velocity.
- **(4)** - The piston strikes the drill bit, which results in the drill bit penetrating the rock. The piston impact velocity (immediately before impact) is estimated and the impact energy is computed.
- **(5)** - The motion of the drill bit and barrel are continuously recorded, and their final displacements are calculated.

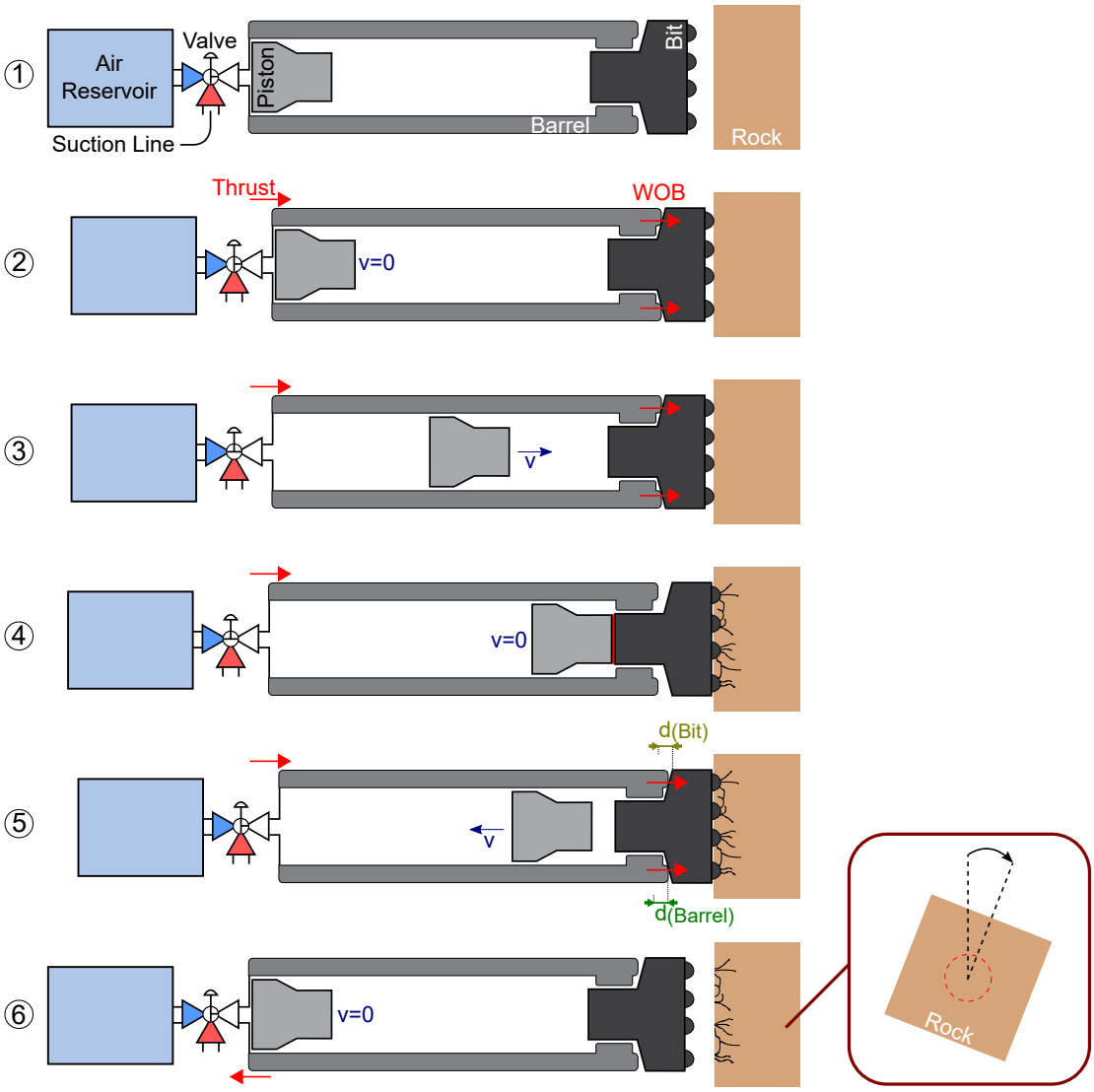

Figure 4.1: Schematic of the discrete percussive drilling experiments.

- **(6)** - Finally, the piston is returned to its initial position, the barrel and drill bit are moved away from the rock (backwards), and the rock sample is rotated. Once the initial conditions are re-established, the process is repeated.

The First Prototype

A prototype was initially built to test and validate the principle of the discrete percussive drilling experiments (refer to Figure 4.2). The experiments carried out with the apparatus were also fundamental for the selection of appropriate actuators and sensors for monitoring the piston velocity and the displacements of the barrel and drill bit.

During the experiments, the maximum piston impact energy achieved was about 20 J (per impact), and it was possible to apply a maximum of 400 kgf of axial load to the drill bit. Moreover, the machine operator was required to perform manually several procedures after each piston activation; for instance, the piston would have to be repositioned in place and the rock sample would have to be rotated[1] before any subsequent activation of the piston. The piston impact frequency achieved during the experiments was about one piston impact every four minutes.

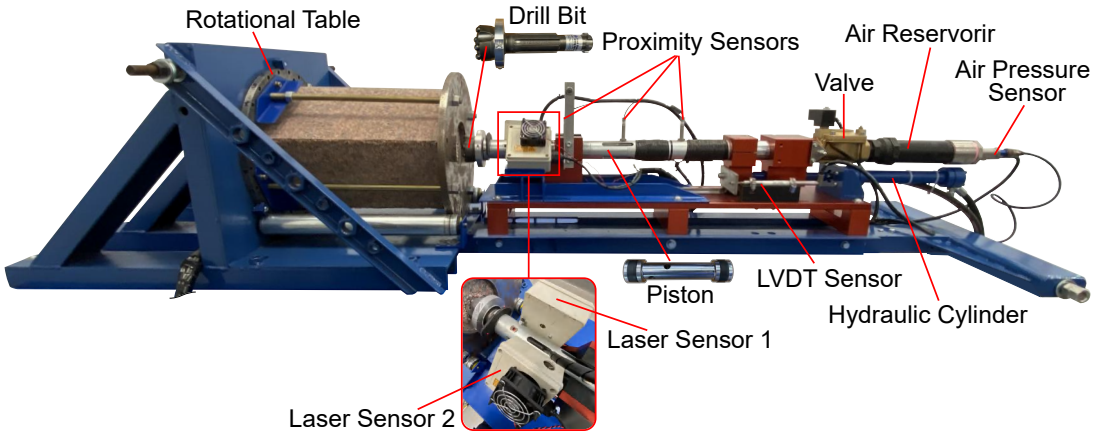

Figure 4.2: The first prototype of the equipment to perform discrete percussive drilling experiments.

[1]The rock sample could be rotated by increment of a multiple of 5 degrees (5°, 10°, 15°, etc.).

Equipment Final Revision

After validating the experiments with the prototype, the equipment *Woody* was designed and built (refer to Figure 4.3).

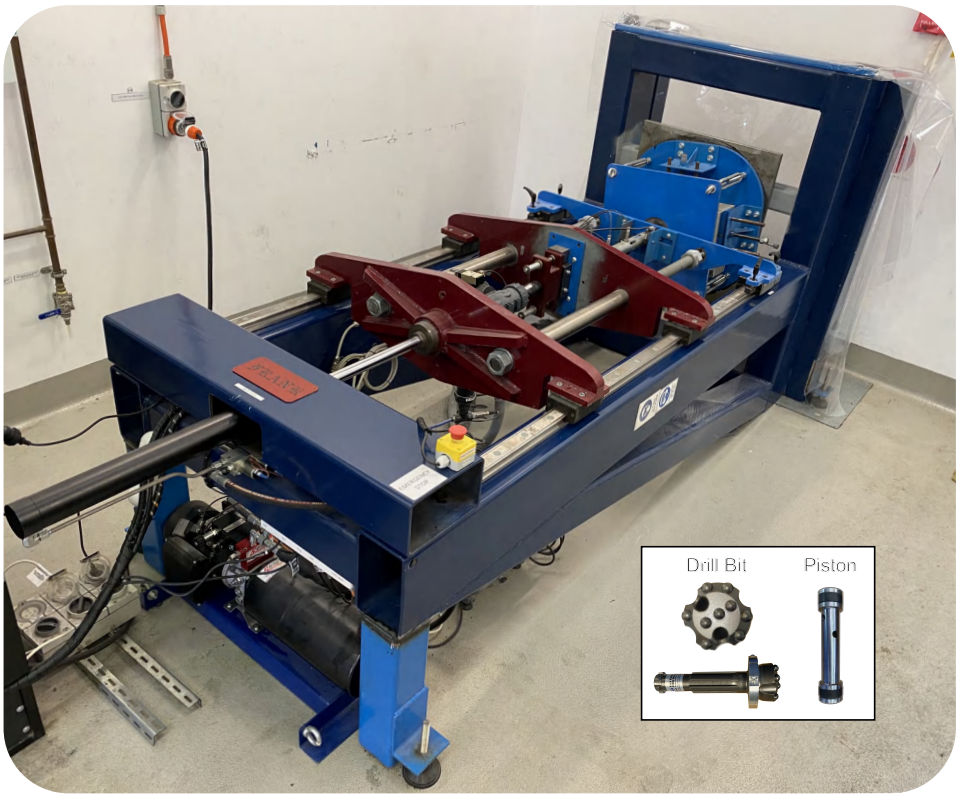

Figure 4.3: Equipment *Woody* built for single impact experiments.

4.2 Experimental Setup: *Woody*

Figure 4.4 shows the complete mechanical structure of the machine as well as the sensors installed on it. Details of the sensors are presented in Table 4.1.

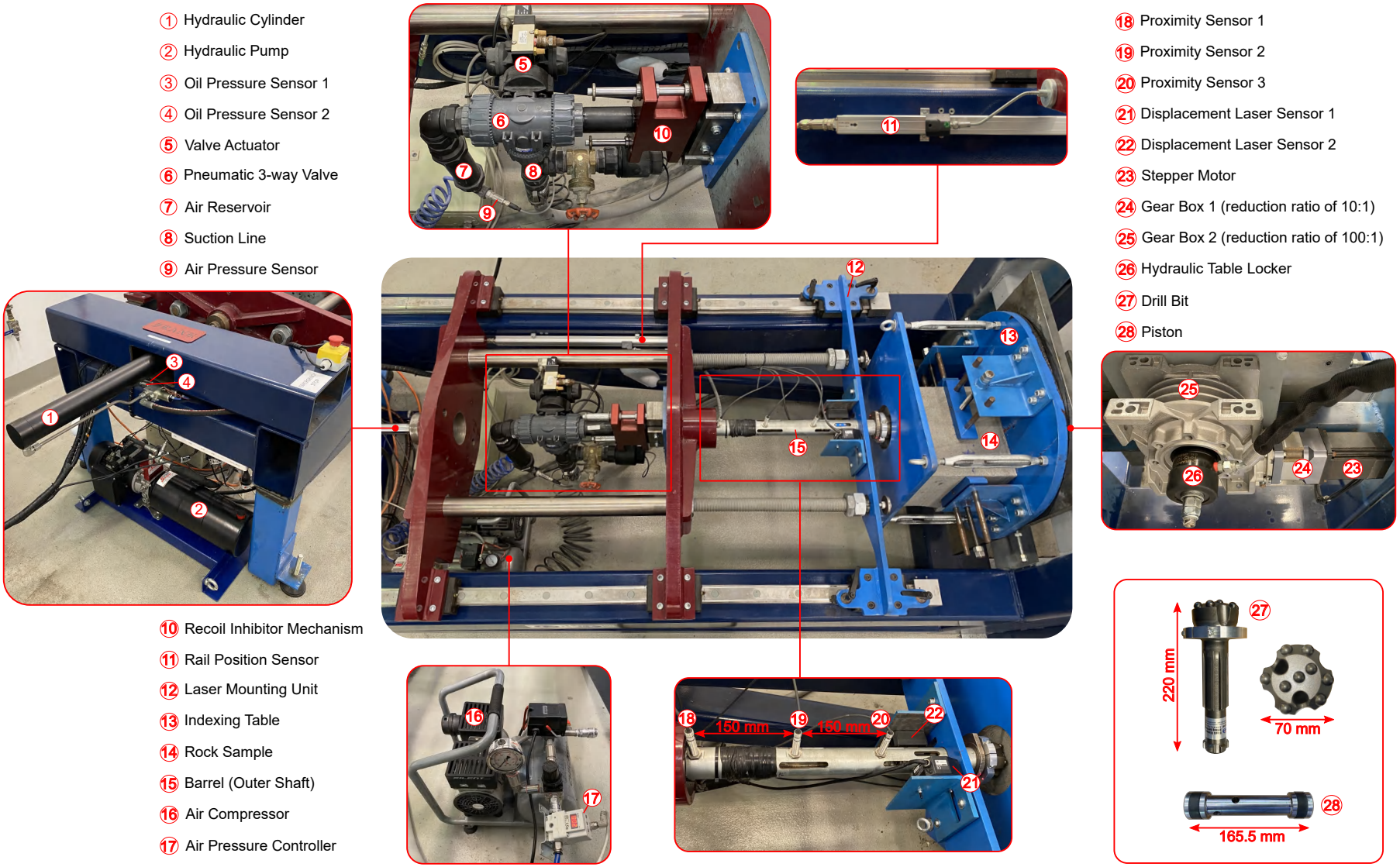

Figure 4.4: Overview picture and close-up pictures of *Woody* and its main components.

ID	Sensor	Unit	Sampling Rate	Precision
3	Oil Pressure 1 (Hold-Back)	Bar	1 kHz	±0.1%
4	Oil Pressure 2 (Feed)	Bar	1 kHz	±0.1%
9	Air Pressure	Bar	1 kHz	±0.1%
11	Rail Position	Millimetres	1 kHz	±0.1%
18	Proximity 1	Volts	50 kHz	±0.1%
19	Proximity 2	Volts	50 kHz	±0.1%
20	Proximity 3	Volts	50 kHz	±0.1%
21	Displacement Laser 1	Millimetres	2.5 MHz	±0.02%
22	Displacement Laser 2	Millimetres	2.5 MHz	±0.02%

Table 4.1: List of sensors installed on the equipment (refer to Figure 4.4).

The equipment *Woody* consists of a cross-head assembly that moves across two parallel rails installed on a heavy-duty frame, as shown in Figure 4.5.

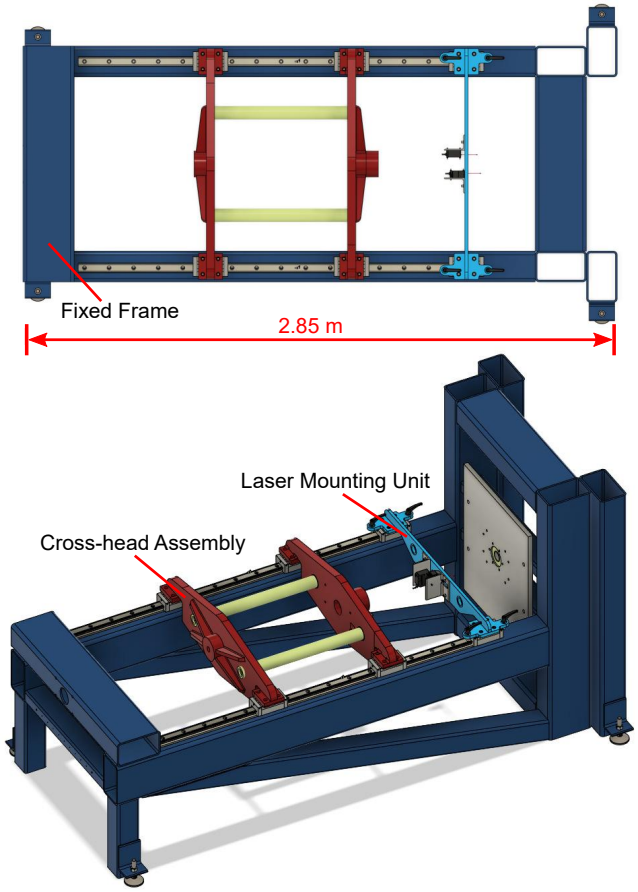

Figure 4.5: Heavy-duty fixed frame and movable parts of the equipment. The *Cross-head Assembly* and the *Laser Mounting Unit* move independently across the rails.

The barrel[2] is fixed on the cross-head assembly and it hosts—at its front section—a percussive drill bit[3]. A high-precision rail position sensor[4] was installed on the fixed frame of the equipment and attached to the cross-head assembly to track precisely the movement of the barrel at all times (refer to Figure 4.4).

Pistons and Impact Velocity

Two different pistons were machined for the discrete percussive drilling experiments; their length and mass are shown in Figure 4.6. Piston 1 (0.8 kg) was initially supposed to be used throughout the entire experimental program. However, due to concerns of material deformation for experiments performed with high impact energy, it was decided to produce Piston 2 (1.382 kg), which is not only heavier but is also made of a material with a higher yield strength; moreover, using Piston 2, it is possible to achieve higher impact energy without accelerating the piston to an extremely high velocity, which is safer for the machine operator and diminishes the possibility of equipment damage.

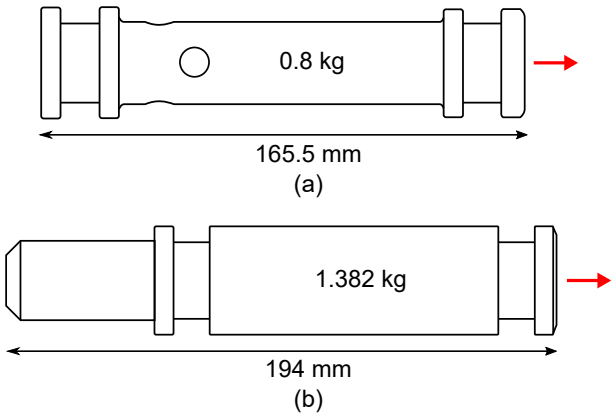

Figure 4.6: Pistons machined for the experiments: (a) Piston 1 made of steel AS1444-4140, and (b) Piston 2 made of steel AS1444-4340.

The selected piston for the experiments travels along the barrel's interior. As shown in Figure 4.7, there are openings (or vents) along the barrel to allow

[2]The barrel has 80 centimetres of length and 42 millimetres of internal diameter.
[3]The 70-millimetre (∅) percussive drill bit has 9 tungsten carbide buttons.
[4]The rail position sensor has a stroke of 70 centimetres.

pressurised air to escape in order to reduce pressure behind the piston after impact; this prevents secondary impact from occurring. The three proximity sensors, mounted along the barrel equidistantly, are used to measure the arrival time of each edge[5] of the piston with a 0.02-millisecond precision, which allows the derivation of the piston velocity before and after impact (refer to Figure 4.8). The impact energy is equal to the kinetic energy of the impacting piston, defined by:

$$E(J) = \frac{mv^2}{2} \tag{4.1}$$

where m is the mass of the piston.

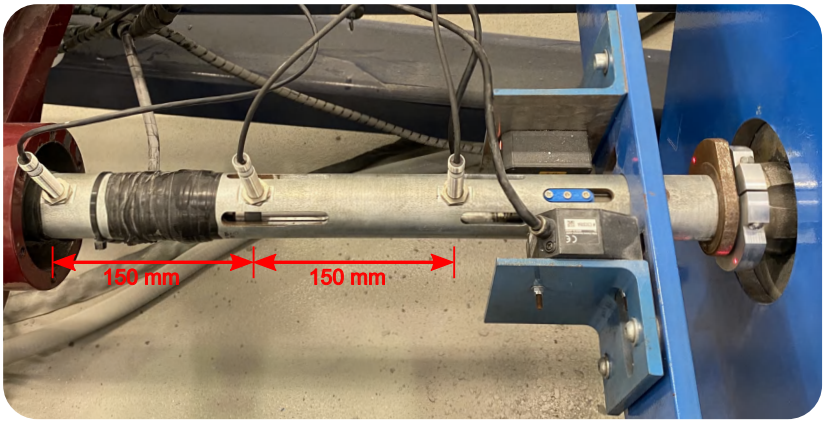

Figure 4.7: Barrel equipped with three proximity sensors used to estimate the piston velocity. The *Laser Mounting Unit* holds two laser sensors pointed to the collars of the drill bit and barrel, used to capture precisely their displacements throughout the experiments.

Furthermore, *Woody* has three main sub-systems: (1) the pneumatic system, (2) the hydraulic system, and (3) the indexing system.

4.2.1 Hydraulic System

A hydraulic pump—with a 1.1 kW single phase motor and equipped with a flow throttling valve with a maximum flow capacity of 25 l/min—is connected to a

[5]Due to the difference in the shape of Piston 1 and Piston 2, the machine operator needs to specify in the software which piston was selected prior to the beginning of the experiments.

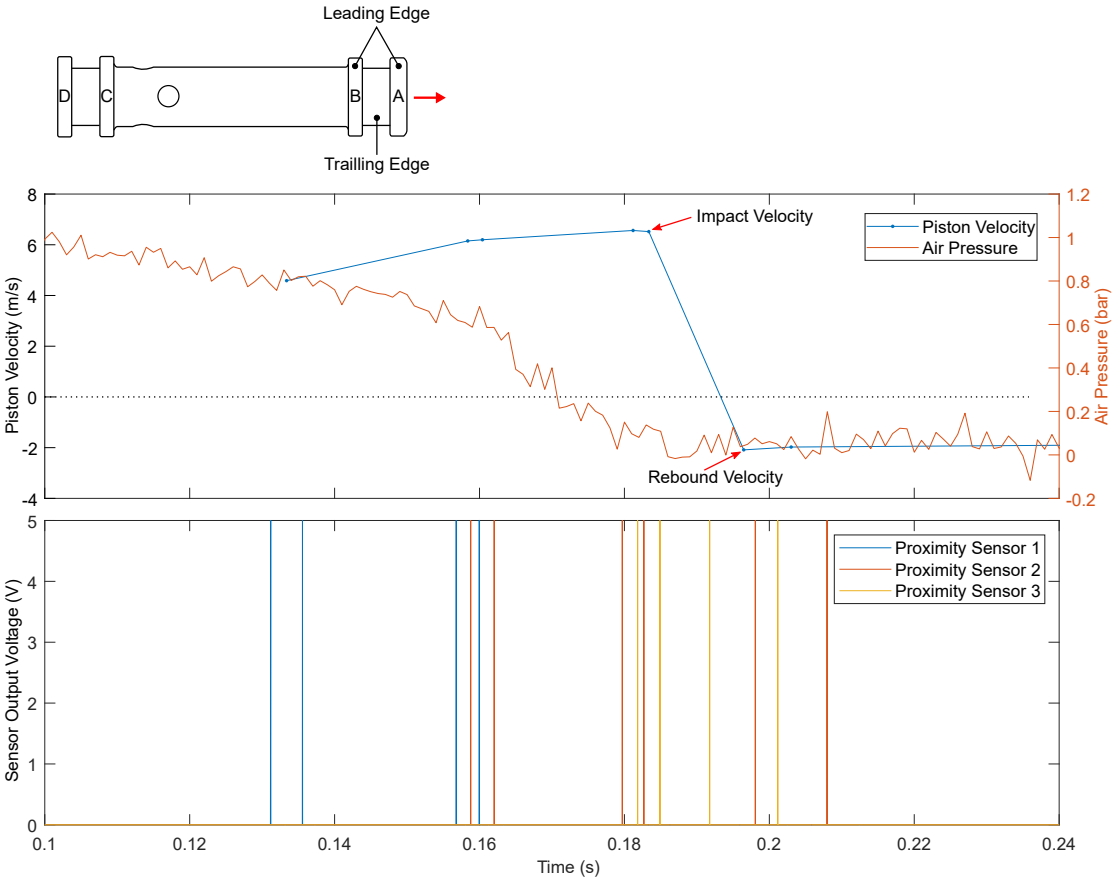

Figure 4.8: The piston velocity is estimated when the piston's edges pass through the proximity sensors installed along the barrel.

hydraulic cylinder with 600 millimetres of stroke. The cylinder is attached to the cross-head assembly, moves with a maximum velocity of 2 cm/s, and can also apply a maximum axial load of 10791 N (1.1 tonf) to the drill bit. Moreover, two IFM electronic pressure sensors measure the hold-back and feed pressures in the front and rear chambers of the hydraulic cylinder.

4.2.2 Pneumatic System

The main component of the pneumatic system is a PVC T-port 3-way ball valve equipped with an electronic actuator (refer to Figure 4.9). The functionality of such a valve is to control whether the interior of the barrel is exposed to the suction line (*suction mode*) or to the pressurised air line (*propulsion mode*). In

suction mode the piston is held at the initial position (opposite to the drill bit) prior to each single impact experiment. At the start of the experiment, the valve is rapidly switched to *propulsion mode* and the pressurised air—stored in a reservoir—is released, which in turn accelerates the piston inside the barrel. Then, the valve is switched back to *suction mode* in order to return the piston to its initial position, avoiding the occurrence of secondary impact. Note that the time duration in which the valve remains in the *propulsion mode* is controlled by software and must be configured prior to any test series.

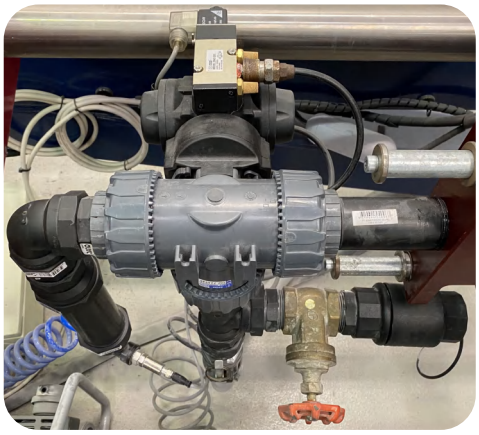

Figure 4.9: PVC T-port 3-way ball valve.

The PVC 3-way ball valve is connected to the lower end of a recoil inhibitor mechanism, which is the mechanical linkage between the valve output and the barrel. Figure 4.10 shows the recoil inhibitor mechanism, which isolates the barrel from the recoil force generated from the release of pressurised air. When an excessive force is generated during a percussive activation, the recoil inhibitor opens, as shown in Figure 4.10 (b).

In the pressurised air line, a compact 4-litre air compressor, with a maximum flow rate of 30 l/min (1.06 CFM at 8.3 bar), discharges air inside a 2-litre reservoir. An electro-pneumatic regulator (controlled by software) maintains the desired pressure inside the reservoir, which can be adjusted from 0 to 7 bar. Furthermore, the pressure inside the reservoir is monitored by an IFM electronic pressure sensor.

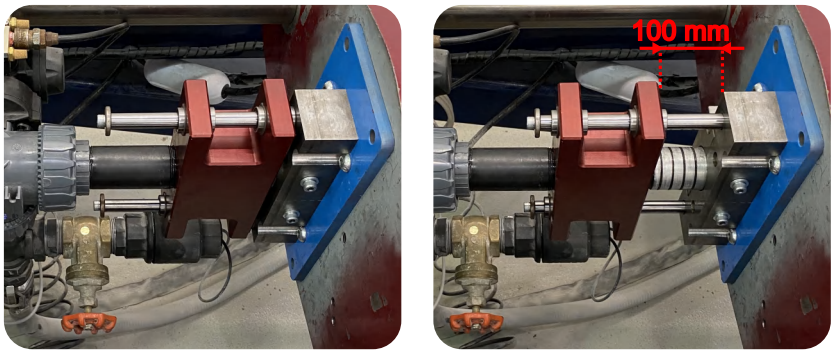

Figure 4.10: Recoil Inhibitor Mechanism: (a) closed and (b) open.

4.2.3 Indexing System

The indexing system consists of a rotational table, a closed-loop stepper motor and two gearboxes installed in series (refer to Figure 4.4). The shaft of the stepper motor turns 1.8° with a maximum torque of 8.25 N.m. The two gearboxes installed in series, between the motor and the table, give a reduction ratio of 1000:1, meaning that the output angular displacement (of the table) is 0.0018° with a maximum torque of 8250 N.m and with ±1% of precision.

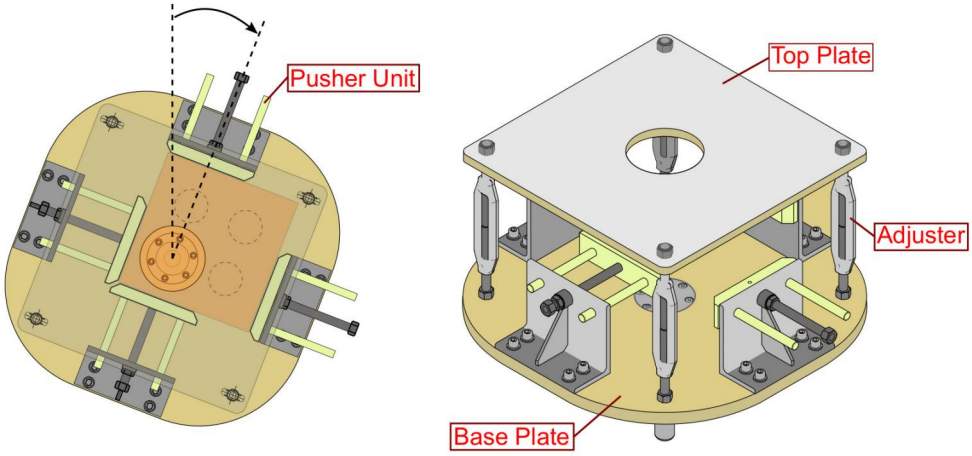

Figure 4.11: Rotational table.

As shown in Figure 4.11, the rotational table is composed of a base plate, a top plate, four height adjusters and four pusher units. Once the rock sample is positioned adequately between the base and top plates, the machine operator can

readjust the pusher units to move the rock; it is possible to drill four distinct holes on the same rock face by readjusting the pusher units correctly. Considerable effort was made to perfectly align the centre of the table with the drill bit axis during the commissioning phase. This ensures that the borehole is propagated with a succession of discrete impacts.

4.3 Data Acquisition and Control System

Figure 4.12 shows the *National Instruments* data acquisition modules, the stepper motor driver, and the electronics circuits, which are necessary for reading and recording the signals from the sensors as well as for controlling the actuators and valves. The PXIe-1073 is used to monitor the high-speed laser sensors and also 24-volt output signals. The PXIe-1073 provides an electrical interface to the pneumatic and hydraulic sub-systems. The cDAQ-9185 is used to monitor all slow-speed sensors (rail position, pressure and proximity sensors) and also to communicate with the stepper motor driver to operate the rotational table.

A dedicated LabVIEW real-time engine software application was developed (refer to Figure 4.13), which allows the machine operator to control the equipment, monitor the statuses of all its sensors, and communicate with the data acquisition modules. Additionally, several parameters can be configured on the software application: (1) the desired weight-on-bit, (2) the angular displacement of the table (between impacts), (3) the initial air pressure inside the reservoir (to control the piston velocity and impact energy), and (4) the period of time in which the 3-way ball valve remains opened (to avoid secondary impact).

Figure 4.12: Data acquisition modules and electronics: (a) PXIe-1073 and I/O modules, (b) cDAQ-9185 and electronics circuit, and the (c) stepper motor driver and electronics.

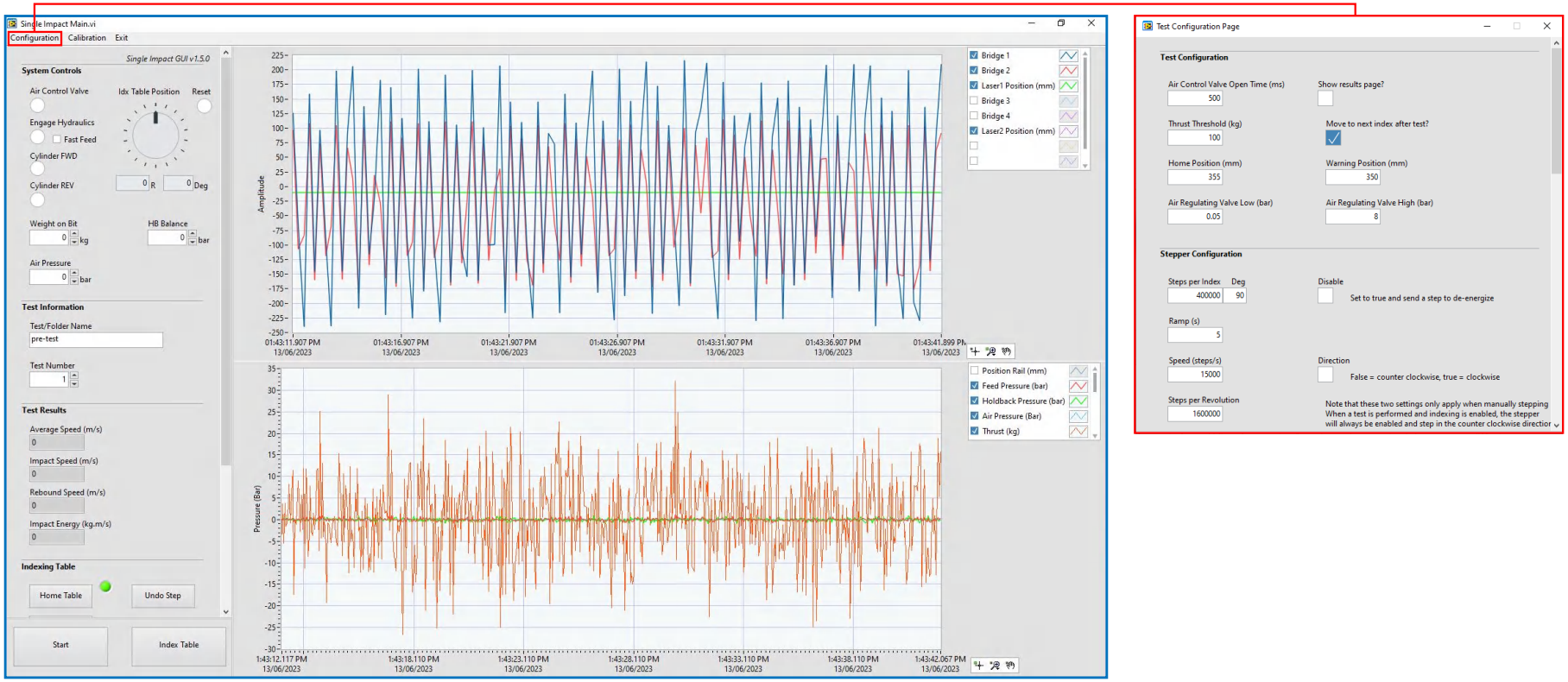

Figure 4.13: Graphical User Interface (GUI) developed in LabVIEW (LabVIEW, 2023).

4.4 Experimental Procedure

The diagram shown in Figure 4.14 depicts the discrete percussive drilling experiment process and can be explained as follows:

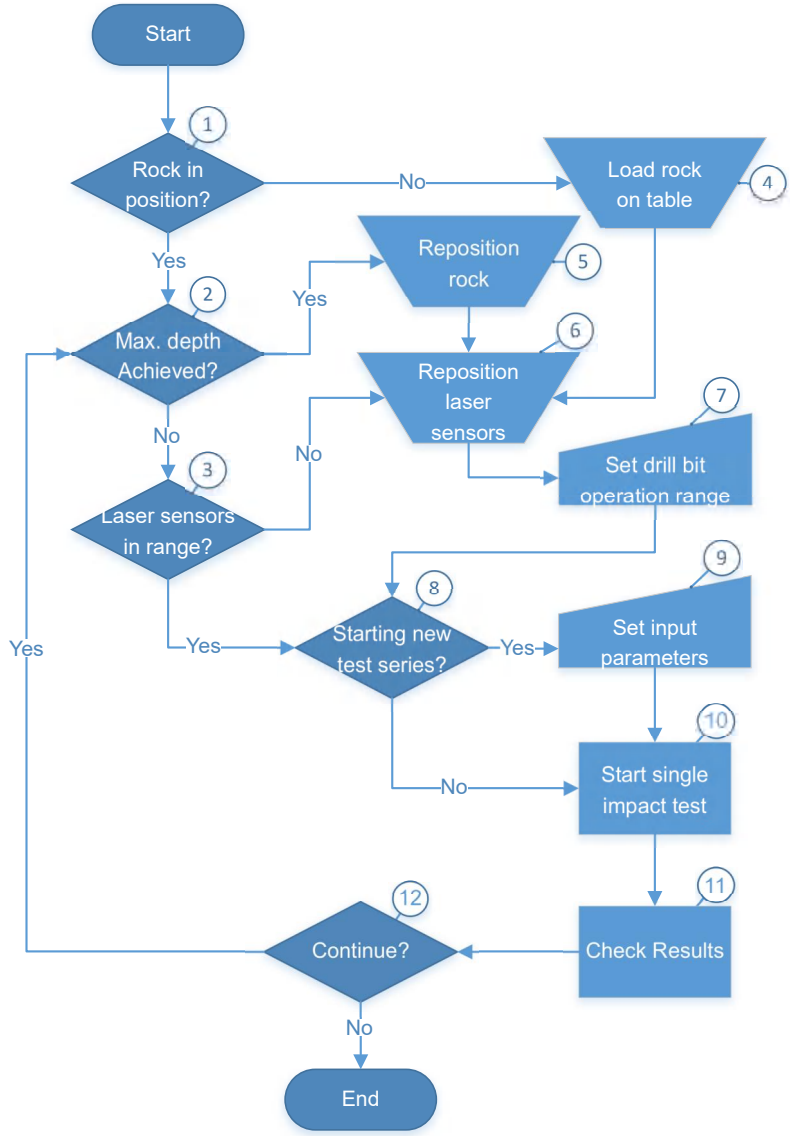

Figure 4.14: Experimental procedure flow chart.

- **(1)**: Before the test series starts, the rotational table must be inspected and the rock sample must be correctly fixed on it.
- **(2)**: The operator must check whether the rock sample is pre-drilled or not. In case the rock is already pre-drilled, the depth of the hole must

be checked. The operator can simply use a measuring tape or advance the barrel until the drill bit touches the rock sample; then, he can check the rail position sensor signal to estimate the hole depth. It is important to emphasise that the maximum hole depth is approximately 4.5 centimetres—before the drill bit's collar touches the rock—meaning that if the hole depth is approaching the maximum allowed depth, the software interface warns the operator to start a new hole.

– **(3)**: The laser sensors must be positioned from 7 to 8 centimetres from the measurement target. Due to their operating range of only 1 centimetre, the operator must always monitor whether the laser sensors have become out of range before any single impact test.

– **(4)**: For safety reasons, the operator must have appropriate training to be able to load the rock onto the rotational table; otherwise, assistance from trained personnel is required. Additionally, due to the weight of the rock sample such a task is only possible with the assistance of adequate equipment, such as a forklift or a gantry system. Initially, considering the table is in an appropriate position, either the top plate should be removed or only one of the pusher units (in this case the rock can be slid from the side or top); the pusher units should also be readjusted in order to make enough space to load the rock sample on the table (refer to Figure 4.11). Once the rock is correctly placed on the base plate, the pusher units and the top plate should be readjusted until the rock sample is in the correct position and adequately fixed on the table.

– **(5)**: The dimensions of the rock samples used for the experiments are 300x300x300 mm^3, and it is possible to drill four holes on each rock face. In order to adjust the rock's position on the table, the top plate should be loosened first, and then the operator can readjust the pusher units to reposition the rock. After that, the top plate should

be adequately tightened before the rotational table can move.

- **(6)**: Whenever the rock sample is repositioned on the table or the laser sensors become out of the operating range, the laser mounting unit must be moved to the correct position (refer to Figure 4.4). First, the machine operator must advance the barrel until the drill bit touches the rock face. Next, the laser mounting unit must be moved until the laser sensors are within the operating range; then, it must be fixed firmly on the heavy-duty frame.
- **(7)**: The drill bit operating range must be set in the software whenever the laser mounting unit is moved to a different position. It ensures that the barrel is always automatically moved to a safe position after each single impact test; this is necessary because the rotational table can only move if the drill bit is not in contact with the rock (for safety reasons). In order to define the bit operating range, the operator must move the barrel slowly until the drill bit is away from the rock face and the end of the barrel is at a safe distance away from the laser mounting unit. Then, the current position, acquired from the rail position sensor, is saved on the software configuration window.
- **(8)**: The operator must decide whether a new test series needs to be initiated or not. It is recommended to readjust the laser mounting unit if a new test series is initiated.
- **(9)**: In case a new test series is initiated, the operator must define and save several input parameters on the software (refer to 4.13): thrust force, indexing angle between impacts, the air pressure to control the piston velocity, and the time interval that the 3-way ball valve will remain open. Furthermore, the location where the data will be saved must also be defined.
- **(10)**: Once the rock is in position and the test parameters are defined and saved on the software, the operator can initiate the single impact

test by simply pressing *Start* on the software interface.

The following set of actions will take place: (i) The hydraulic cylinder will push the cross-head assembly in order to apply a specific weight to the drill bit. From the moment that the PID controller stabilises the WOB according to the desired value set by the operator (± 5 kgf), (ii) the data acquisition system starts to record on memory the data and the 3-way ball valve is activated to release (from the reservoir) the pressurised air in order to accelerate the piston inside the barrel. (iii) Then, the piston strikes the drill bit and is immediately returned to its initial position; the drill bit penetration and barrel displacement are also recorded. The period of time over which the 3-way valve switches back from the *propulsion mode* to the *suction mode* needs to be carefully configured in order to avoid any secondary impact of the piston on the drill bit. The entire data recording process has a duration of 2 seconds, and the computer retrieves the recorded data from the memory of the data acquisition devices and stores it in a TDMS file. Meanwhile, the rotational table is activated and the rock sample is rotated according to the desired indexing angle configured on the software.

- **(11)**: A script written in MATLAB is used to open and interpret the TDMS files.
- **(12)**: Finally, the operator decides whether the test series continues or not, based on the results checked on MATLAB.

4.5 Test Series and Results

This section presents the outcome of an extensive discrete percussive drilling experimental program that was carried out on Blue Stone Granite rock samples (300x300x300 mm^3). Throughout the tests, the borehole was properly cleaned (by the operator) with a brush; unless otherwise stated, the cleaning protocol was to brush the borehole surface always after two successive piston activations.

Prior to Testing Phase

It is important to emphasise that whenever a new hole was started during the experimental program, a *Collaring Phase* was necessary to ensure that the drill bit was engaged with the rock sample. Figure 4.15 shows the recorded displacements of the drill bit and barrel, and also the data from the rail position sensor, pertaining to an entire *Collaring Phase*. Note that the slope of the curve starts to stabilise after several impacts, indicating that the drill bit is fully engaged with the rock sample.

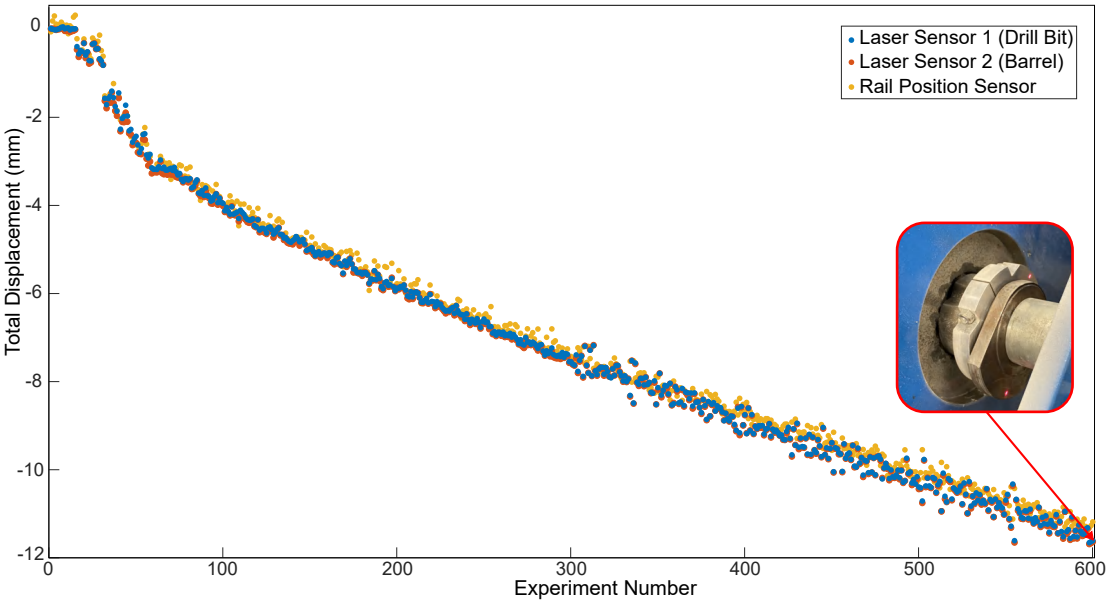

Figure 4.15: Recorded data from a *Collaring Phase*. The slope of the curve stabilises once the drill bit is fully engaged with the rock sample.

During Testing Phase

Once the drill bit is fully engaged with the rock sample, the *Testing Phase* can be initiated. The following parameters are estimated throughout the experimental program:

- The maximum drill bit penetration (P) after each piston impact, which is extracted from the output signal of laser sensor 1 at each experiment, as shown in Figure 4.16.

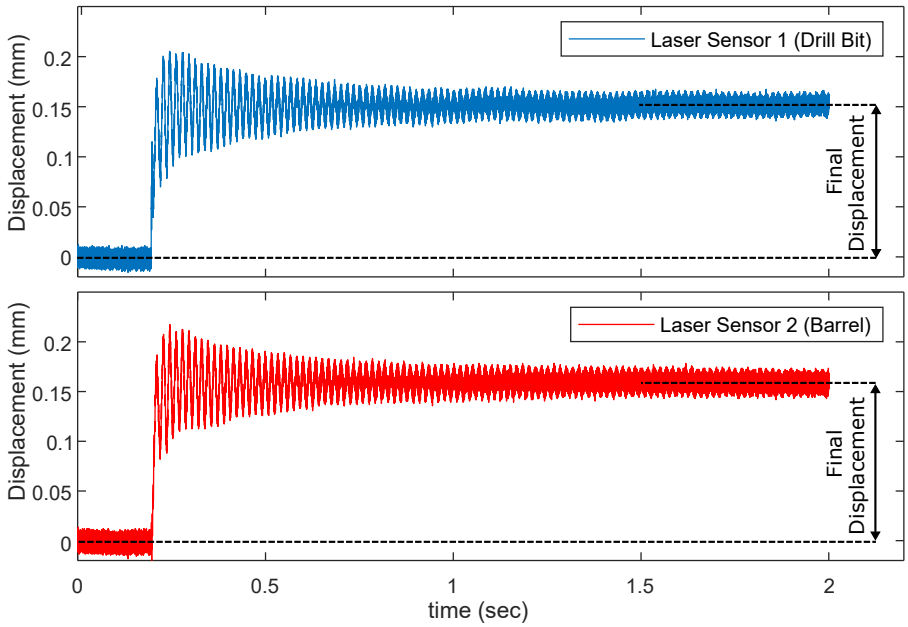

Figure 4.16: Final displacements of the drill bit and barrel after a single piston activation.

- The recovery time t_a, which is the time it takes for the barrel to re-establish contact with the drill bit after impact (refer to Figure 4.17).

- The rate of propagation (ROP) of the borehole, which is computed as an average rate of penetration under constant thrust and impact energy, where the average is performed over as many events required to propagate the rock surface by a given increment. The rationale is to reduce dispersion in the data caused by the details of the geometry of the bit-rock interface. Figure

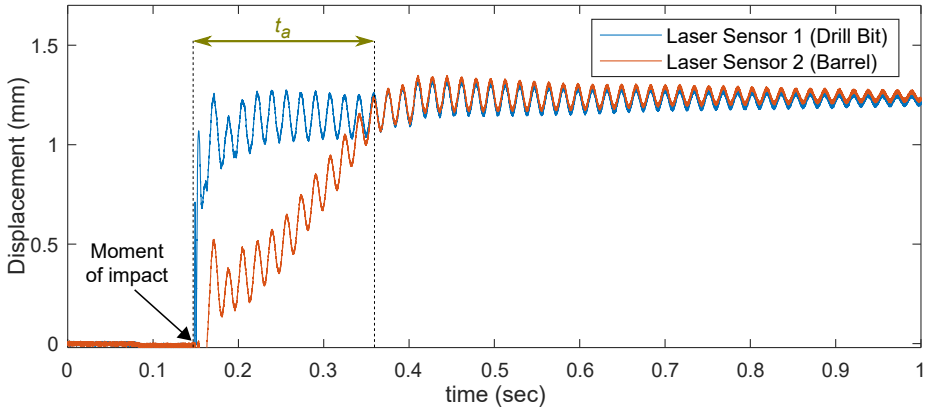

Figure 4.17: The recovery time (t_a) is estimated from the moment of impact until the barrel re-establishes contact with the drill bit.

4.18 illustrates the computation of the ROP from the initial position of the drill bit during several experiments.

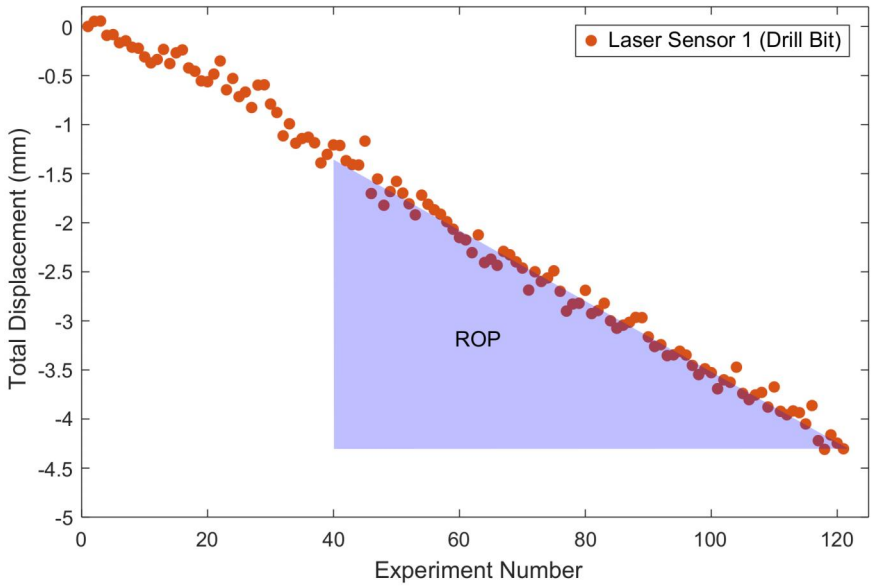

Figure 4.18: Each point in this graph represents the initial position of the drill bit during an impact test, considering the same parameters: piston impact energy, indexing angle, and WOB. Then, several points are considered for the estimation of the ROP (normally representing several complete drill bit revolutions).

Figure 4.19 helps to illustrate the difference between the average rate of propagation (ROP) of the borehole and the maximum drill bit penetration (P) for a single piston activation. Considering that several drill bit penetrations are

necessary for the borehole to be propagated, the following term is introduced:

$$N \equiv \frac{P}{ROP} \tag{4.2}$$

where N can be interpreted as the number of impacts necessary to clear the borehole surface for a given angular displacement between impacts.

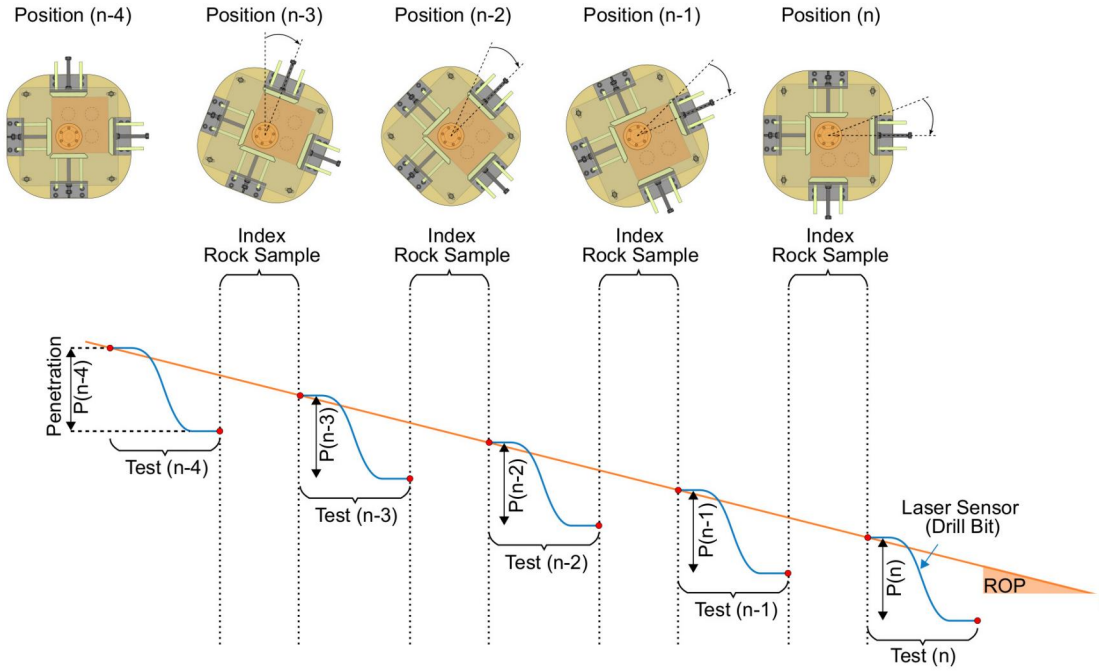

Figure 4.19: Illustration of the ROP estimation from the initial position of the drill bit at each experiment. The angular displacement of the rock sample (between successive impacts) is necessary for the borehole to be propagated throughout the experiments.

4.5.1 Influence of WOB on Drilling Performance

The aim of the experiments explained in this section was to study the dependence of the *ROP* on the axial load applied to the drill bit (WOB). Table 4.2 summarises the drilling parameters considered throughout all test series. Although the indexing angle remained unchanged for all tests, four different piston impact energies were considered—14, 33, 70, and 110 J. Seven distinct tests were carried out for each respective impact energy, in which the WOB varied from 100 kgf up to 700 kgf. Moreover, 121 piston activations were performed for each test.

Test Series	Piston Selected	Impact Energy (J)	WOB (kgf)	Indexing Angle (°)	Number of Impacts (per test)
A	Piston 1	14	#	24	121
B	Piston 1	33	#	24	121
C	Piston 2	70	#	24	121
D	Piston 2	110	#	24	121

- Each test series consists of 7 different tests, each of them carried out for a different value of WOB: 100, 200, 300, 400, 500, 600, and 700 kgf.

Table 4.2: Summary of the test series carried out to investigate the influence of WOB on the drilling performance.

Figure 4.20 shows how the piston impact velocity—and consequently the impact energy—was maintained throughout all test series; the error bars represent the standard deviation of the data (of each test). The piston velocity was kept consistent during the tests for low and medium impact energy (up to 70 J). An impact frequency of three impacts per minute was achieved (not accounting for the time to clean the borehole). However, for high impact energy (110J), the compressor struggled to repressurise the air reservoir rapidly after each piston activation. As a result, the maximum impact frequency achieved was one impact per minute. Furthermore, the piston velocity values were more dispersed (from the mean value) compared to the other tests, as shown in Figure 4.20; a higher piston velocity increases the friction inside the barrel between these two components.

To estimate the *ROP* for each test, the last 90 successive piston impacts were

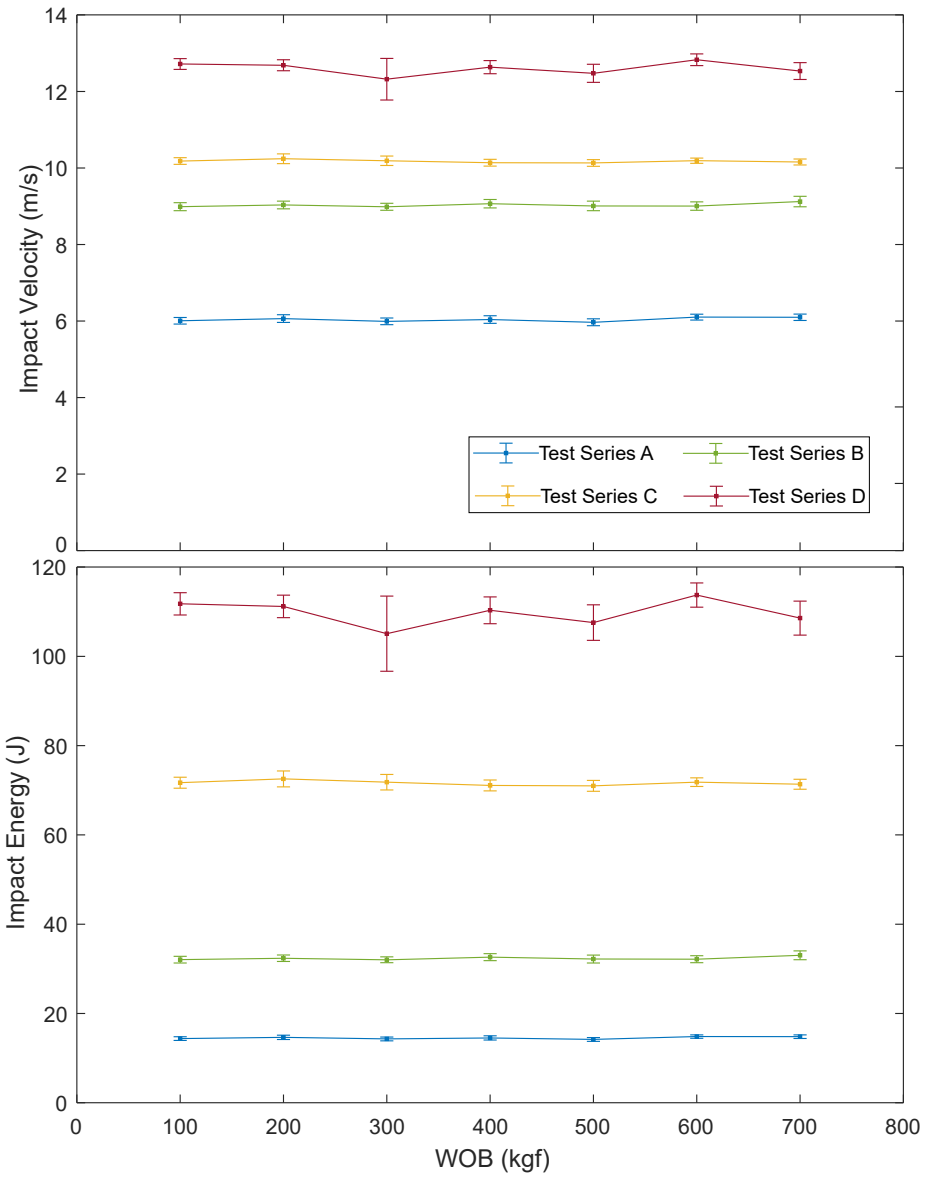

Figure 4.20: Piston impact velocity and impact energy for all test series described in Table 4.2 (impact energy=14, 33, 70, and 110 J, indexing angle=24°, WOB=from 100 kgf up to 700 kgf).

considered; this comprises six complete drill bit revolutions for the indexing angle of 24°. As an example, Figure 4.21 shows the data pertaining to the experiments of the *Test Series D* (impact energy of 110 J). Even though the piston velocity was slightly less consistent compared to the other test series, the average *ROP* did not present any significant change.

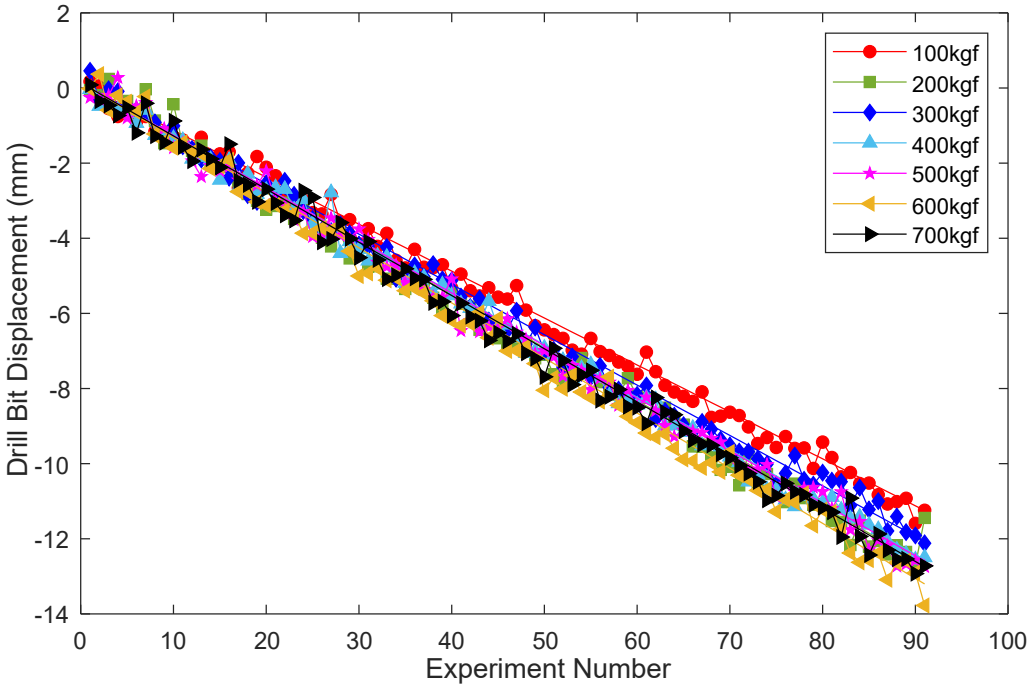

Figure 4.21: Data from the last 90 experiments pertaining to *Test Series D* (impact energy=110 J, indexing angle=24°, WOB=from 100 kgf up to 700 kgf). Each data point corresponds to the initial position of the drill bit at each experiment.

Figure 4.22 presents the rate of propagation (ROP) and the drill bit penetration per piston impact (P) for *Test Series D*. While the WOB changed from 100 kgf up to 700 kgf, no significant change was observed on both output parameters. The ROP varied only approximately 16% from the experiments at WOB of 100 kgf (lowest value) to the experiments at WOB of 600 kgf (maximum value); this small variation could be attributed to the inconsistent impact energy or even different rock samples. Nonetheless, the change in WOB did not influence the overall drilling performance. Moreover, the average penetration P also presented consistent values throughout the tests. Note the high dispersion of the data,

probably due to the heterogeneity of the rock sample; the propagation of cracks and removal of rock material are both uncertain after each impact (refer to Figure 4.22).

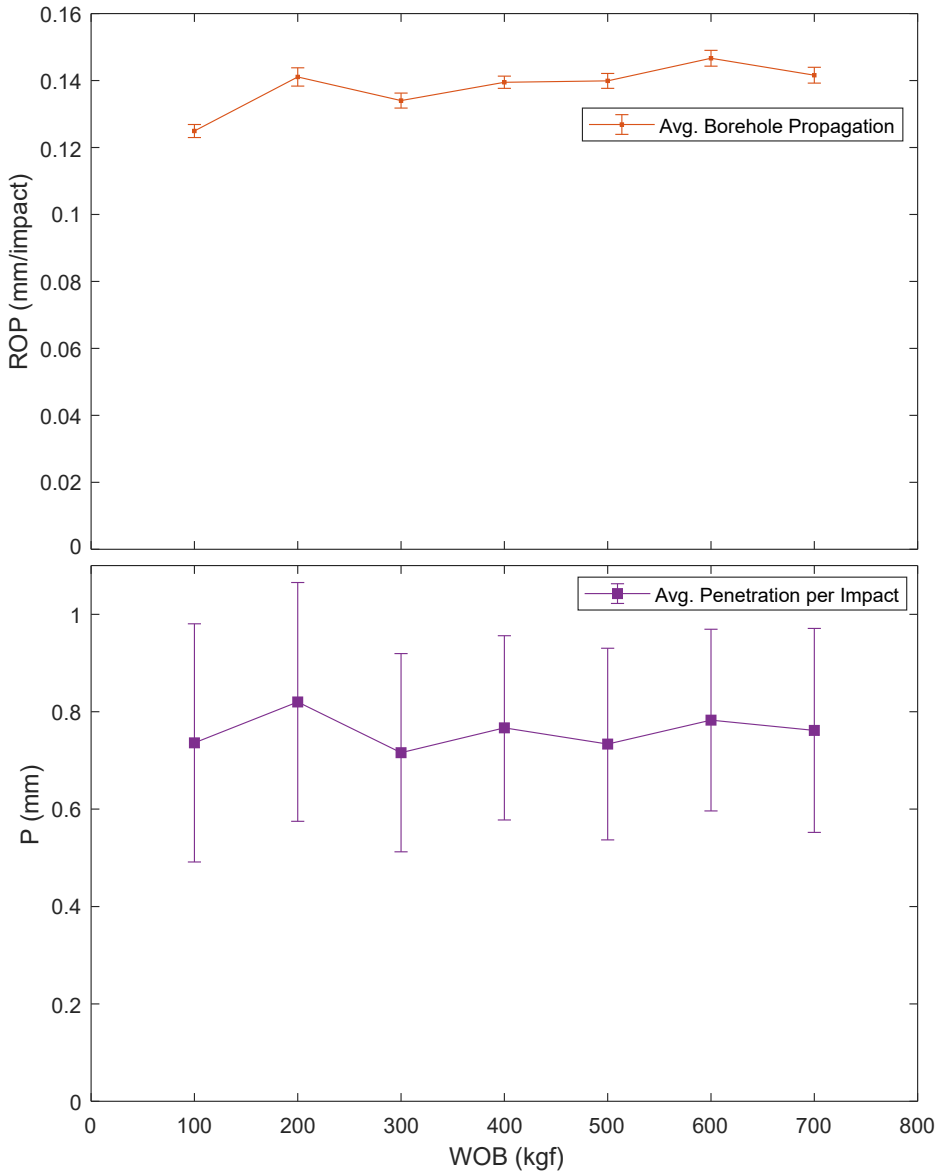

Figure 4.22: Average ROP and average penetration per impact P for *Test Series D* (impact energy=110 J, indexing angle=24°, WOB=from 100 kgf up to 700 kgf) (refer to Figure 4.21).

Comparison of Results

Figures 4.23 and 4.24 show the results pertaining to all test series conducted to evaluate the effect of WOB on the drilling performance. Both parameters ROP and P are presented for each WOB and piston impact energy considered during the experiments. As one can observe, the overall drilling performance did not present any significant change with the increase of WOB. Conversely, the piston impact energy directly affected the average ROP and the average P (refer to Figure 4.24). For low to medium impact energy (up to 70 J), the average ROP and P had a significant change, whereas for medium to high impact energy (70 J to 110 J), both performance parameters changed but with less significance. The increase in drilling performance appears to become less significant once the piston impact energy increases excessively.

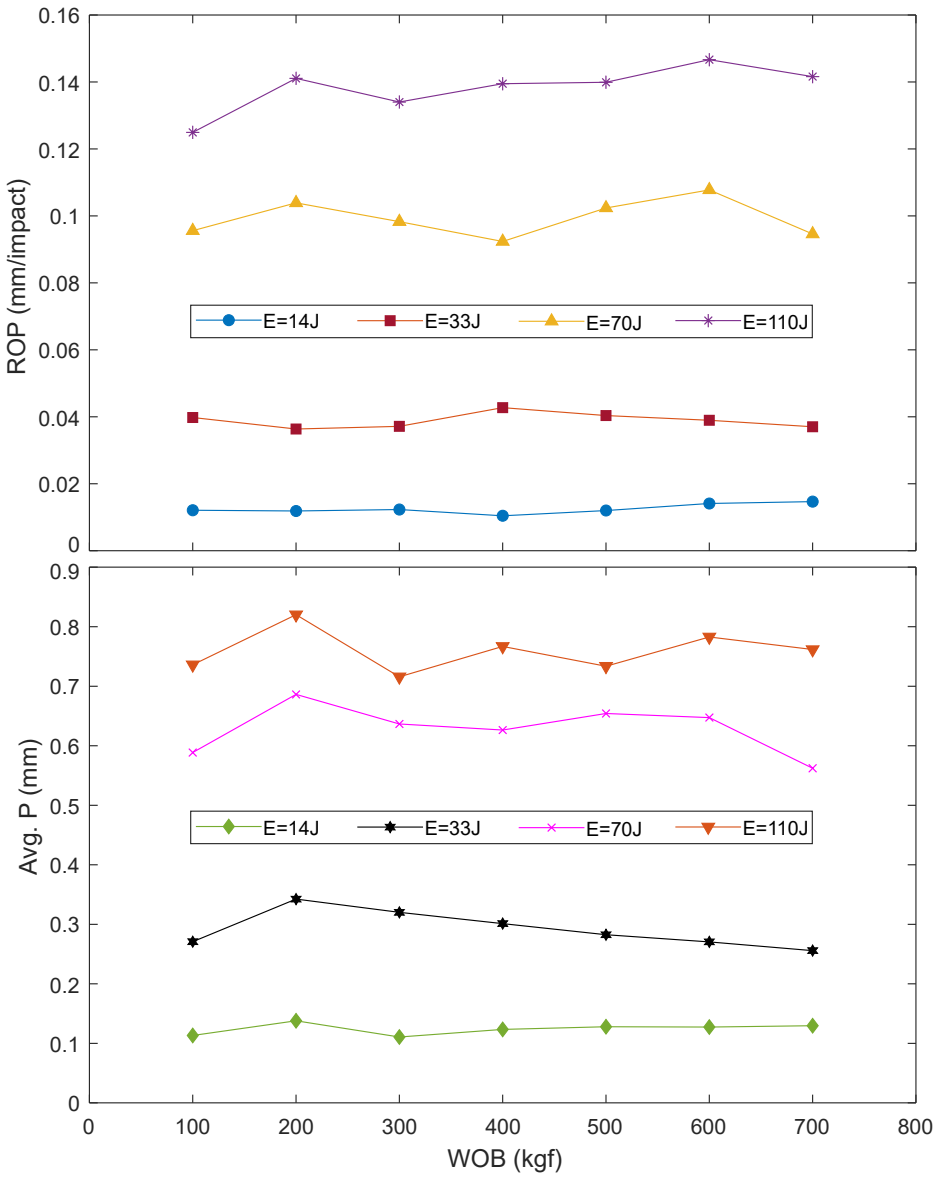

Figure 4.23: Results from all test series described in Table 4.2 (impact energy=14, 33, 70, and 110 J, indexing angle=24°, WOB=from 100 kgf up to 700 kgf). Average ROP and P acquired during the experiments as a function of WOB.

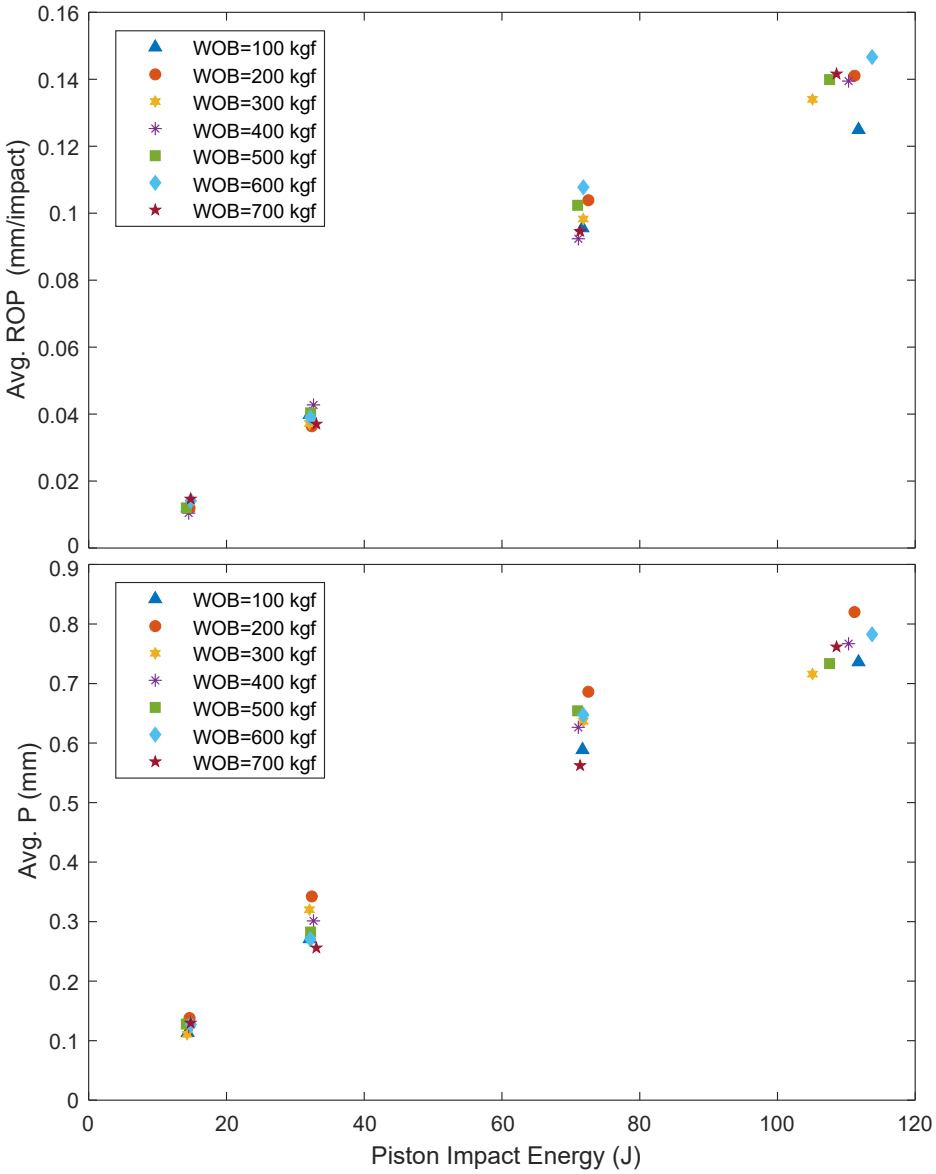

Figure 4.24: Results from all test series described in Table 4.2 (impact energy=14, 33, 70, and 110 J, indexing angle=24°, WOB=from 100 kgf up to 700 kgf). Average ROP and P acquired during the experiments as a function of piston impact energy.

Although the WOB does not affect the average ROP and the average P, this parameter directly influences the time that takes for the barrel to re-establish contact with the drill bit after each impact, as shown in Figure 4.25. Note that the recovery time (t_a) increases considerably for low WOB, considering the tests conducted with high impact energy (70 J and 110 J). It is clear that in an actual drilling process, there exists a minimum WOB that ensures the reconnection of the outer shaft with the drill bit before the subsequent impact occurs.

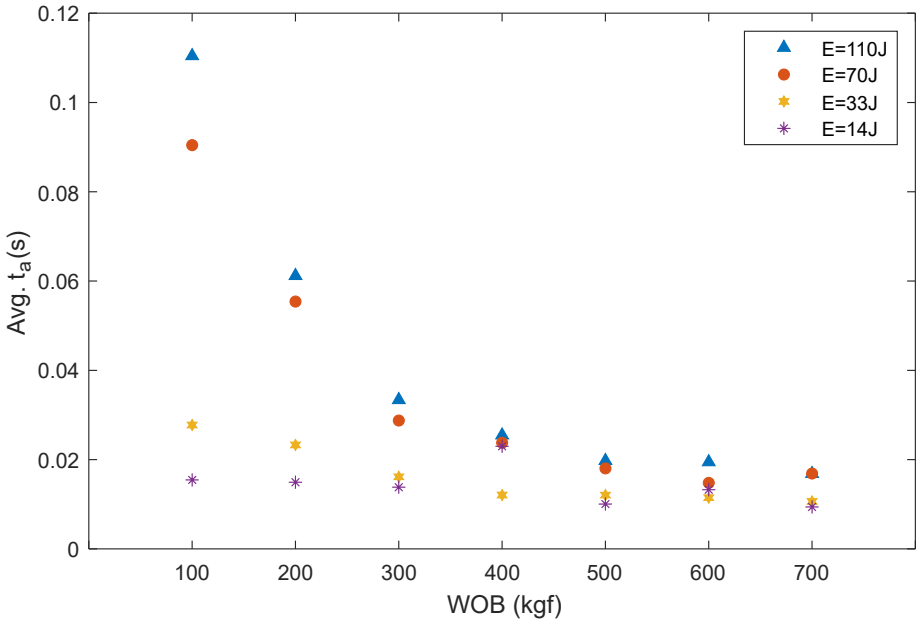

Figure 4.25: Average recovery time (t_a) as a function of WOB for all test series described in Table 4.2 (impact energy=14, 33, 70, and 110 J, indexing angle=24°, WOB=from 100 kgf up to 700 kgf).

Furthermore, a backward movement of the barrel was also observed for low WOB values after each impact. As shown in Figure 4.26, the laser sensor used to monitor the barrel's movement captured a rebound-type movement when low weight was applied to the bit; this behaviour becomes more prominent for high piston impact energy.

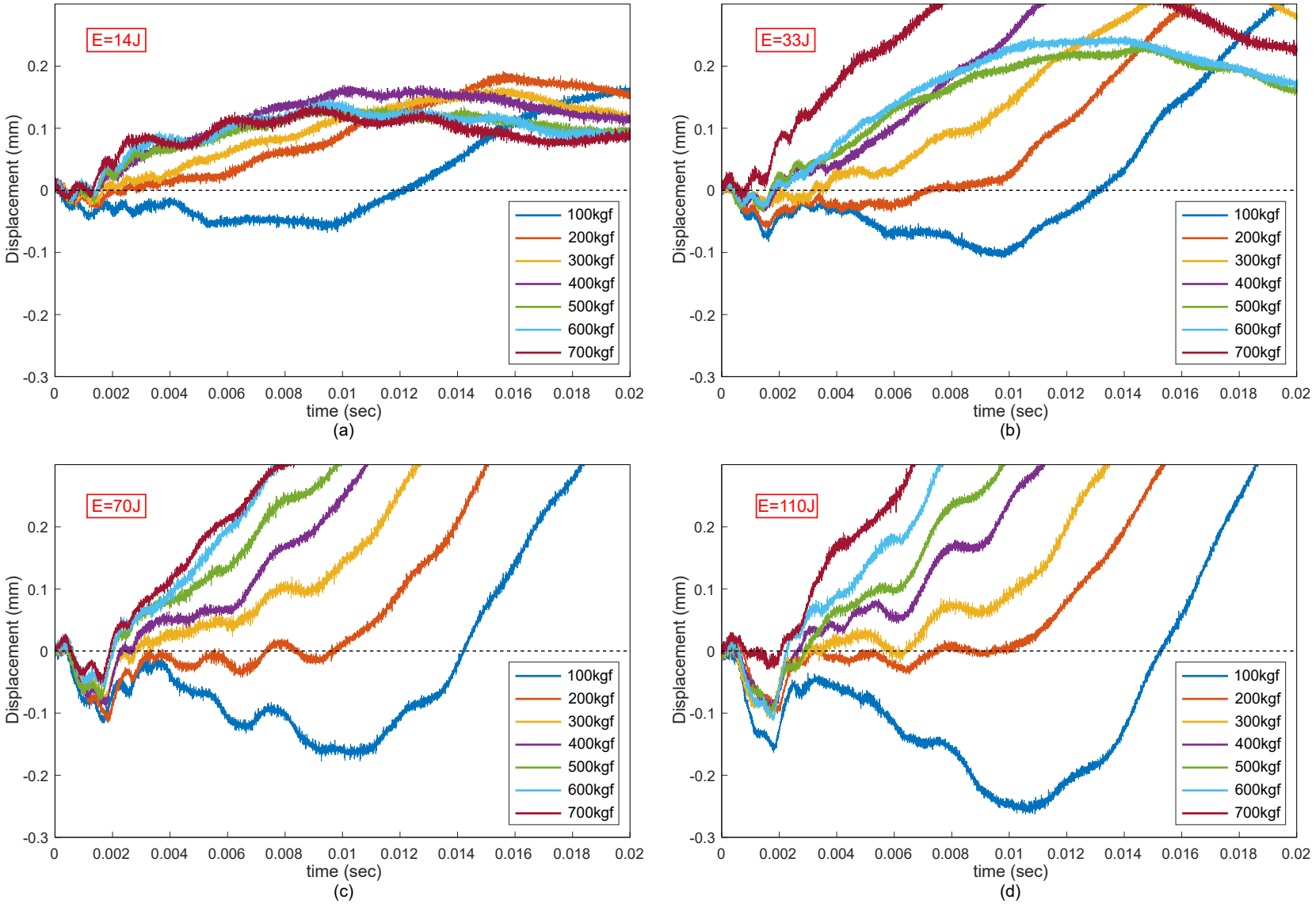

Figure 4.26: Impact number 100 of each test series described in Table 4.2. The data pertains to the laser sensor used to monitor the displacement of the barrel (Laser Sensor 2): (a) impact energy=14 J, (b) impact energy=33 J, (c) impact energy=70 J, and (d) impact energy=110 J. Time "0" is the moment of impact.

Even though it is unclear what causes the rebound movement of the barrel, the results shown in Figure 4.26 are in agreement with what was observed in the data pertaining to the field experiments explained in the previous chapter. The data analysis revealed the occurrence of a drilling regime characterised by a distinct pattern of the rotary head displacement, in which a periodic motion with upward movement of the rotary head (after impact) was observed (refer to Section 3.3.6 (Chapter 3)).

Figure 4.27 presents the ROP as a function of P and the parameter N as a function of the piston impact energy. One can observe that the approximate number of impacts to clear the borehole surface (N)—for a given angular displacement between impacts—decreases with the increase of piston impact energy due to a higher propagation of cracks to adjacent craters; this, in turn, leads to better chipping and, consequently, to better material removal after each impact.

4.5.2 Influence of Indexing Angle on Drilling Performance

Several tests were carried out to investigate whether the indexing angle has any significant effect on the overall drilling performance. Table 4.3 summarises the drilling parameters considered throughout the tests. While the piston impact energy and the WOB were maintained constant, six different tests were conducted for the following indexing angles of the rock sample: 5°, 10°, 15°, 20°, 24°, and 30°. Figure 4.28 shows the drill bit coverage profile (of one revolution (360°)) for each indexing angle considered for the experiments.

Figure 4.29 shows how the piston impact velocity—and consequently the impact energy—was maintained during the tests. There was no major issue, and the air regulator managed to maintain the desired air pressure in the reservoir, meaning that the piston velocity could be controlled consistently throughout the tests. Conversely, the average piston rebound velocity was slightly different for each test, indicating that the transmission of energy during the drill bit penetration is dependent on the indexing angle.

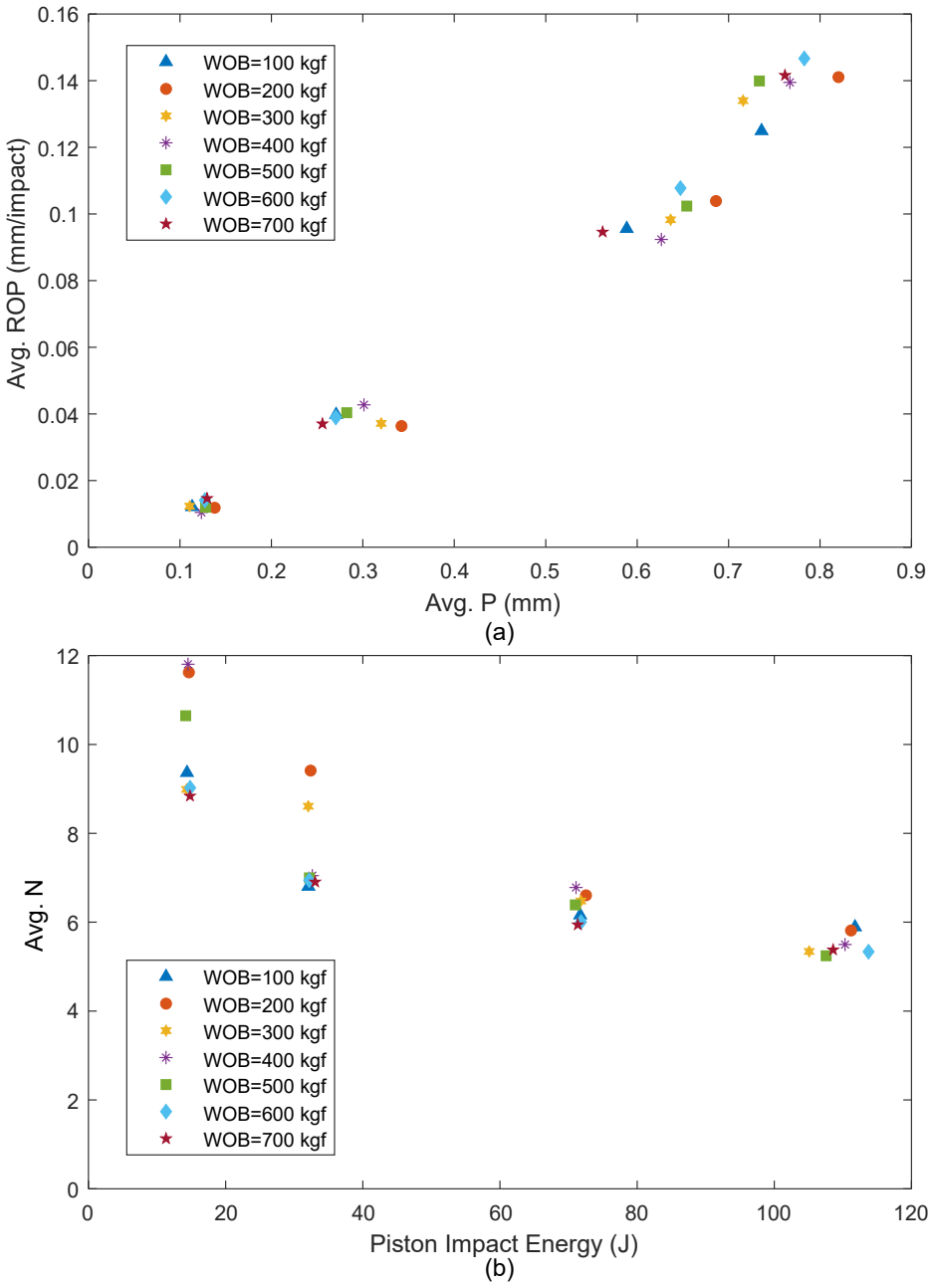

Figure 4.27: Results from all test series described in Table 4.2 (impact energy=14, 33, 70, and 110 J, indexing angle=24°, WOB=from 100 kgf up to 700 kgf). (a) ROP as a function of P, and (b) average N as a function of piston impact energy.

Test	Piston Selected	Impact Energy (J)	WOB (kgf)	Indexing Angle (°)	Number of Impacts
1	Piston 2	33	400	5	210
2	Piston 2	33	400	10	210
3	Piston 2	33	400	15	210
4	Piston 2	33	400	20	210
5	Piston 2	33	400	24	210
6	Piston 2	33	400	30	210

Table 4.3: Summary of the tests carried out to investigate the influence of the indexing angle on the drilling performance.

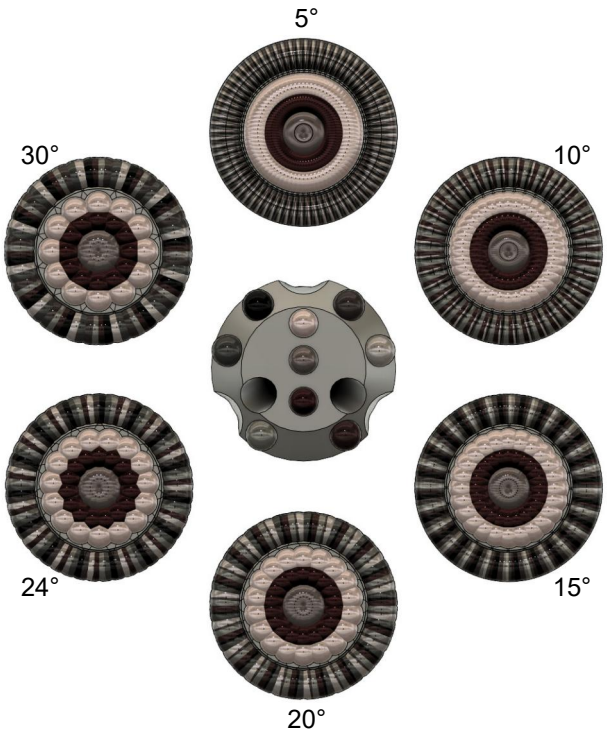

Figure 4.28: Drill bit coverage profile (360°) for different indexing angles (generated on the software Autodesk Fusion 360 (Autodesk, 2023)).

Moreover, the air compressor had no problem rapidly re-pressurising the air reservoir while the indexing table turned the rock after each piston impact. The impact frequency of three impacts per minute was achieved (not considering the time for cleaning the borehole).

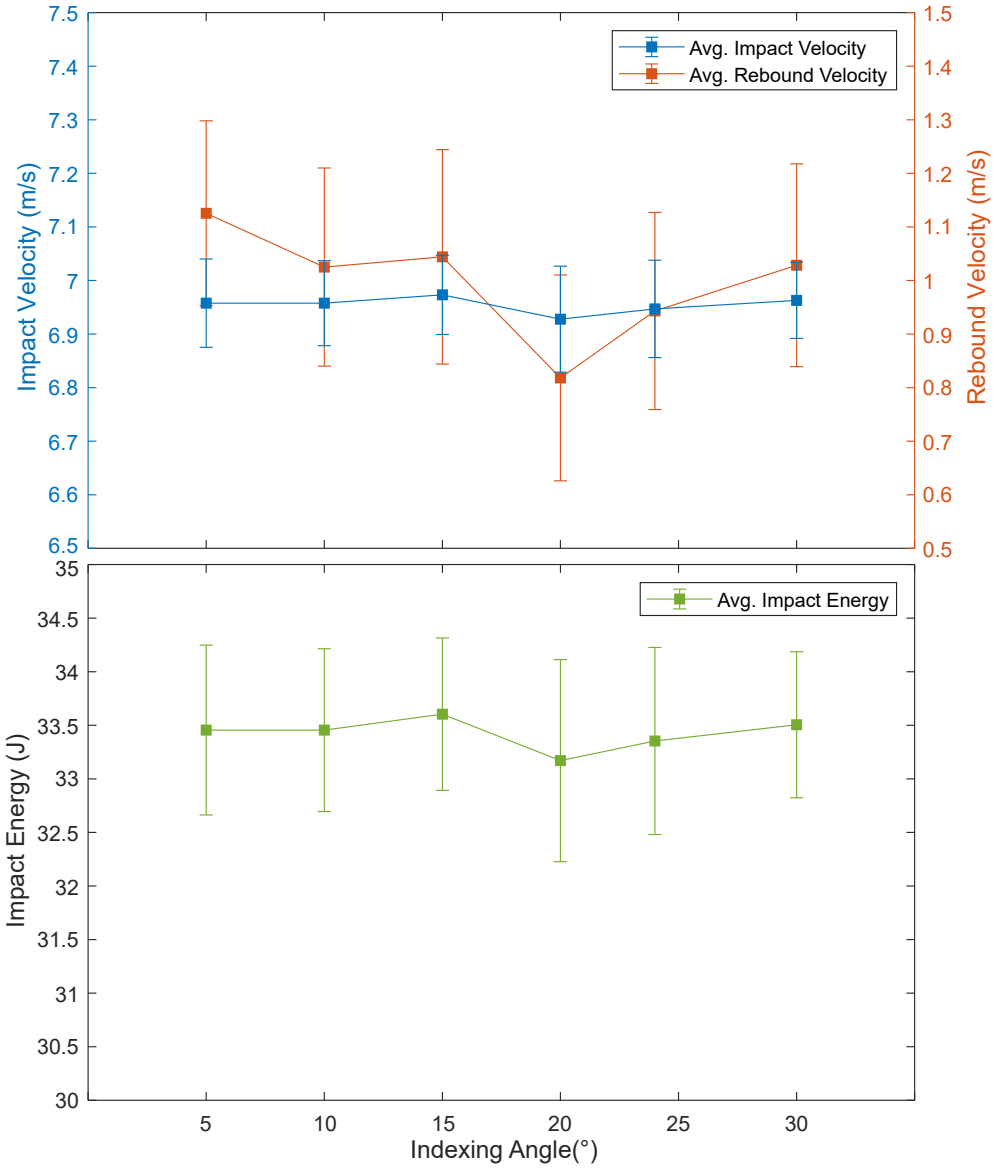

Figure 4.29: Piston impact velocity, rebound velocity, and impact energy for the tests described in Table 4.3 (impact energy=33 J, WOB=400 kgf, indexing angle=5°, 10°, 15°, 20°, 24°, and 30°).

A total of 210 impacts were performed during each test described in Table 4.3. To estimate the rate of propagation ROP of each test, the last 90 successive piston impacts were considered, as shown in Figure 4.30. One can observe that the parameter indexing angle affects the ROP, indicating that the ratio of the angular velocity over the piston activation frequency is important to be monitored during drilling activities; this can be considered in data-driven drilling

optimisation strategies.

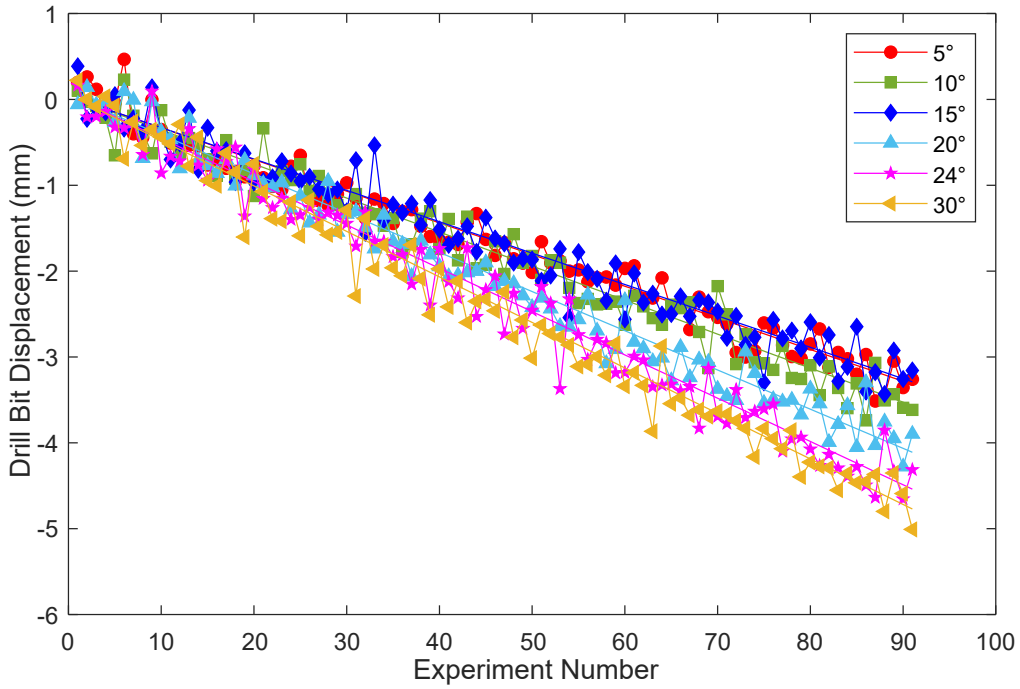

Figure 4.30: Data from the last 90 experiments pertaining to the tests described in Table 4.3 (impact energy=33 J, WOB=400 kgf, indexing angle=5°, 10°, 15°, 20°, 24°, and 30°). Each data point corresponds to the initial position of the drill bit at each experiment.

Figure 4.31 presents the average borehole rate of propagation and the average drill bit penetration per piston impact for different values of indexing angle (refer to Table 4.3). The parameter P did not vary significantly with the change in indexing angle; it increased approximately 16% from the tests with the lowest average penetration (indexing of 15°) to the tests with the highest penetration (indexing of 25°). However, a significant increase in the ROP was observed; this parameter increased by about 45% when the indexing angle changed from 15° to 30°. Moreover, Figure 4.32 presents the ROP as a function of P and also the parameter N as a function of the indexing angle for the tests described in Table 4.3. It is evident that the approximate number of impacts to clear the borehole surface (N) is dependent on the drill bit angular displacement between two successive piston impacts.

The results of the tests, considering different indexing angles, indicate that better drilling performance can be achieved by readjusting the angular velocity of the drill bit for a given piston impact frequency.

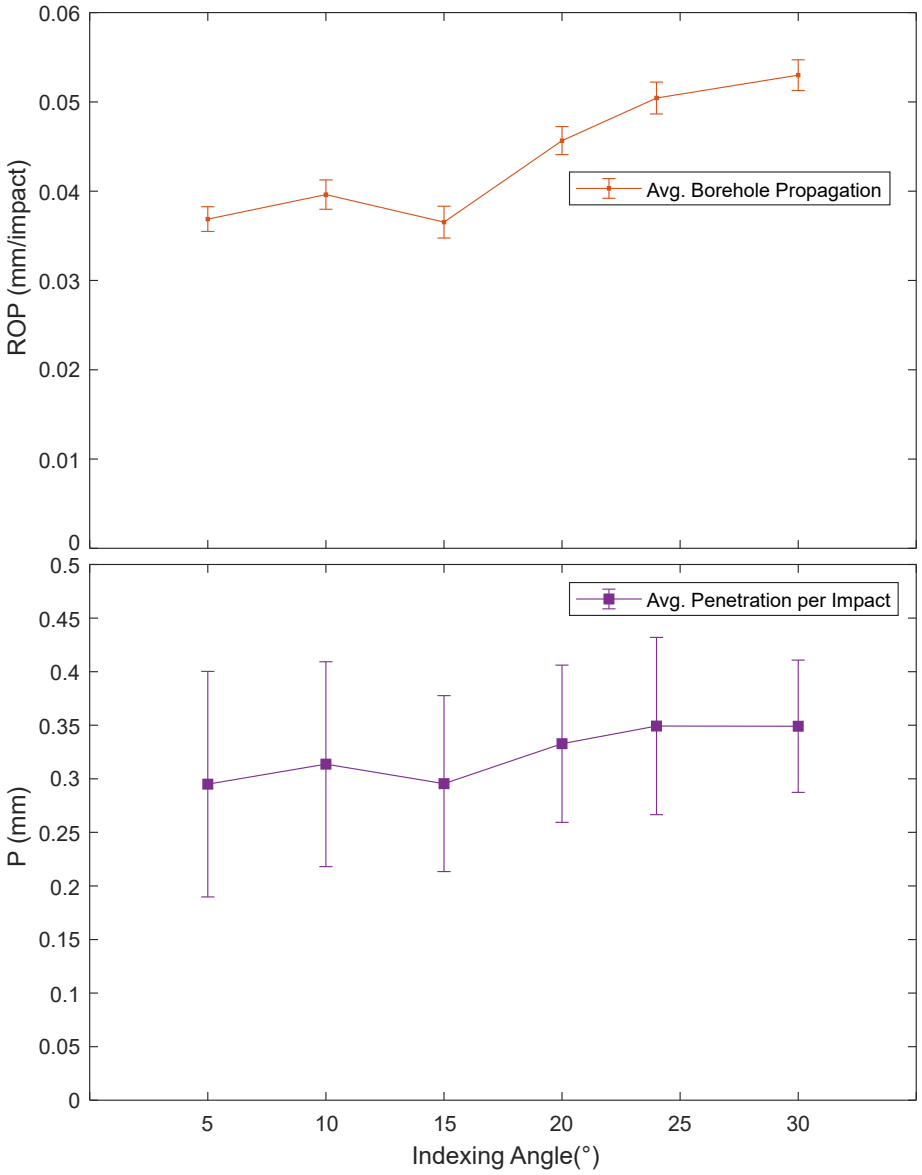

Figure 4.31: Average ROP and average P for the tests described in Table 4.3 (impact energy=33 J, WOB=400 kgf, indexing angle=5°, 10°, 15°, 20°, 24°, and 30°).

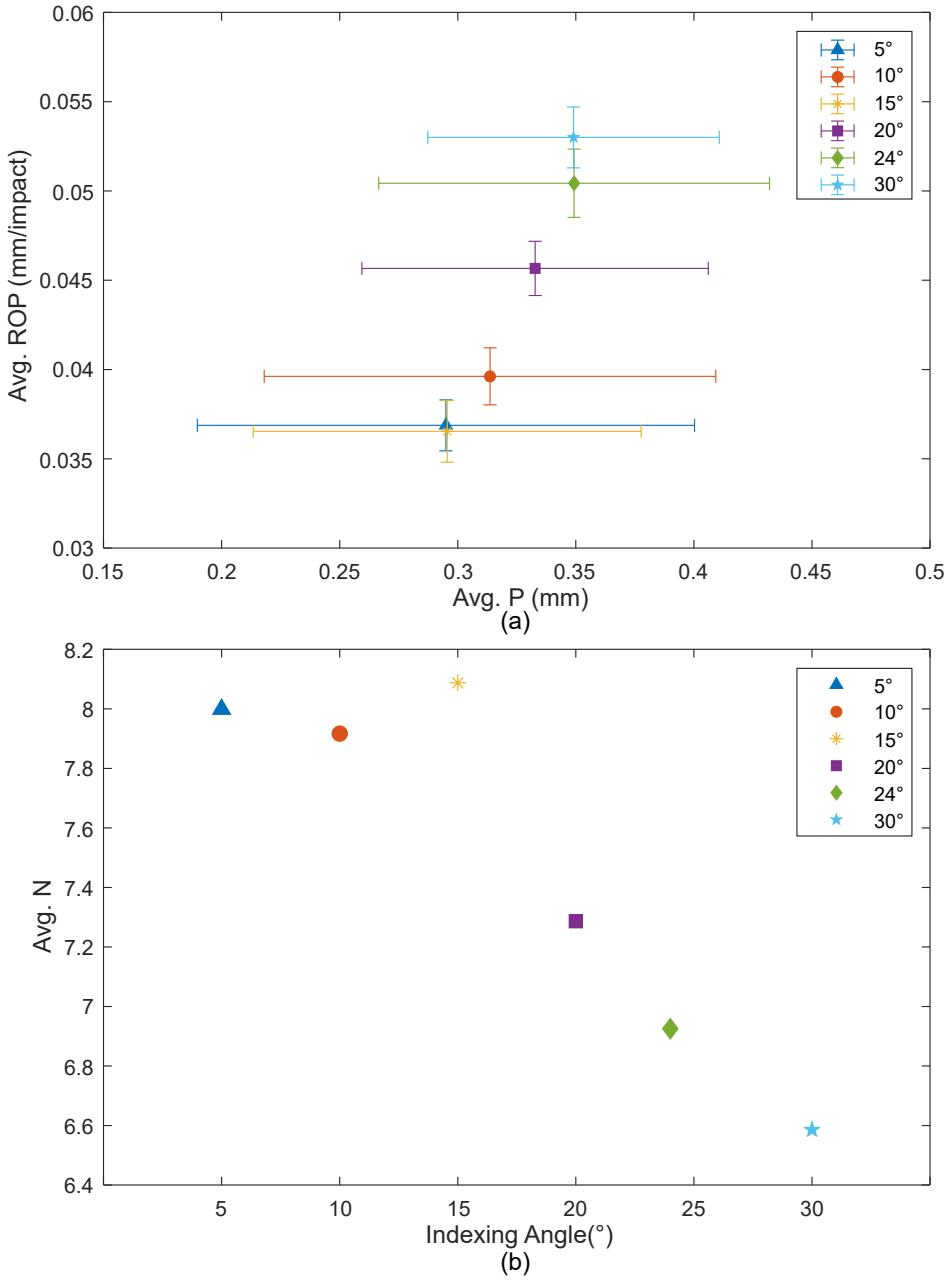

Figure 4.32: Results from the tests described in Table 4.3 (impact energy=33 J, WOB=400 kgf, indexing angle=5°, 10°, 15°, 20°, 24°, and 30°). (a) *ROP* as a function of P, and (b) average N as a function of indexing angle.

4.5.3 Influence of Cleaning on Drilling Performance

Tests were carried out to evaluate the effect of accumulated material in the borehole (cuttings and powder) on the overall drilling performance. There was no *Collaring Phase* prior to these experiments, meaning that new boreholes were drilled at each test. Table 4.4 summarises the drilling parameters considered during the tests. The drilling parameters were equal for both tests and were maintained constant. However, the cleaning protocol was different; for one of the tests, the borehole was not cleaned at all, whereas for the other test, the borehole was always perfectly cleaned after two piston impacts (from start to finish).

Test *	Piston Selected	Impact Energy (J)	WOB (kgf)	Indexing Angle (°)	Number of Impacts
1	Piston 2	80	400	24	282
2	Piston 2	80	400	24	228

* - During Test 1 the borehole surface was not cleaned throughout the entire run; whereas during Test 2 the borehole surface was always cleaned after two impacts.

Table 4.4: Summary of the tests carried out to investigate the influence of cleaning on the drilling performance.

As shown in Figure 4.33, both tests were terminated at the same borehole depth, which was about 29 millimetres deep. It was necessary 54 extra piston impacts in *Test 1* for such desired borehole depth to be achieved. Note that both curves propagated similarly for a borehole depth of 15 millimetres or lower due to the fact that the experiments are conducted horizontally, so there is no material build-up inside the hole (since the cuttings fall outside). However, once the borehole becomes deeper, cuttings and powder (dust) begin to accumulate on the lower section of the borehole (refer to Figure 4.34), which in turn affects the transmission of energy from the drill bit to the rock sample.

Figure 4.35 shows how the piston impact velocity—and consequently the impact energy—was maintained during the tests. Even though there was no major issue with the compressor and the piston velocity was maintained consistently for both tests, a short period of time was necessary between successive experiments

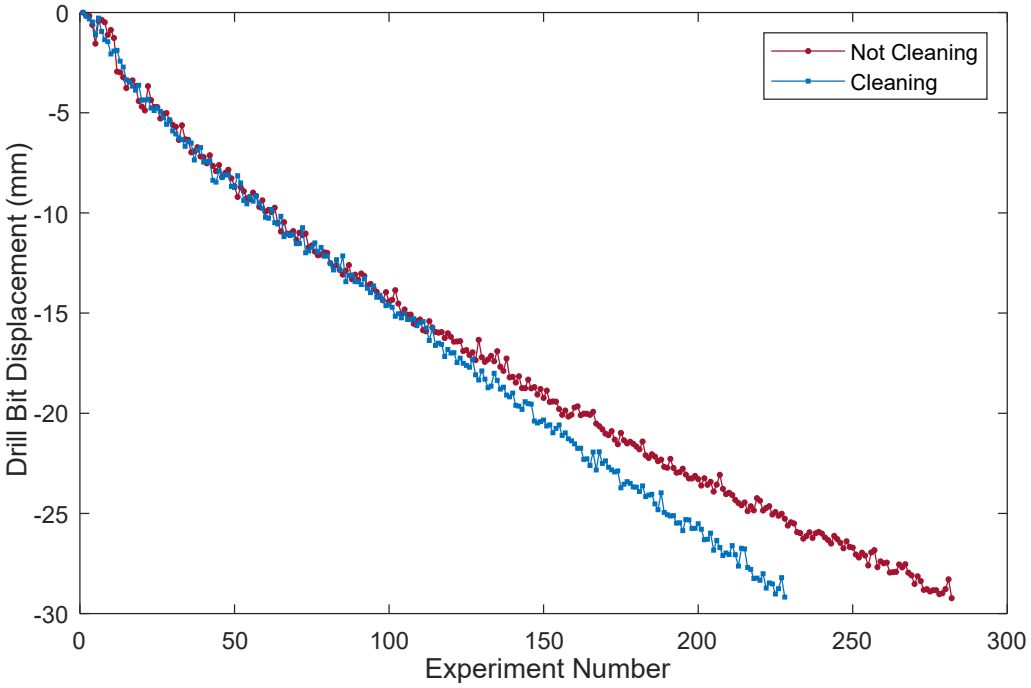

Figure 4.33: Data points for the tests described in Table 4.4 (impact energy=80 J, indexing angle=24°, WOB=400 kgf). Each point corresponds to the initial position of the drill bit.

Figure 4.34: Significant cuttings and powder (dust) accumulation in the borehole. Picture taken at the end of *Test 1* (impact energy=80 J, indexing angle=24°, WOB=400 kgf).

for the desired air pressure (in the reservoir) to be achieved. As a result, the impact frequency achieved was slightly less than two impacts per minute (not considering the time for cleaning the borehole during *Test 2*). Furthermore, the piston rebound velocity was also estimated for both tests, as shown in Figure 4.35. The average rebound velocity was slightly lower for *Test 1*, but the dispersion was considerably higher. This indicates that the extra material between the drill bit buttons and the rock surface affects the transmission of energy to the rock and makes the energy transmission more inconsistent.

In order to estimate the average ROP for both tests, the last 150 piston impacts were considered (refer to Figure 4.36); this comprises ten complete drill bit revolutions for the indexing angle of 24°. The change in performance due to a perfect surface cleaning protocol is evident. Figure 4.37 presents the average ROP and the average P for both tests. While the drill bit penetration presented no significant difference between both tests, the rate of propagation of the borehole increased by approximately 50 % once the cleaning process commenced.

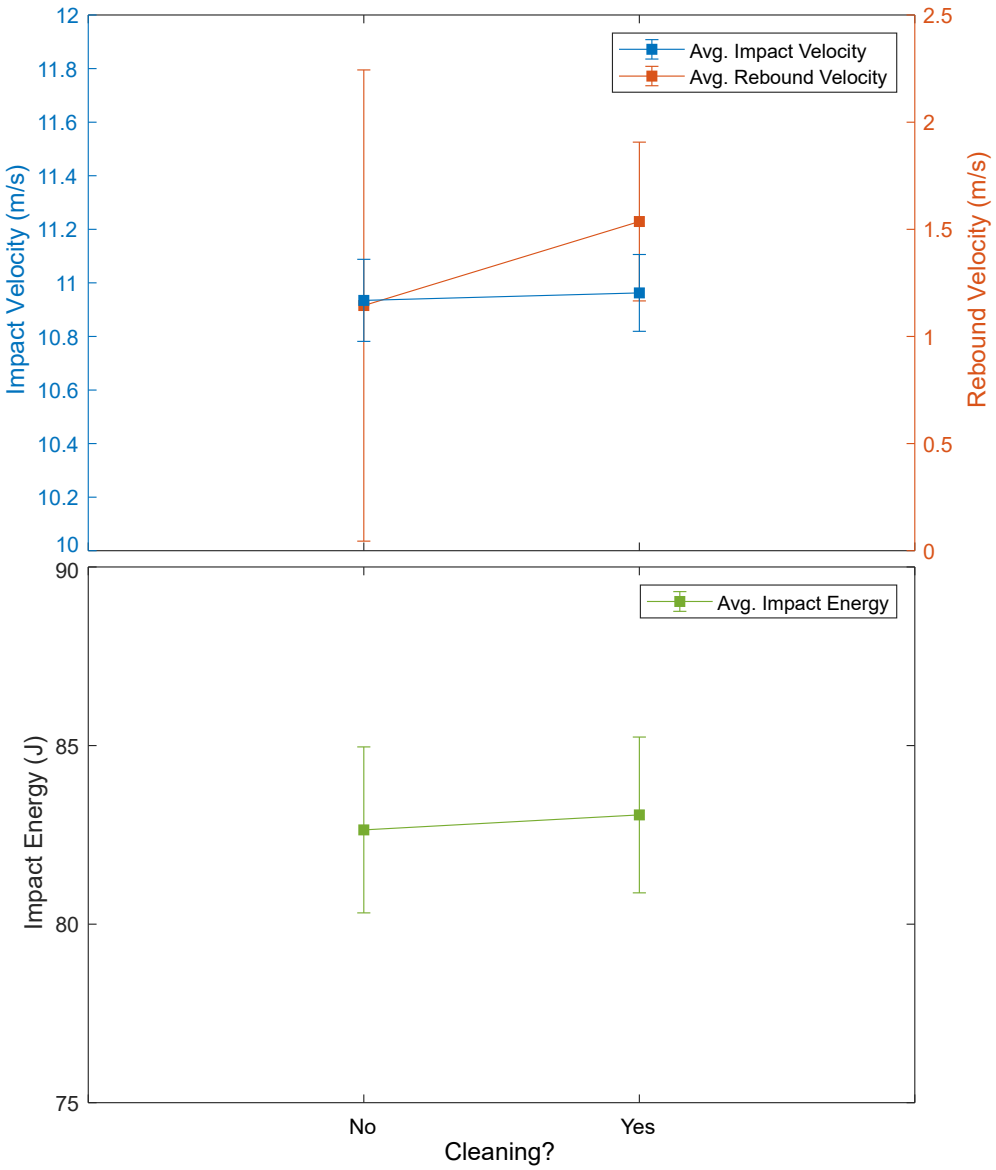

Figure 4.35: Piston impact velocity, rebound velocity, and impact energy for the tests described in Table 4.4 (impact energy=80 J, indexing angle=24°, WOB=400 kgf).

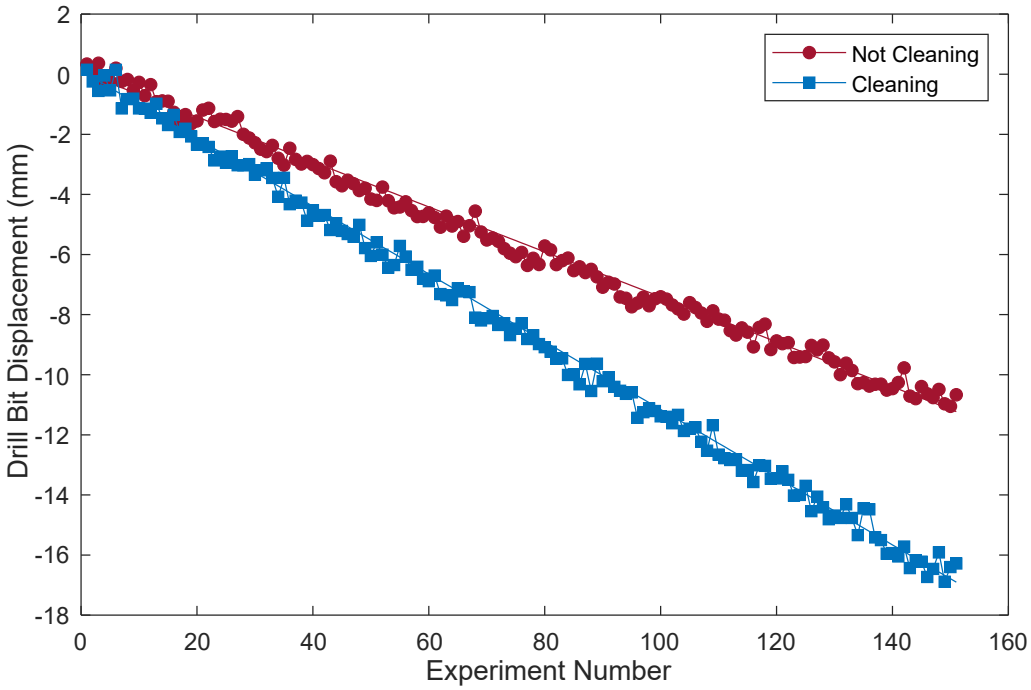

Figure 4.36: Data from the last 150 experiments pertaining to the tests described in Table 4.4 (impact energy=80 J, indexing angle=24°, WOB=400 kgf). Each data point corresponds to the initial position of the drill bit at each experiment.

4.6 Concluding Remarks

In this chapter, the experimental setup *Woody* was presented. The main difference between our experimental setup and the equipment reported in the literature for percussive drilling is the ability to drill shallow holes with a succession of discrete events, one piston impact at a time. The initial conditions between two successive piston impacts are always re-established, meaning that the desired axial load (weight) is guaranteed to be applied to the drill bit before any piston impact. This allows us to evaluate the true effect of the WOB on the overall drilling performance. Additionally, the percussive drilling experiments conducted on *Woody* also allow the investigation of the piston impact energy and indexing angle.

Three distinct percussive drilling experimental programs were carried out on Blue Stone Granite rock samples:

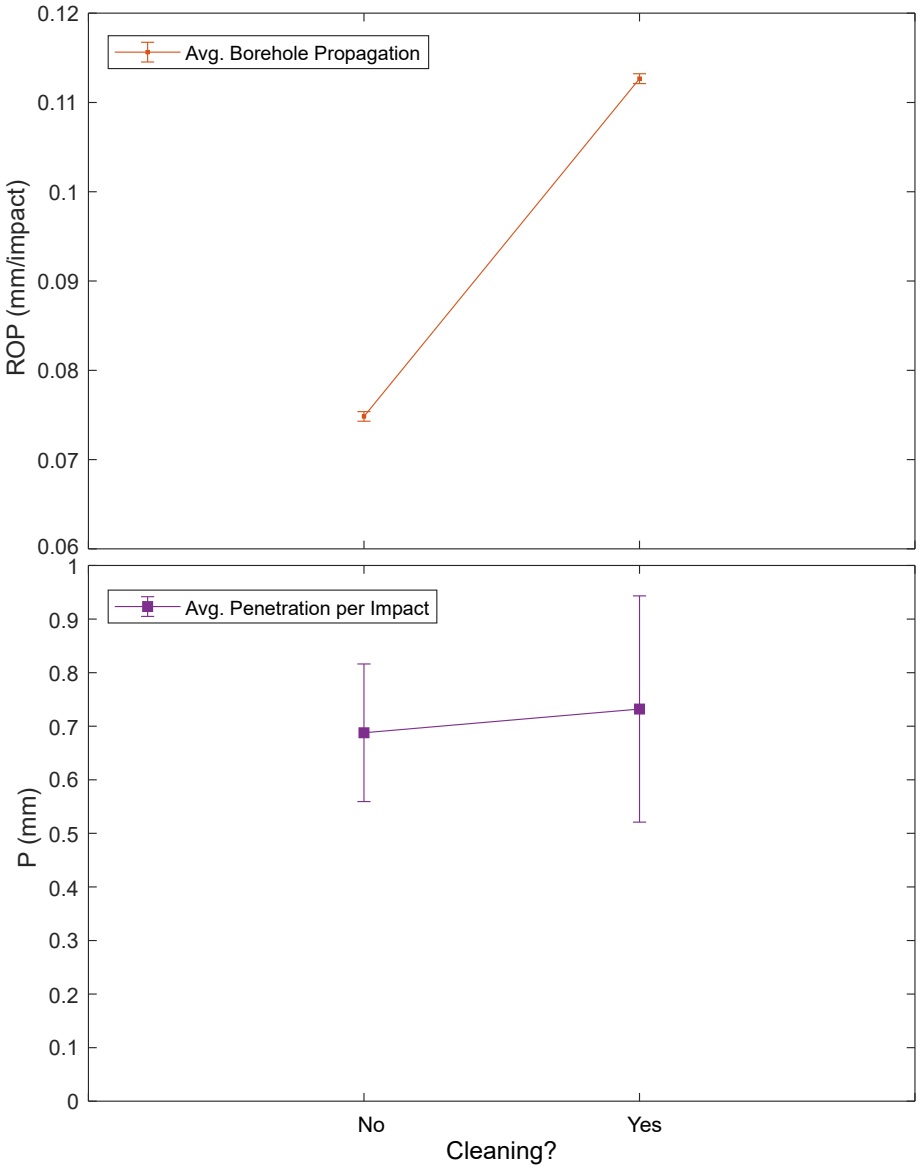

Figure 4.37: Average ROP and average penetration per impact P for the tests described in Table 4.4 (impact energy=80 J, indexing angle=24°, WOB=400 kgf). Borehole with an accumulation of material throughout the experiments, and test with an appropriate cleaning protocol in place.

- **Program 1** - The main objective was to evaluate whether the WOB affects the overall drilling performance. Four different extensive test series were conducted, in each of which seven different values of WOB were evaluated—from 100 kgf up to 700 kgf—while the indexing angle of the rock sample was maintained constant over all experiments; moreover, a different piston impact energy was considered for each test series. The results of the tests revealed that the overall drilling performance does not depend on the WOB. While the average borehole propagation (ROP) and the average drill bit penetration per impact (P) varied with increasing piston impact energy, both parameters presented insignificant changes for different WOB values. Conversely, the axial load applied to the bit affected the time the outer shaft (or barrel) takes to re-establish contact with the drill bit after each piston impact.

- **Program 2** - Several tests were conducted to evaluate a possible dependence of the overall drilling performance on the indexing angle. Six different indexing angles were selected—5°, 10°, 15°, 20°, 24°, and 30°—while the piston impact energy and WOB were maintained constant. The drill bit penetration per piston impact P did not change significantly for different indexing angles. However, the average borehole propagation ROP increased by about 45% when the indexing angle changed from 15° to 30°.

- **Program 3** - Two tests were conducted to evaluate the effect of accumulated material in the borehole (cuttings and powder) on the overall drilling performance. The drilling parameters WOB, piston impact energy, and indexing angle were maintained equal and constant for both tests. The only difference between both tests was the cleaning protocol implemented. For one test, the borehole was not cleaned throughout the experiments, whereas for the other test, the borehole was cleaned after two successive piston impacts. Even though the average drill bit penetration P did not change significantly when the cleaning protocol was implemented, the borehole rate

of propagation ROP increased by about 50%. Moreover, the analysis of the rebound velocity indicated that the transmission of energy—from the drill bit to the rock—is more inconsistent with the presence of extra loose material between the drill bit buttons and the rock surface.

Chapter 5

Conclusion

The overarching objective of this research project was to acquire a better understanding of the mechanisms associated with the drilling action of a DTH hammer system, with a particular focus on the reported *Optimum Drilling State*. There is no consensus in the literature on the root cause of such a phenomenon in percussive drilling. Our main focus was to determine whether the ODS stems from an intrinsic property of the bit-rock interface. To accomplish the objectives of this work, two types of experimental procedures were carried out:

- **Full-scale Drilling Experiments** - Since most of the documented results in the literature regarding the ODS phenomenon are several decades old, the research group involved in this work decided to collect drilling data with state-of-the-art sensors and data acquisition hardware. Our team visited a mining site, instrumented a drilling rig with a tailored monitoring system, and collected drilling data over a period of three days. The major outcomes of the field tests are summarised below:
  - I developed several algorithms to compute real-time drilling parameters, such as bit depth, hole depth, WOB, TOB, and ROP. This research work also introduced a method to monitor the dynamics of the down-hole drilling tool and determine the piston impact frequency (hammer frequency) and the drill bit penetration per impact; the al-

gorithm I developed to estimate these parameters is also detailed in this thesis.

  - During my analysis of the drilling data, evidence of the ODS phenomenon was found in several instances. However, I could not draw any conclusion related to its root cause (at this stage of the research).

  - The post-mortem analysis of the drilling data also further revealed the occurrence of different drilling regimes, characterised by distinct patterns of the rotary head displacement: (i) a periodic step-like motion with distinct plateaus where the rotary head is at full rest between impacts, (ii) a periodic motion but with the rotary head moving forward between impacts, (iii) a periodic motion with a vertical rebound of the rotary head after each impact, and (iv) the rotary head moving steadily downward without any hammer activity (bit shearing the rock).

- **Discrete Percussive Drilling Experiments** - The next stage of the research was to conduct laboratory experiments using a novel approach; the aim was to investigate the effect of the WOB on the average drilling performance. Our team designed and built equipment that can drill shallow holes with successive discrete events (one percussive activation at a time) while allowing independent control of the weight-on-bit, indexing angle, and piston impact energy. In discrete percussive drilling experiments, the idea is to mimic the percussive drilling process with the system dynamics decoupled from the bit-rock interface. The barrel (hammer outer shaft) is guaranteed to be in contact with the drill bit before each percussive activation; this ensures that an appropriate weight is applied to the bit before each piston impact. The following are the major outcomes of the laboratory experiments:

  - (Program 1) 28 holes (several centimetres deep) were drilled with a

70-millimetre (⌀) drill bit and under constant impact energy, weight-on-bit and indexing angle. For each impact energy (14, 33, 70, and 110 J), the WOB was varied from 1 to 7 kN. The results of the tests show that the WOB does not affect the average ROP, but it does affect the time it takes for the barrel (or hammer outer shaft) to re-establish full contact with the drill bit after each piston impact.

- (Program 2) Tests were carried out considering different indexing angles (5°, 10°, 15°, 20°, 24°, and 30°) while the piston impact energy and WOB were maintained constant. Even though the average drill bit penetration (per piston activation) did not present any significant change during the tests, the average ROP increased by about 45% when the indexing angle changed from 15° to 30°. The results of the tests show that the indexing angle affects the drilling performance, which means that the ROP can be optimised by readjusting the angular velocity of the drill bit for a given piston impact frequency.
- (Program 3) The drilling parameters WOB, piston impact energy, and indexing angle were maintained equal and constant throughout two distinct tests. The only difference was the cleaning protocol implemented; in one test the hole was properly cleaned after two successive piston activations, whereas for the other test, the cuttings were never removed during the experiments. The average ROP decreased approximately 50% due to the accumulation of material (cuttings) in the hole; this indicates that it is of significant importance to appropriately clean the borehole during drilling.

This work concludes that the ODS phenomenon is not intrinsic to the bit-rock interface and appears to be related to the system dynamics. While the axial load (weight) applied to the drill bit does not affect the average ROP (as observed in the laboratory tests), it does affect the dynamic response of the DTH hammer system. The time the barrel (or hammer outer shaft) takes to

re-establish contact with the drill bit is directly proportional to the WOB. In an actual drilling process, the hammer period (T_1) and the outer shaft recovery time (T_5) are both in the order of O(0.01)s (refer to Chapter 2 (Section 2.2)). There exists a minimum WOB that ensures that $T_5 < T_1$; this condition guarantees that appropriate weight is applied to the bit at each percussive cycle. However, this condition is not guaranteed to be met during drilling. The asynchronous interaction between the hammer system's components—outer shaft, piston, and drill bit—may be related to the occurrence of the ODS phenomenon. Further tests are necessary to investigate the interaction between the barrel and drill bit after each piston impact; it is unclear what causes the barrel to move backward (away from the rock) for low WOB.

It is important to emphasise that the accumulation of material inside the borehole, the indexing angle of the drill bit, and the piston impact energy indeed affect the overall drilling performance. However, it is unlikely that the ODS phenomenon is attributed to them. The analysis of the data from the field tests shows an abrupt change of the ROP—up to fourfold in a few instances—in a short period of time while the indexing angle and piston impact frequency change monotonically. Additionally, during the same period of time, it is unlikely that an excessive amount of cuttings can be accumulated between the drill bit and the borehole bottom. Nonetheless, it is important to mention that the parameters indexing angle and piston impact frequency, as well as the ability to clean adequately the borehole bottom (during drilling), are vital in the context of drilling optimisation and need to be considered.

5.1 Thesis Contribution and Future Work

This research offers valuable contributions to both academic knowledge and industrial applications:

1. **Novel platform to study percussive drilling** - The development of *Woody* allows our research group to study percussive drilling further. The drilling parameters WOB, indexing angle, and piston impact energy can be investigated independently with this unique apparatus. The results of the tests to assess the effect of WOB on the drilling performance are major contributions of this thesis. These results show that the parameter WOB does not affect the transmission of energy from the drill bit to the rock (at each percussive cycle) but affects the hammer system dynamics.

2. **Distinctive drilling data** - A full-scale drilling rig was instrumented with our custom-built monitoring system, and unique drilling data was acquired during field experiments. The data related to the ODS phenomenon and the different drilling regimes interpreted from surface measurements are also major contributions of this thesis. The data gives us insight into the drilling dynamics of the DTH hammer system. Additionally, a second drilling rig (refer to Figure 5.1) was also instrumented[1] with state-of-the-art sensors and extra drilling data was collected, expanding our database and allowing our research group to continue investigating the intricate dynamics involved in DTH percussive drilling.

3. **Algorithms for real-time data processing** - The algorithms developed throughout this research project were instrumental in the development of an embedded real-time control system, which can be used to estimate the following parameters during the drilling process: bit depth, hole depth, TOB, WOB, ROP, indexing angle, hammer frequency, and drill bit penetra-

[1]The sensors and data acquisition system are explained in Chapter 3 (Section 3.1.1).

tion per impact. Such parameters can be visualised on the Windows-based graphical user interface shown in Figure 5.2.

Recommendation of Future Work

Our research group will continue the study of percussive drilling by conducting extra experiments on *Woody*. The following recommendations can be followed:

- The barrel should be upgraded and a heavier piston (with the same length) should be used. Consequently, a new air compressor will also be needed. The idea is to conduct the same experiments described in this thesis but for impact energies superior to 200 J (to be more comparable to the drilling data acquired during the field tests).

- More tests should be conducted to strengthen the generalizability and applicability of this research. For instance, different indexing angles could be explored for different rock types and piston impact energies. Different drill bits, with distinct bit button shapes, could also be used during the experiments. The apparatus could even be modified to incorporate confining pressure effects, a critical factor influencing rock failure modes after bit indentation.

- The drill bit and barrel could be equipped with strain gauges, allowing strain analysis. The idea is to have a better understanding of the barrel's displacement from the moment of the piston impact until the contact with the drill bit is re-established. Further investigation is necessary to assess what causes the backward movement of the barrel for low WOB values. Moreover, force-penetration curves could be extracted during discrete percussive drilling tests to clarify the WOB effect on the bit-rock interaction.

- Experiments can be conducted with different pistons to assess how the piston's shape, mass, and length affect the overall drilling performance (considering the same drilling parameters).

- Discrete percussive drilling experiments can also be used to investigate and define optimum drilling parameters for a specific hammer system or rock. For instance, the barrel could be upgraded, and a specific hammer system—identical to the hammer system used in the field—could be used. The idea would be to map the barrel recovery time for different WOB values and piston impact energies. Then, the acquired information could be integrated into a control algorithm and be used in the field to control the drilling rig. The algorithm would optimise (in real time) the WOB according to the piston impact frequency to ensure that the hammer outer shaft re-establishes contact with the drill bit before the subsequent piston impact. The same idea could also be used to explore optimum indexing angles for a specific drill bit.

Figure 5.1: McKay Drilling Rig 3 equipped with our custom-built monitoring system. The picture was taken in Swam Valley (Western Australia) during the final tests before deploying the rig to a mining site.

Figure 5.2: Windows-based Graphical User Interface (GUI) available to the drill operator. The algorithms developed throughout this research project were optimised for real-time applications.

Appendices

Appendix A

Algorithms to Estimate Bit Depth and Hole Depth

This section presents the algorithms developed to estimate the bit depth and hole depth parameters.

A.0.1 State Machine for modeling drilling activities

Several drilling operations were modelled using the finite-state machine (FSM) concept, defined by a list of states, its initial state, and inputs that trigger transitions from one state to another.

Figure A.1 shows an example of an FSM. It consists of three states (**State 1**, **State 2**, and **State 3**), with the transition from one state to another governed by the variables **Var1** and **Var2**. In **State 1**, **Var1** is set to "0". The state machine will shift to **State 2** once **Var2** becomes equal to "ON". No action will occur once the **State 2** is reached. However, once **Var 2** becomes equal to "OFF", the state machine will shift to **State 3**. Note that through the transition from **State 2** to **State 3**, **Var1** will be set to "1". No action will occur once the **State 3** is reached. Finally, the state machine will return to its initial state (**State 1**) if **Var1** becomes equal to "0".

The state diagram from Figure A.1 is represented by Table A.1.

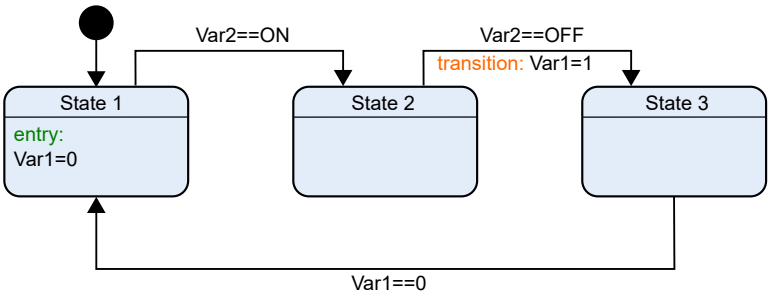

Figure A.1: State machine example.

State		Transition		
Name	Action	**Condition**	**Action**	**Next State**
State 1	Var1=0	Var2==ON	-	State2
State 2	-	Var2==OFF	Var1=1	State 3
State 3	-	Var1==0	-	State 1

Table A.1: Description of the state machine example.

A.0.2 Computation of Bit Depth and Hole Depth

The transitions (from one state to another) of the FSMs presented in Appendices A and B, are governed by each status shown in Table A.2. Each status was defined according to specific threshold values based on our analysis of the data set available.

Parameter	**Analog Sensor Range**	**Status**
Head Position(u_1)	$u_1 \geq 8$ m	TOP
	1 m $< u_1 <$ 8 m	MIDDLE
	$u_1 \leq$ 1m	BOTTOM
Air Flow(u_2)	$u_2 \geq 200$ scfm	ON
	$u_2 < 200$ scfm	OFF
RPM(u_3)	$u_3 \geq 25$ rpm	ON
	$u_3 < 25$ rpm	OFF
Rotational Pressures A(u_4) and B(u_5)	$u_4 - u_5 \geq 15$ bar	CLOCKWISE
	$u_4 - u_5 < -15$ bar	ANTICLOCKWISE
Foot Clamp(u_6)	$u_6 \geq 10$ bar	OPEN
	$u_6 < 10$ bar	CLOSED
Water Flow(u_7)	$u_7 \geq 10$ lpm	ON
	$u_7 < 10$ lpm	OFF

Table A.2: Status definition for several sensors.

Making-Up and Breaking-Down Connections at the Surface

The first step is to identify how many rods have been added or removed from the drill string. Considering Figure A.2, the following possible events can occur at the surface:

(A) - Rotary head located within the **MIDDLE** region (1 m $< u_1 <$ 8 m): the drill operator makes up the connection between the top rod and the rest of the drill string.

(B) - Rotary head located within the **MIDDLE** region (1 m $< u_1 <$ 8 m): the drill operator breaks down the connection between the top rod and the rest of the drill string.

(C) - Rotary head located within the **TOP** region ($u_1 \geq$ 8m): the drill operator breaks down the connection between the rotary head and the top rod (with the rig's auxiliary arm engaged).

(D) - Rotary head located within the **TOP** region ($u_1 \geq$ 8m): the drill operator makes up the connection between the rotary head and the top rod (with the rig's auxiliary arm engaged).

(E) - Rotary head located within the **BOTTOM** region ($u_1 \geq$ 8m): the drill operator breaks down the connection between the rotary head and the drill string.

(F) - Rotary head located within the **BOTTOM** region ($u_1 \geq$ 8m): the drill operator makes up the connection between the rotary head and the drill string.

The state diagram shown in Figure A.3 was implemented in order to identify the events explained above. Its complete representation was divided into four different tables: Tables A.3, A.4, A.5, and A.6.

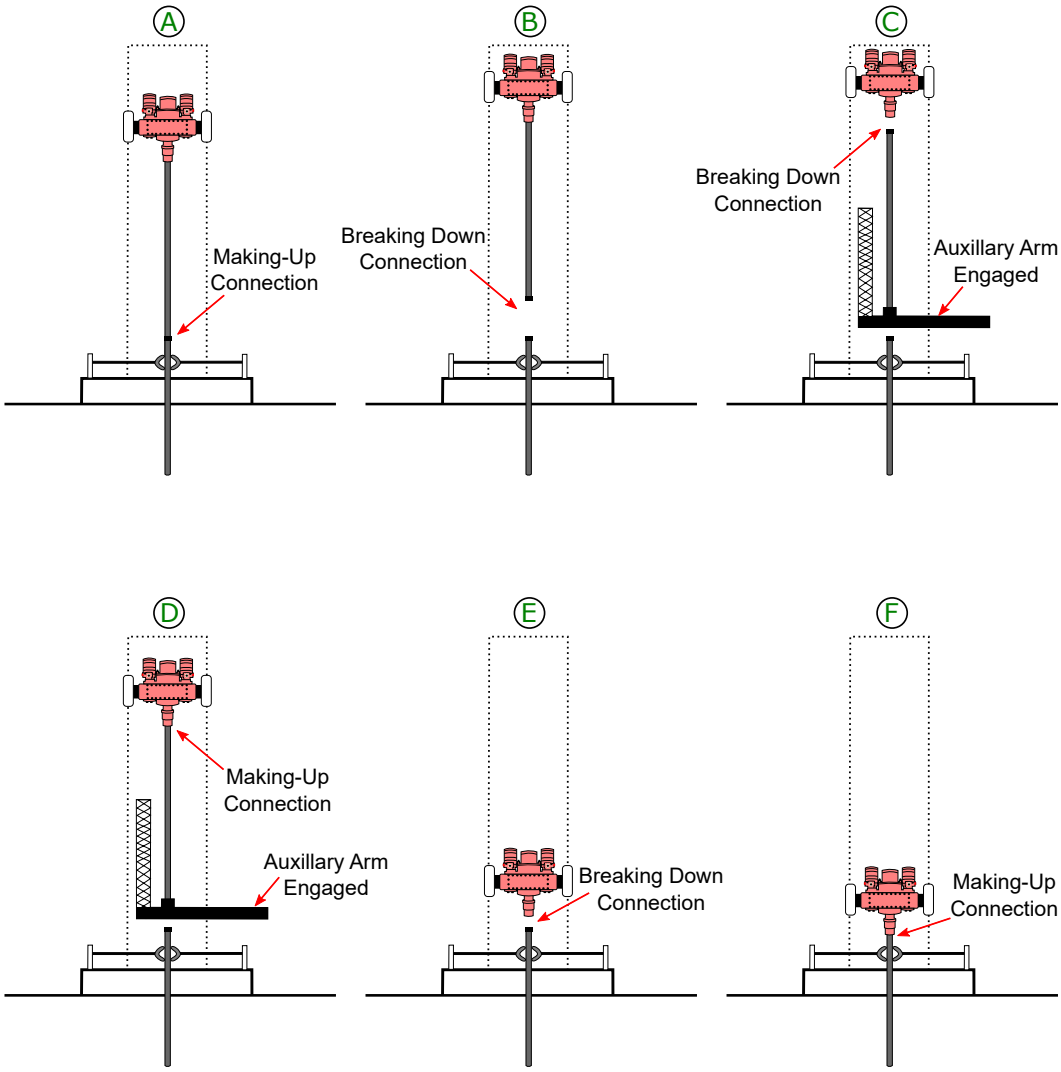

Figure A.2: Surface events to be identified.

Table A.3 describes the part of the state machine that indicates in which region (top, middle, or bottom) the rotary head is located at any given time (refer to Figure A.3).

State		Transition		
Name	Action	**Condition**	**Action**	**Next State**
Head Position	-	Position==TOP	-	TOP
	-	Position==MIDDLE	-	MIDDLE
	-	Position==BOTTOM	-	BOTTOM
TOP	-	Position==MIDDLE	C=0,D=0	MIDDLE
MIDDLE	-	Position==TOP	A=0,B=0	TOP
	-	Position==BOTTOM	A=0,B=0	BOTTOM
BOTTOM	-	Position==MIDDLE	E=0,F=0	MIDDLE

Table A.3: Description of the state diagram from Figure A.3: rotary head position.

Table A.4 represents the state machine that is active while the rotary head is within the **TOP** region. Note that the events "C" and "D" are identified once one of the final states (**Making UP** or **Breaking Down**) is reached (refer to Figure A.3).

State		Transition		
Name	Action	**Condition**	**Action**	**Next State**
Check Air Flow	-	Air Flow==OFF	-	Check Rotation
Check Rotation	-	Air Flow==ON	-	Check Air Flow
	-	Rotation==ON	-	Rotation Direction
Rotation Direction	-	CLOCKWISE	-	Making Up
	-	ANTICLOCKWISE	-	Breaking Down
Making Up	D=1	-	-	-
Breaking Down	C=1	-	-	-

Table A.4: Description of the state diagram from Figure A.3: "TOP" state.

Table A.5 represents the state machine that is active while the rotary head is within the **MIDDLE** region. Note that the events "A" and "B" are identified once one of the final states (**Making UP** or **Breaking Down**) is reached (refer to Figure A.3).

Table A.6 represents the state machine that is active while the rotary head is within the **BOTTOM** region. Note that the events "E" and "F" are identified once one of the final states (**Making UP** or **Breaking Down**) is reached (refer to Figure A.3).

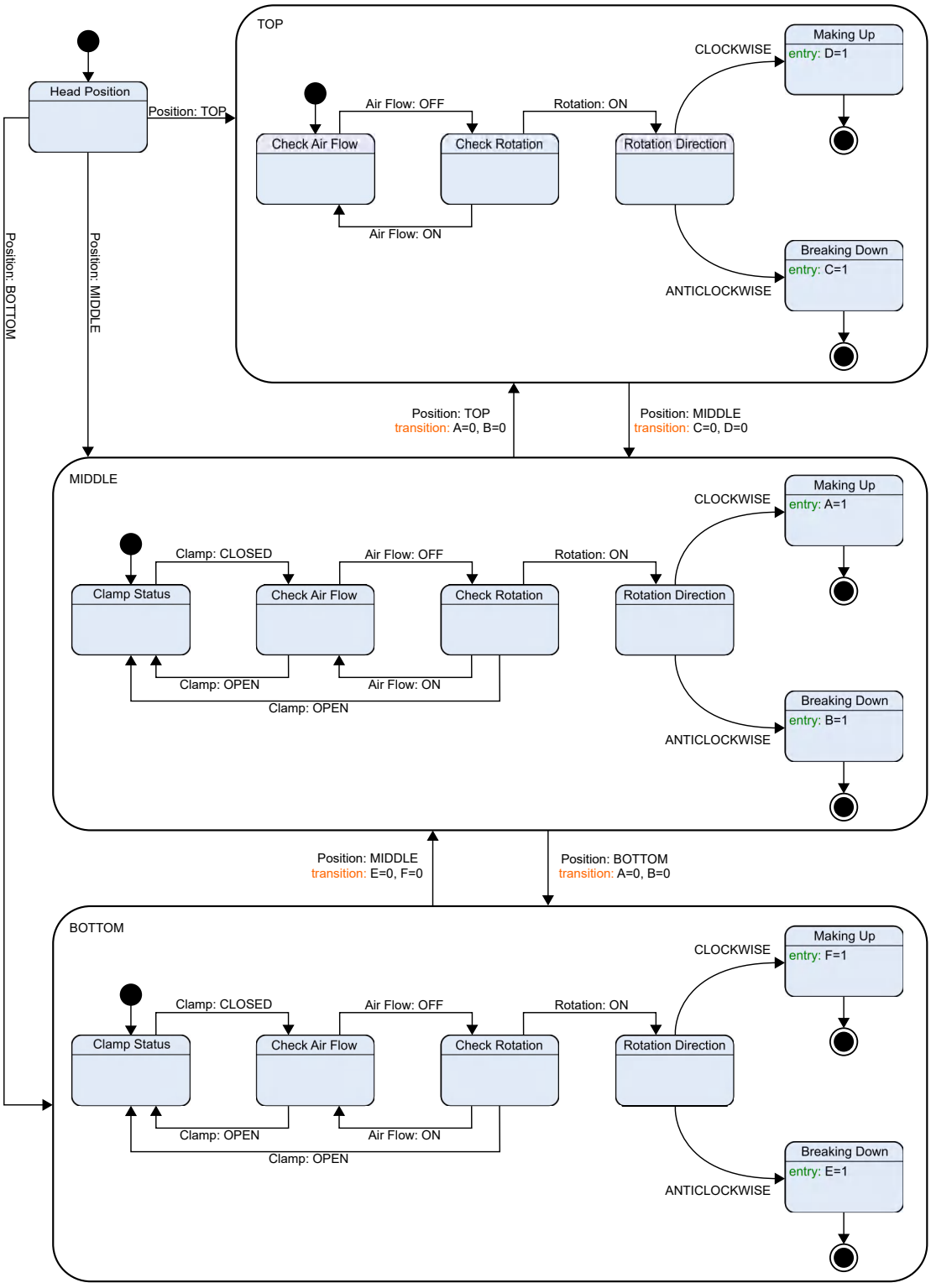

Figure A.3: State machine to identify the surface events shown in Figure A.2.

State		Transition		
Name	Action	**Condition**	**Action**	**Next State**
Clamp Status	-	Clamp==CLOSED	-	Check Air Flow
Check Air Flow	-	Clamp==OPEN	-	Clamp Status
	-	Air Flow==OFF	-	Check Rotation
Check Rotation	-	Air Flow==ON	-	Check Air Flow
	-	Clamp==OPEN	-	Clamp Status
	-	Rotation==ON	-	Rotation Direction
Rotation Direction	-	CLOCKWISE	-	Making Up
	-	ANTICLOCKWISE	-	Breaking Down
Making Up	A=1	-	-	-
Breaking Down	B=1	-	-	-

Table A.5: Description of the state diagram from Figure A.3: "MIDDLE" state.

State		Transition		
Name	Action	**Condition**	**Action**	**Next State**
Clamp Status	-	Clamp==CLOSED	-	Check Air Flow
Check Air Flow	-	Clamp==OPEN	-	Clamp Status
	-	Air Flow==OFF	-	Check Rotation
Check Rotation	-	Air Flow==ON	-	Check Air Flow
	-	Clamp==OPEN	-	Clamp Status
	-	Rotation==ON	-	Rotation Direction
Rotation Direction	-	CLOCKWISE	-	Making Up
	-	ANTICLOCKWISE	-	Breaking Down
Making Up	F=1	-	-	-
Breaking Down	E=1	-	-	-

Table A.6: Description of the state diagram from Figure A.3: "BOTTOM" state.

Rotary Head Connected to the Main Drill String

Since the events occurring at the surface can be identified (shown in Figure A.2), it is possible to detect when the rotary head is connected to the main drill string and, therefore, the parameters bit depth and hole depth can be estimated. The state diagram shown in Figure A.4 is controlled by the occurrence of the events "A", "B", "C", "D", "E", and "F". When states 2, 5, and 6 are reached (refer to Figure A.4), it is detected that the rotary head is connected to the main drill string.

The state diagram from Figure A.4 is represented by Table A.7. Note that when states 2, 5, and 6 are reached, the variable "Drillstring_connected" is set to

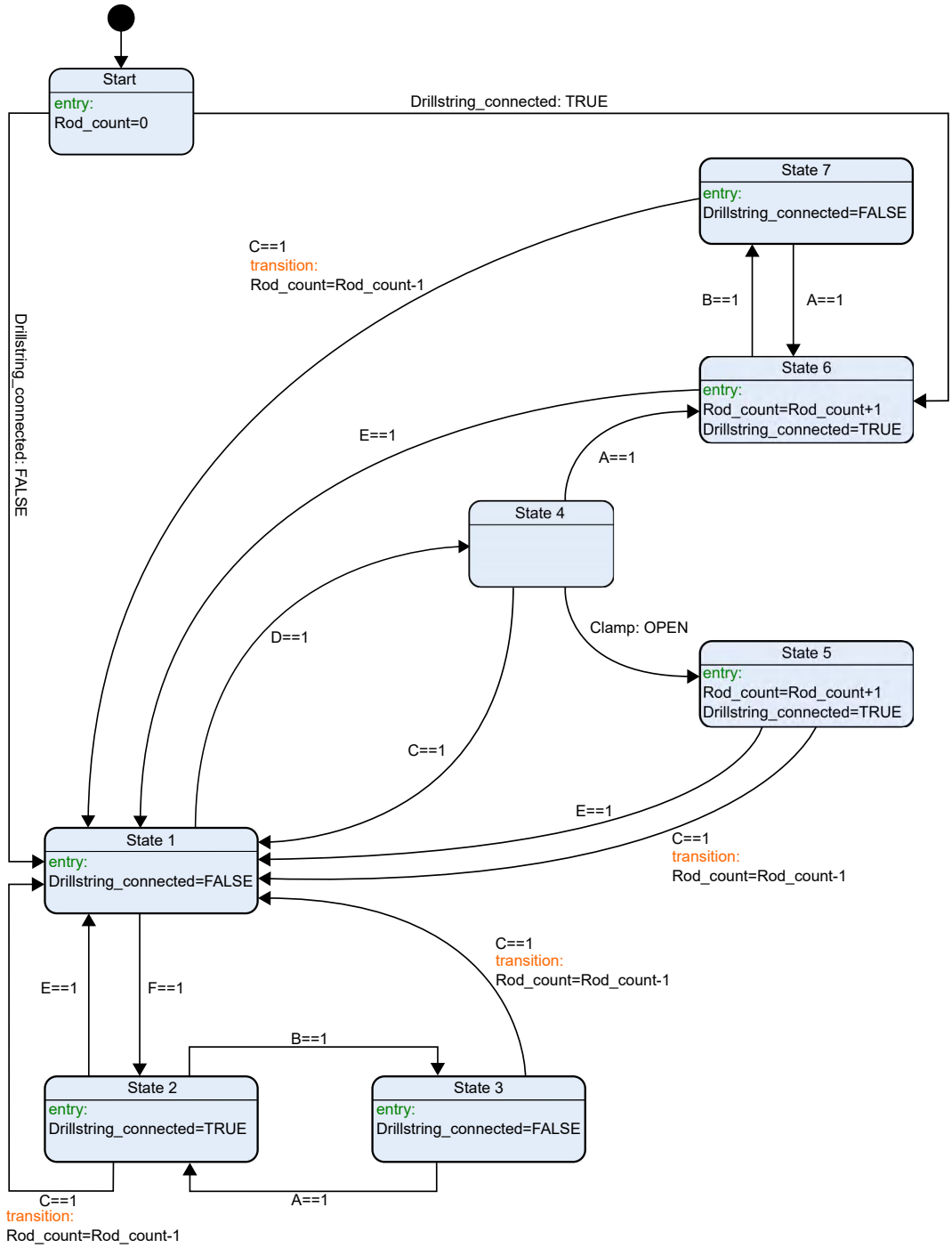

Figure A.4: State machine to identify when the main drill string is connected to the rotary head.

TRUE.

State		Transition		
Name	Action	**Condition**	**Action**	**Next State**
Start	Rod_count	Drillstring_connected==FALSE	-	State 1
		Drillstring_connected==TRUE	-	State 6
State 1	Drillstring_connected=FALSE	F==1	-	State 2
		D==1	-	State 4
State 2	Drillstring_connected=TRUE	C==1	Rod_count=Rod_count-1	State 1
		B==1	-	State 3
		E==1	-	State 1
State 3	Drillstring_connected=FALSE	C==1	Rod_count=Rod_count-1	State 1
		A==1	-	State 2
State 4	-	C==1		State 1
		Clamp==OPEN	-	State 5
		A==1	-	State 6
State 5	Rod_count=Rod_count+1, Drillstring_connected=TRUE	C==1	Rod_count=Rod_count-1	State 1
		E==1	-	State 1
State 6	Rod_count=Rod_count+1, Drillstring_connected=TRUE	E==1	-	State 1
		B==1	-	State 7
State 7	Drillstring_connected=FALSE	C==1	Rod_count=Rod_count-1	State 1
		A==1	-	State 6

Table A.7: Description of the state diagram from Figure A.4.

Once the drill string becomes connected to the rotary head, the parameters bit depth and hole depth are estimated as shown in Algorithm 1.

Algorithm 1: Compute bit and hole depths.

input variables : Head_Position, Drillstring_connected
output variables: Bit_Depth, Hole_Depth

```
begin
    (Step 1.) Initialize variables Bit_Depth and Hole_Depth.
    while (Drillstring_connected == TRUE) do
        (Step 2.) Update variable Bit_Depth.
        Bit_Depth = Bit_Depth + Head_Position;
        (Step 3.) Check if it is drilling.
        if (Bit_Depth > Hole_Depth ) then
            (Step 4.) Update variable Hole_Depth.
            Hole_Depth = Bit_Depth;
        else
            (Not Drilling);
        end if
    end while
end
```

Figure A.5 presents the final results of the algorithms explained in this section. It is then possible to identify when the drill bit is approaching the borehole bottom and when the drilling process is occurring. The parameter rate of penetration (ROP) can also be estimated.

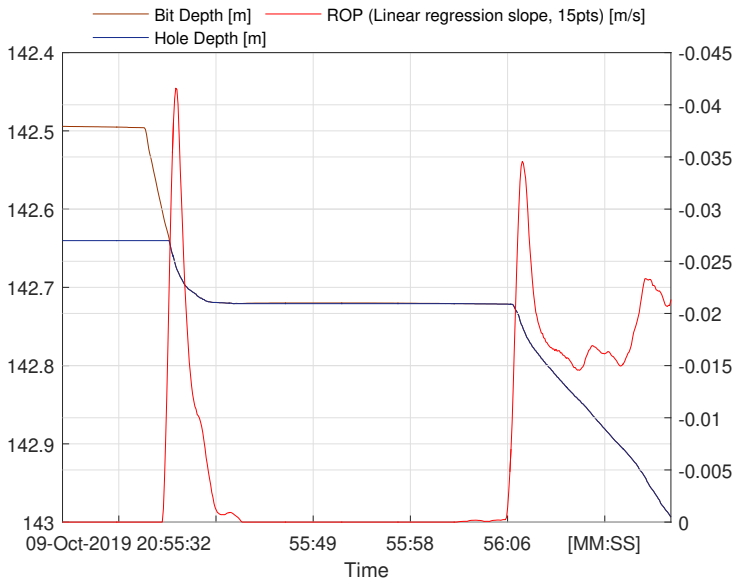

Figure A.5: Output parameters bit depth, hole depth, and rate of penetration.

Appendix B

Algorithms to Estimate Torque-on-Bit and Weight-on-Bit

This section presents the algorithms developed to estimate the torque and weight applied to the drill bit.

B.0.1 Computation of TOB and WOB Parameters

The output thrust and torque generated at the surface (see Section 3.2.1) are recorded as reference parameters, immediately after a new rod is added to the drill string and the rotary head starts moving downwards with the drill string rotating (before touching the bottom of the hole). The idea is to use these references to estimate the weight and torque applied to the bit while drilling. This task is accomplished with the state machine shown in Figure B.1, represented by Table B.1.

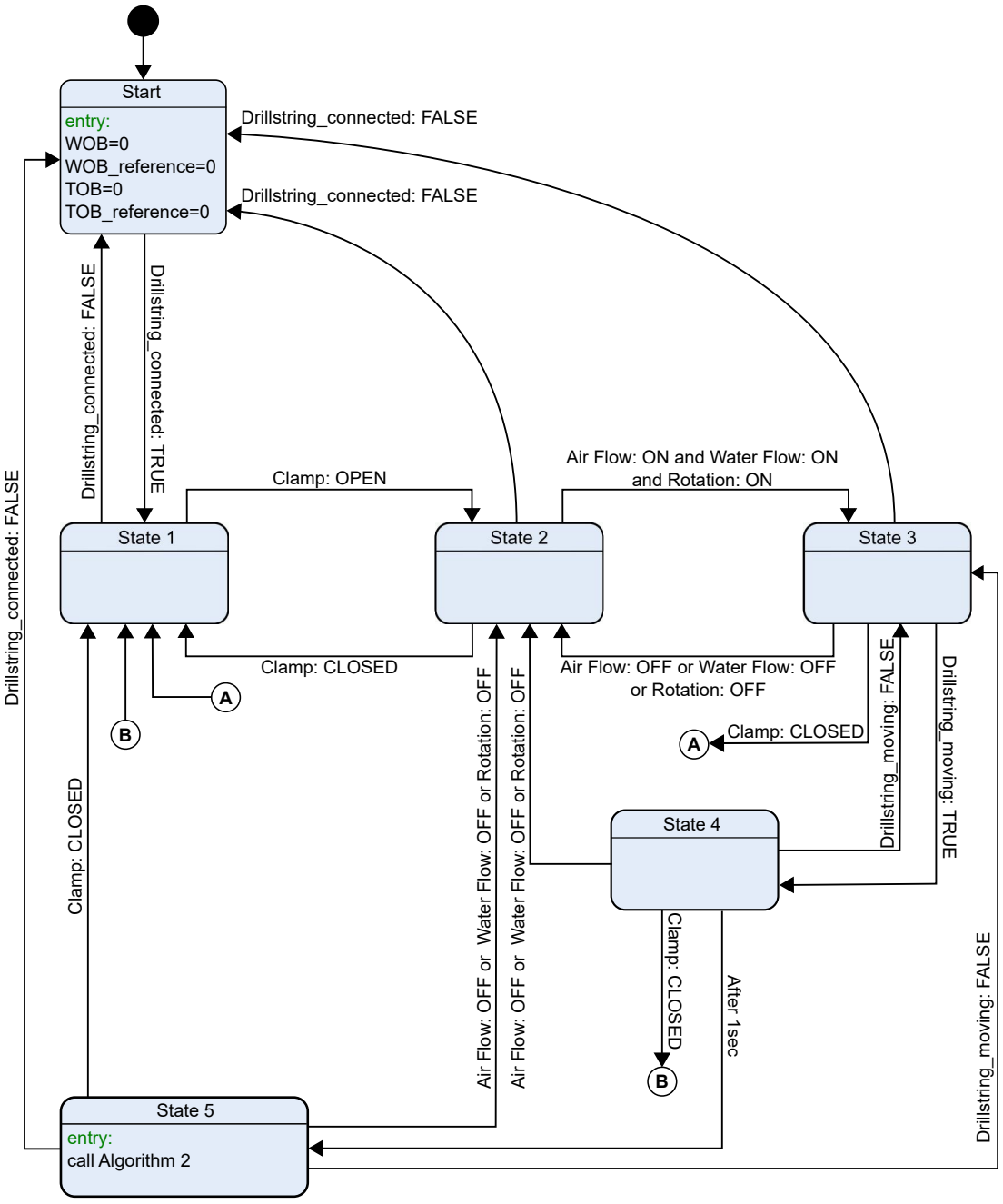

Figure B.1: State machine to ensure that the algorithm (used to record the reference parameters) is called when the drilling rig is in its dynamic state.

State		Transition		
Name	Action	**Condition**	**Action**	**Next State**
Start	Reset Variables	Drillstring_connected==TRUE	-	State 1
State 1	-	Drillstring_connected==FALSE	-	Start
		Clamp==OPEN	-	State 2
State 2	-	Drillstring_connected==FALSE	-	Start
		Clamp==CLOSED	-	State 1
		Comparison 1	-	State 3
State 3	-	Drillstring_connected==FALSE	-	Start
		Clamp==CLOSED	-	State 1
		Comparison 2	-	State 2
		Drillstring_moving==TRUE	-	State 4
State 4	-	Clamp==CLOSED	-	State 1
		Comparison 2	-	State 2
		Drillstring_moving==FALSE	-	State 3
		After 1 sec	-	State 5
State 5	call Algorithm 2	Drillstring_connected==FALSE	-	Start
		Clamp==CLOSED	-	State 1
		Comparison 2	-	State 2
		Drillstring_moving==FALSE	-	State 3

Reset Variables: WOB=0, WOB_reference=0, TOB=0, TOB_reference=0;
Comparison 1: Air Flow==ON AND Water Flow==ON AND Rotation==ON;
Comparison 2: Air Flow==OFF OR Water Flow==OFF OR Rotation==OFF.

Table B.1: Description of the state diagram from Figure B.1.

Once the **State 5** is reached, the parameters weight and torque applied to the bit are estimated as shown in Algorithm 2. Note that the **State 5** remains active as long as **(1)** the drill string is moving and **(2)** the parameters air flow, water flow, and rotation are turned on. This ensures that the drilling rig is in its dynamic state when the references are recorded as well as while the weight and torque on the bit are being monitored (refer to Figure B.1 and Table B.1).

Algorithm 2: Compute WOB and TOB.

```
input variables  : Thrust (surface), Torque (surface), Bit_Depth,
                   Hole_Depth
output variables: WOB, TOB
begin
    while (State 5 == Active) do
        (Step 1.) Check if the bit is off-bottom.
        if (Bit_Depth < (Hole_Depth - 0.5 (off-bottom region)) ) then
            if (WOB_reference < Thrust) then
                (Step 2.) Update variable WOB_reference.
                WOB_reference = Thrust;
            end if
            if (TOB_reference < Torque) then
                (Step 3.) Update variable TOB_reference.
                TOB_reference = Torque;
            end if
        else
            (Step 4.) Estimate the weight and torque applied to the bit
             while the bit is within the drilling region.
            WOB = WOB_reference - Thrust;
            TOB =TOB_reference - Torque;
        end if
    end while
end
```

The output result from Algorithm 2 is the weight and torque applied to the drill bit. Figure B.2 illustrates the main steps to estimate such parameters:

1. After adding a new rod to the main drill string, the drill operator releases the clamp and, therefore, the rotary head becomes ready to move (downwards).

2. The rotary head starts moving and the **State 5** is reached (from the state

machine shown in Figure B.1). Then, weight and torque are recorded as reference parameters (before the drill bit touches the bottom of the hole).

3. Finally, the weight and torque applied to the bit are estimated once the on-bottom region is reached.

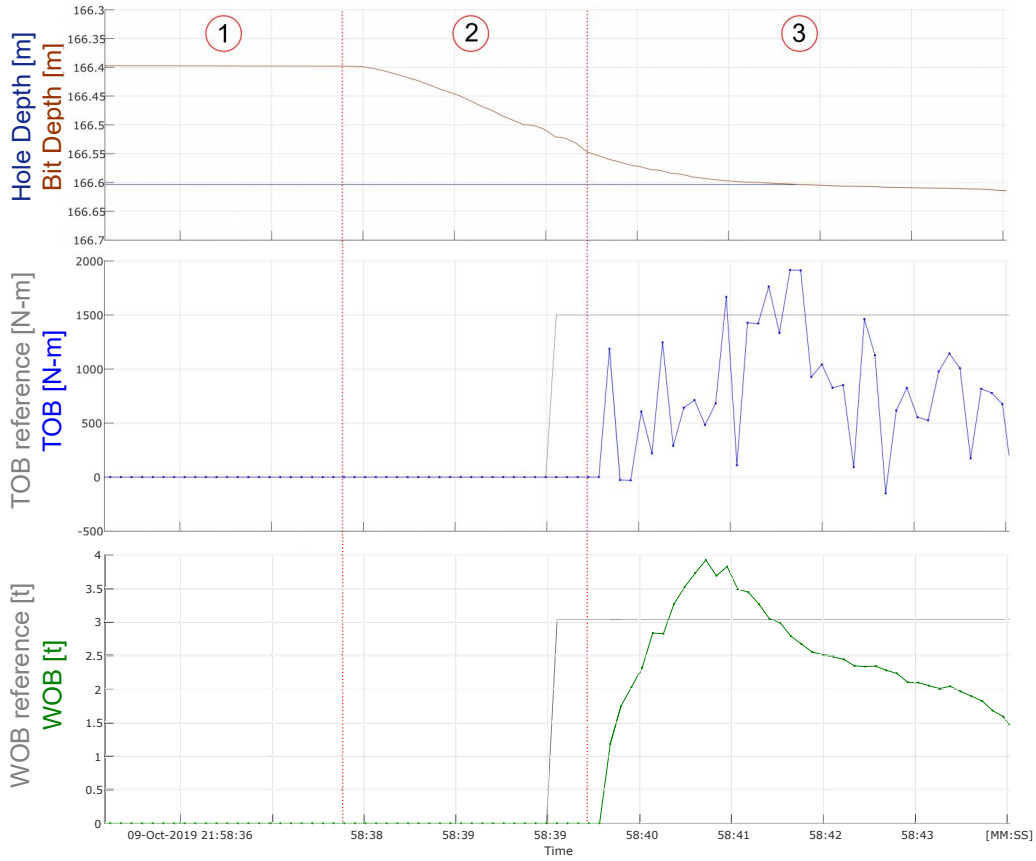

Figure B.2: Weight and torque applied to the bit.

Appendix C

Hammer Frequency and Penetration-per-Impact Estimation

This section presents my proposed method to estimate hammer frequency and penetration per impact in real time. The algorithm for the method executes the following procedures at each iteration:

- Define and process the input vector (from the draw wire sensor signal).
- Perform time-frequency analysis on the input vector.
- Identify whether the hammer system has become active.
- Estimate the piston impact frequency and compute the drill bit penetration (after each piston impact).

C.0.1 Filtering the high-resolution data

The first step is to filter out unwanted content from the input data using one of the two major types of digital filters: either **(1)** Infinite Impulse Response (IIR) or **(2)** Finite Impulse Response (FIR) filter. FIR filters are more suitable for our

application because the input signal is not stationary, and FIR filters are always stable and can implement linear-phase filtering—meaning that all frequencies are shifted equally in time, maintaining their relative harmonic relationships. It is important to mention that IIR filters require less computation speed and memory, but the cRIO-9056 data acquisition system (refer to Figure 3.6) used during the field tests has the hardware requirement to run applications in real time.

Equation C.1 describes the relationship between input and output of an FIR filter:

$$y[n] = \sum_{k=0}^{J} b[k]x[n-k] \tag{C.1}$$

where J is the order of the FIR filter and $b[k]$ are the filter coefficients (filter's impulse response). A bandpass FIR filter was designed with 501 coefficients to attenuate frequency content below 10 Hz and above 100 Hz. This range was specified since most down-the-hole hammer systems used in the mining industry operate in this range. Figure C.1 shows the filter's impulse response (filter's coefficients) and the filter's kernel.

C.0.2 Input Signal for the Algorithm

It was defined that for each iteration of the algorithm, a three-second equivalent vector of input data (from the draw wire sensor) would be selected and processed, as illustrated in Figure C.2. Moreover, it was stipulated that there will always be an overlap of two seconds between the input vectors of each algorithm's iteration (between iterations i and $i+1$).

The designed FIR filter (refer to Figure C.1) is convolved with the three-second-equivalent input vector to filter out the unwanted frequency content. The filter with 501 coefficients ($J=501$) enters completely in the *steady state* regime only after processing through the first J input samples. Before that, the output might have erratic behaviour. Therefore, after filtering the input data, the middle

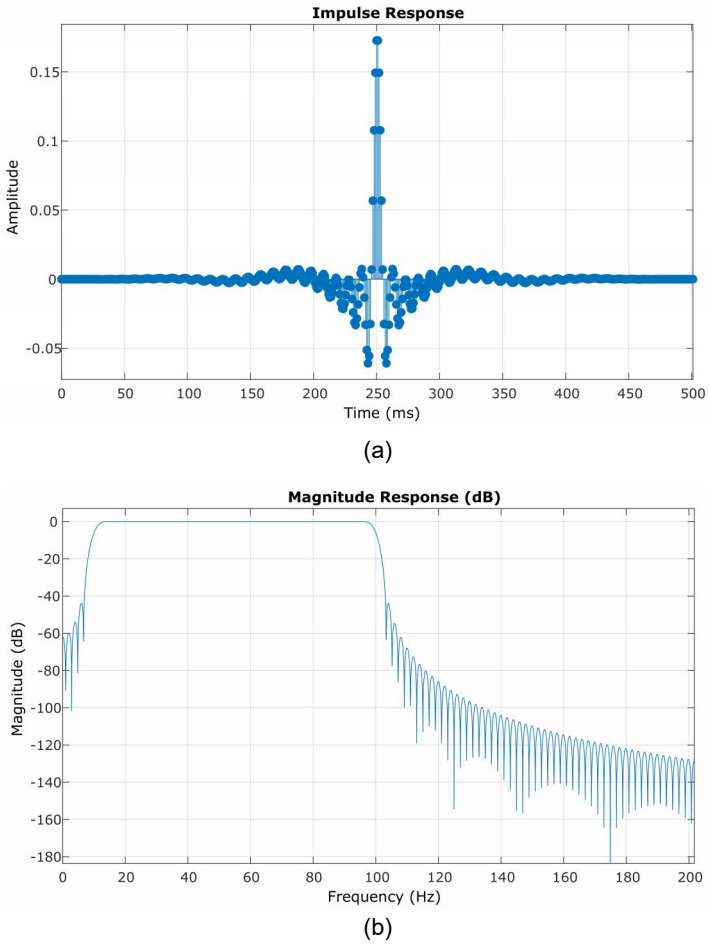

Figure C.1: Bandpass FIR filter to attenuate frequencies below 10 Hz and above 100 Hz: (a) impulse response and (b) filter kernel in the frequency domain.

part of the input vector is selected to ensure that only the correctly filtered data will be considered for the algorithm's next steps. This is illustrated in Figure C.3.

C.0.3 Time-frequency Analysis

Since the draw wire sensor signal has non-stationary, non-periodic characteristics and fast transient features (i.e., high-frequency content for a short duration), complex Morlet wavelets were used for the time-frequency analysis. Figure C.4 shows an example where the hammer dominant frequency varies over time from on-bottom with (i) the hammer not activated (dominant frequency equal to zero),

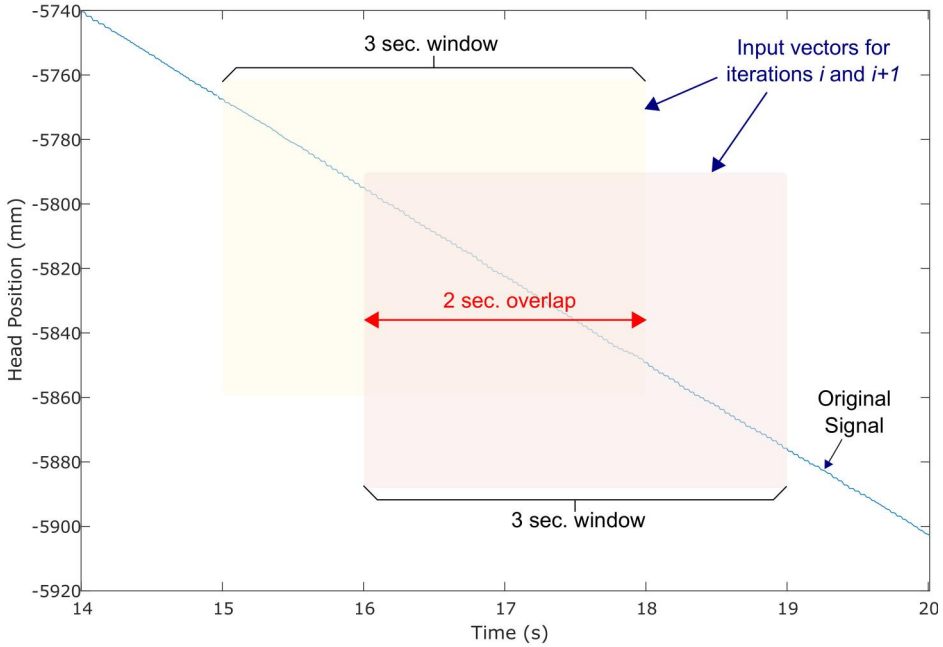

Figure C.2: Overlap of two seconds between the input vectors of iterations i and $i+1$.

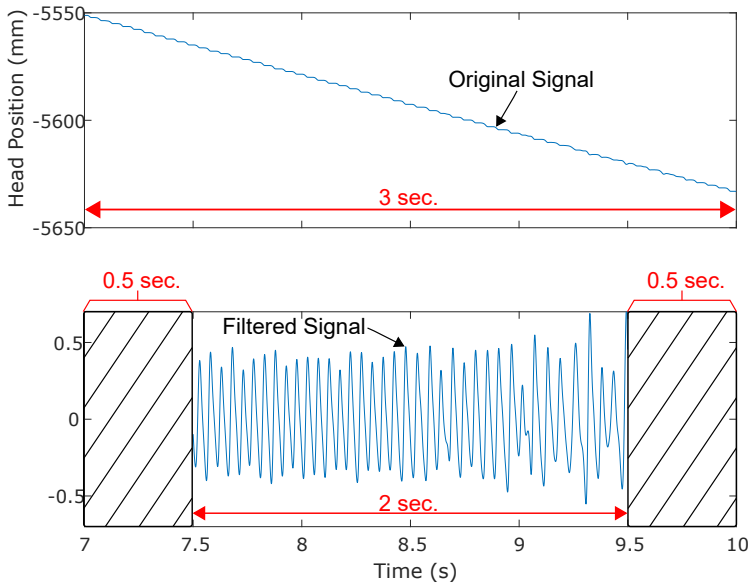

Figure C.3: Original input signal and filtered signal.

to (ii) on-bottom with the hammer activated and, then, (iii) varying as drilling conditions change.

Time-frequency analysis with complex Morlet wavelets allows the possibility to identify with high precision the moment when the hammer system becomes

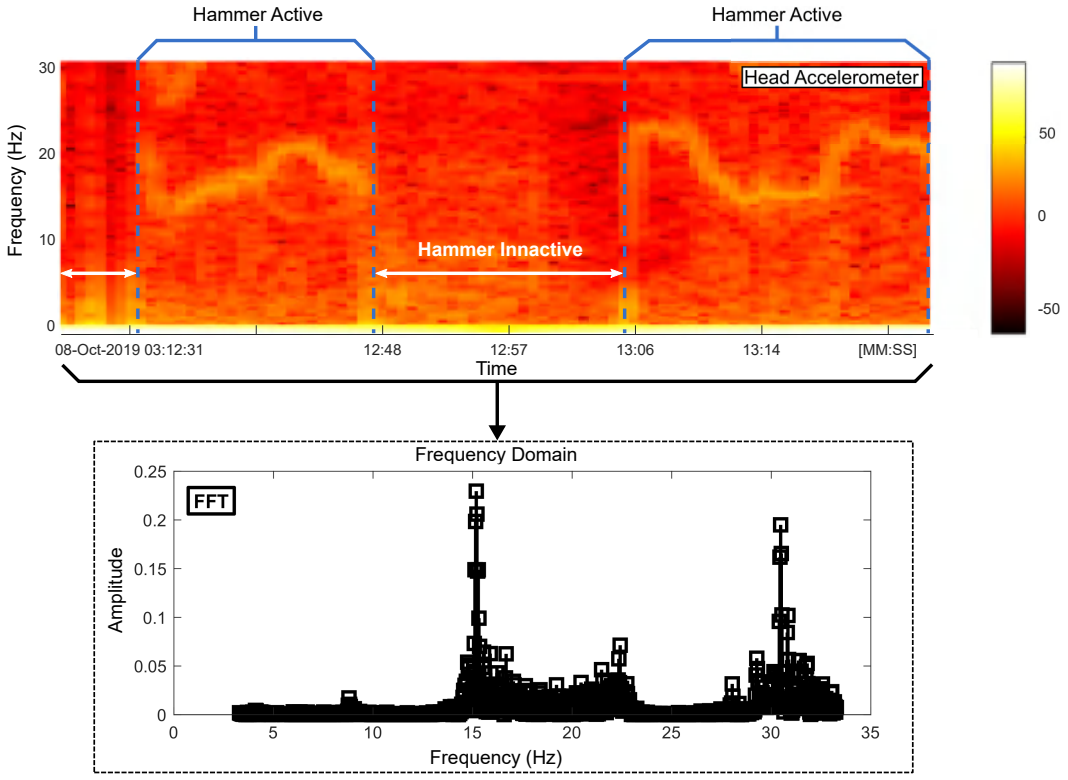

Figure C.4: Power spectrum of the data pertaining to the accelerometer mounted on the rotary head that illustrates a variation in the dominant frequency with time. The result of the FFT carried out on the entire time window shows a strong first harmonic (at 16 Hz) and also a strong second harmonic (at around 32 Hz).

active and how its dominant frequency changes, as a variation may reflect a change at the bit-rock interface. Figure C.5 shows a complex Morlet wavelet in the time domain, which can be defined as a complex sine wave (of frequency f) tapered by a Gaussian function. Note that in the frequency domain, it has exactly the shape of a Gaussian function that peaks at the frequency of the sine wave used to generate the Morlet wavelet. Due to the fact that the Gaussian-shaped signal (in the frequency domain) has no sharp edges, this reduces ripple effects that could be wrongly interpreted as oscillations (when it is convolved with another signal).

In each iteration of the algorithm, the two-second input time series (refer to Figure C.3) is convolved with several complex Morlet wavelets that have different frequencies to generate the time-frequency matrix M_{PW} (shown in Equation C.2). Since the expected piston impact frequencies range between 10 and 100 Hz, the

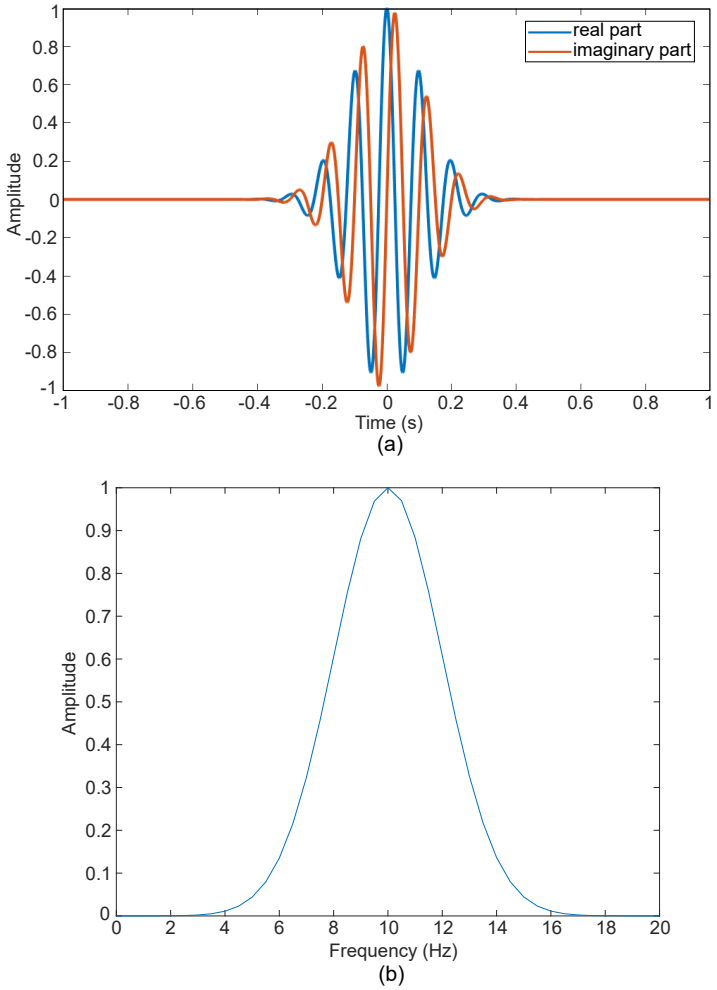

Figure C.5: 10 Hz complex Morlet wavelet: (a) real and imaginary parts of the wavelet in the time domain and (b) power spectrum of the wavelet in the frequency domain.

time-frequency analysis will consider 50 linearly spaced frequencies between this range. Therefore, the dimension of the matrix M_{PW} will be equal to 50 lines that correspond to the amount of wavelets with different frequencies, and 2058 columns that correspond to the length of the two-second time series input.

The result, of each convolution between the same input signal with each complex Morlet wavelet, is a complex-valued signal from which the instantaneous phase and power are extracted. Each line of matrix M_{PW} corresponds to the estimated power of the convolution between the input signal and one of the wavelets.

A visual representation of Matrix M_{PW} (Equation C.2) is shown in Figure

C.6.

$$[M_{PW}]_{n\times m} = \begin{bmatrix} a_{11} & a_{12} & a_{13} & a_{14} & \dots & a_{1m} \\ a_{21} & a_{22} & a_{23} & a_{24} & \dots & a_{2m} \\ a_{31} & a_{32} & a_{33} & a_{34} & \dots & a_{3m} \\ \vdots & \vdots & \vdots & \vdots & \vdots & \vdots \\ a_{n1} & a_{n2} & a_{n3} & a_{n4} & \dots & a_{nm} \end{bmatrix}_{50\times 2048} \tag{C.2}$$

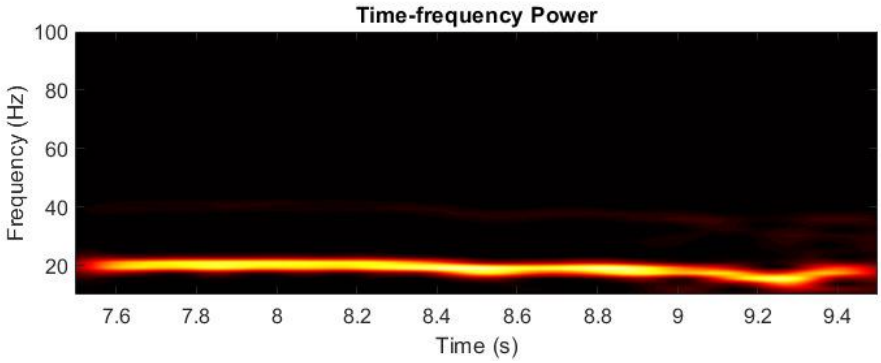

Figure C.6: Visual representation example of Matrix M_{PW} (from Equation C.2).

C.0.4 Hammer Activation Indicator

Considering the time-frequency matrix M_{PW}, a row vector containing the variances corresponding to each of its columns is generated with Equation C.3:

$$\sigma^2 = \frac{\sum_{i=1}^{n}(x_i - \bar{x})^2}{n} \tag{C.3}$$

where x_i is the i^{th} data point in column m, $\bar{x}$ is the mean of all data points in column m, and n is the number of data points in column m.

Tests have shown that the variance vector gives us a good indication of whether the down-the-hole hammer system is activated or not. An example is shown in Figure C.7, where the variance vector is plotted together with the draw wire sensor signal (head position) and matrix M_{PW}.

Noticeably, the variance becomes considerably high whenever the hammer sys-

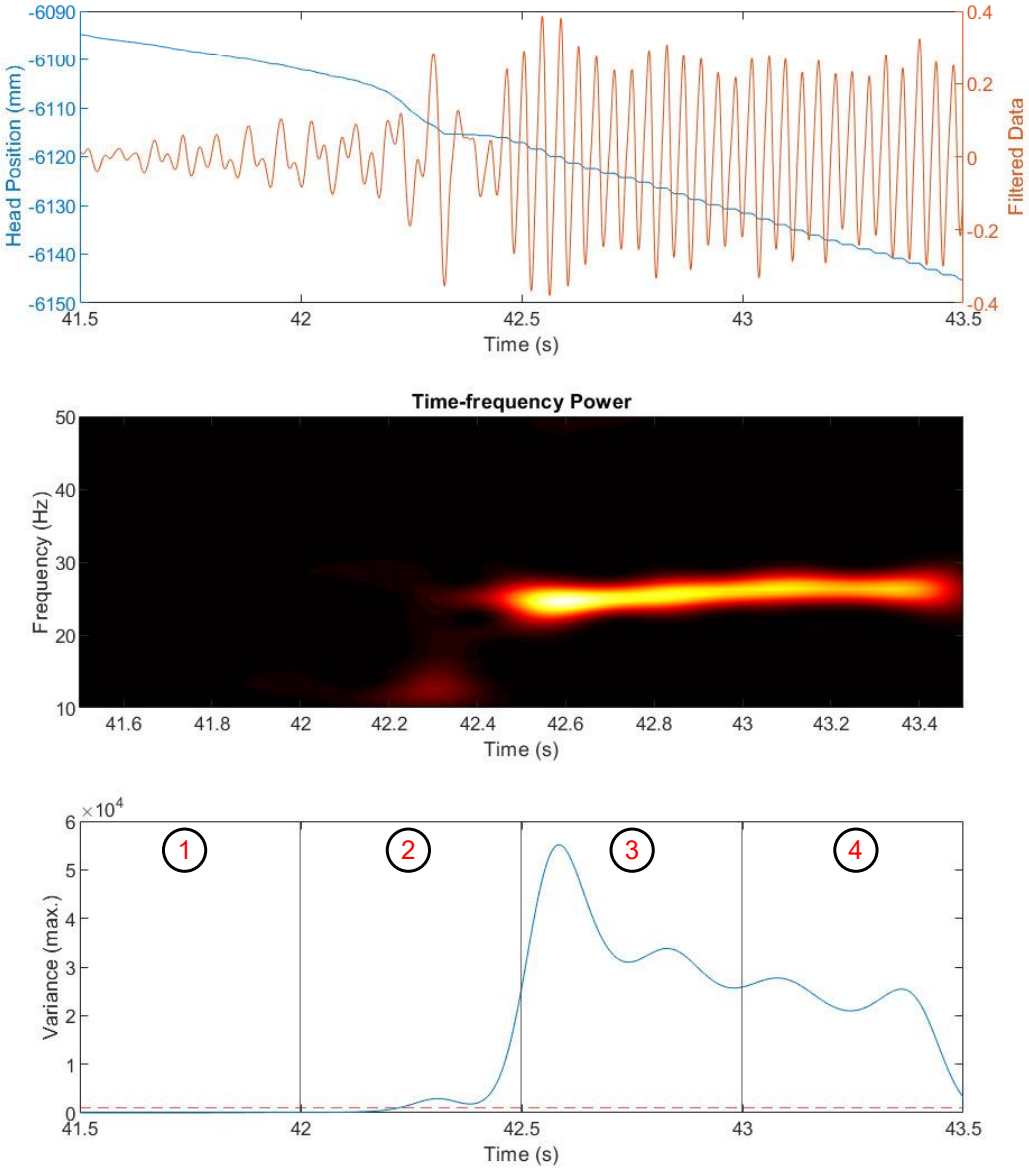

Figure C.7: Hammer activation indicator.

tem is activated. Therefore, it was defined (in the algorithm) a variance threshold of $\sigma^2 = 1000$ to identify the moment when the hammer system becomes active[1]. After a thorough analysis, excellent results using this value were obtained. Note that in Figure C.7 the two-second window is subdivided into four equally spaced intervals, and within each of these intervals it is assumed that the hammer is

[1]A considerable amount of tests were performed considering a variance threshold of $\sigma^2 = 1000$ and excellent results were obtained. This parameter defines the indicator's sensitivity and can be changed.

active only if the threshold $\sigma^2 = 1000$ is surpassed.

C.0.5 Hammer Frequency and Penetration per Impact

The clear periodic step response of the draw wire sensor signal allows the estimation of the depth difference between two successive piston impacts (while it is active). Thus, it is possible to estimate the drill bit penetration after each piston impact, as shown in Figure C.8.

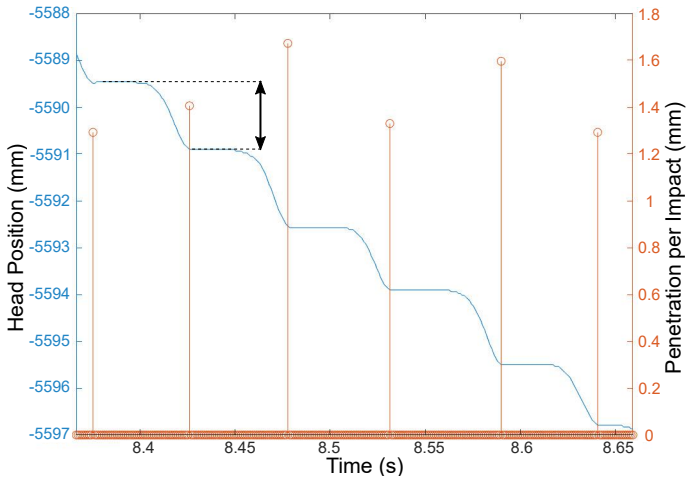

Figure C.8: Recording of the draw wire position sensor while drilling on-bottom over a period of about 0.3 seconds that shows a periodic step response. From these measurements, the parameters bit penetration per single impact and piston impact frequency can be estimated.

Finally, the hammer frequency f is estimated with Equation C.4:

$$f = \frac{n_i}{t} \tag{C.4}$$

where n_i is the number of impacts when the hammer is active and t is the time window interval ($t = 2seconds$).

Algorithm 3 presents the complete structure of the algorithm and its output result is shown in Figure C.9.

Algorithm 3: Compute hammer frequency and penetration per impact.

input variables : Head_Position, Bit_Depth, Hole_Depth
output variables: Hammer Frequency, Penetration per Impact

begin
- (Step 1.) Initialize variables and load filter coefficients (FIR bandpass);
- (Step 2.) Define the filter kernel in the frequency domain;
- (Step 3.) Generate complex Morlet Wavelets with different frequencies (from 10 Hz up to 100 Hz);
- (Step 4.) Check if the drill bit is close to the bottom hole region.
- **while** (*Bit_Depth* > *Hole_Depth - 0.5*) **do**
  - (Step 5.) Specify the input vector (3 sec. time window).
  - (Step 6.) Fast convolution of the input vector with the filter kernel to remove unwanted frequencies (Frequency domain).
  - (Step 7.) Select only 2 seconds equivalent of data (to remove filter transient time and delay).
  - (Step 8.) Perform convolution of the filtered data with each complex wavelet (frequency domain).
  - (Step 9.) Reconstruct the signal in the time domain.
  - (Step 10.) Construct the time-frequency matrix.
  - (Step 11.) Check if the hammer is activated.
  - **if** (*Hammer==Active*) **then**
    - (Step 12.) Compute penetration per single impact.
    - (Step 13.) Estimate the hammer frequency.
  - **end if**
- **end while**

end

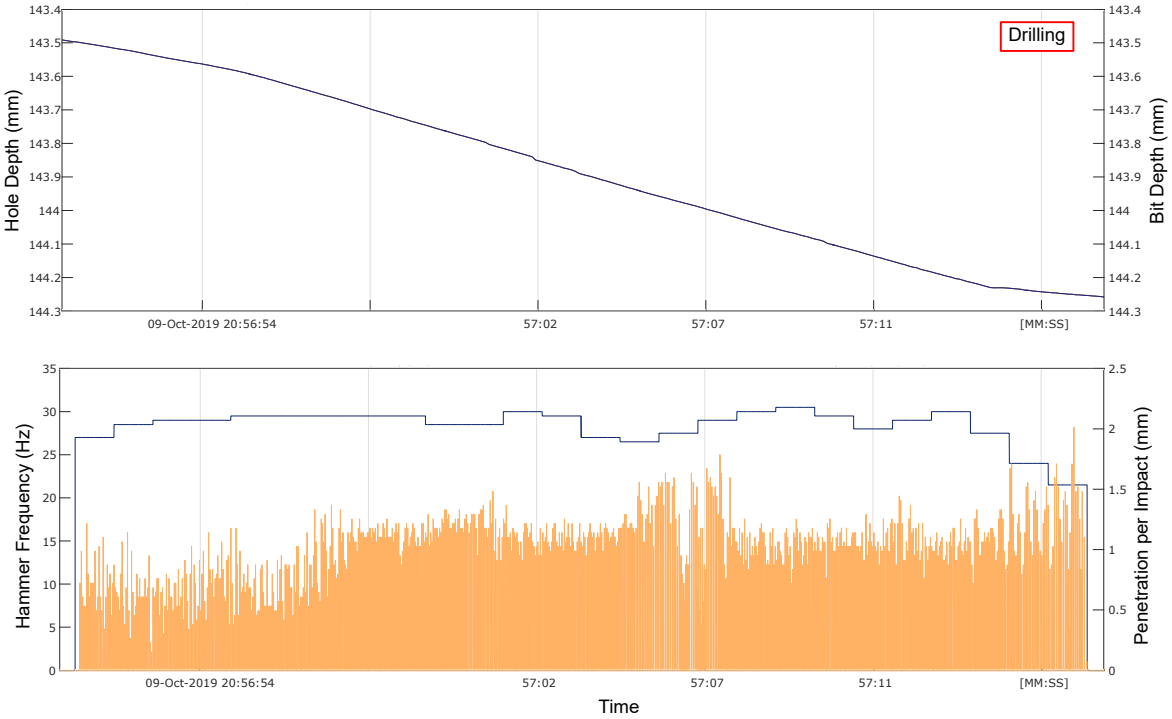

Figure C.9: Hammer frequency and penetration per impact output parameters.

Bibliography

M. Amjad (1996). *Control of ITH percussive longhole drilling in hard rock*. Ph.d.

Autodesk (2023). 'Fusion 360 (version v.2.0.16985)'.

M. V. Barr (1985). *Instrumented horizontal drilling for tunnelling site investigation*. Ph.D. thesis, University of London.

J. Caers, et al. (2022). 'Efficacy of Information in Mineral Exploration Drilling'. *Natural Resources Research* pp. 1–17.

P. Cao, et al. (2018). 'Optimal design of novel drill bit to control dust in down-the-hole hammer reverse circulation drilling'. *Arabian Journal for Science and Engineering* **43**(3):1313–1324.

W. Changming (1991). 'An analytical study of percussive energy transfer in hydraulic rock drills'. *Mining Science and Technology* **13**(1):57–68.

W. Cheetham & E. Inett (1953). 'Factors affecting the performance of percussive drills'. *Transactions of the Institution of Mining and Metallurgical Engineers* **63**:45–74.

L. Chiang & D. Elıas (2000). 'Modeling impact in down-the-hole rock drilling'. *International Journal of Rock Mechanics and Mining Sciences* **37**(4):599–613.

L. Chiang & E. Stamm (1998). 'Design optimization of valveless DTH pneumatic hammers by a weighted pseudo-gradient search method' .

L. E. Chiang & D. A. Elías (2008). 'A 3D FEM methodology for simulating the impact in rock-drilling hammers'. *International Journal of Rock Mechanics and Mining Sciences* **45**(5):701–711.

A. Depouhon, et al. (2013). 'A drifting impact oscillator with periodic impulsive loading: Application to percussive drilling'. *Physica D: Nonlinear Phenomena* **258**:1–10.

A. F. Depouhon (2014). *Integrated dynamical models of down-the-hole percussive drilling*. Ph.d.

P. Dutta (1968). 'The determination of stress waveforms produced by percussive drill pistons of various geometrical designs'. In *International Journal of Rock Mechanics and Mining Sciences & Geomechanics Abstracts*, vol. 5, pp. 501–510. Elsevier.

EPSLOG (2023). 'DREAM (version 2021.05)'.

H. Fischer (1959). 'On longitudinal impact I'. *Applied Scientific Research, Section A* **8**(1):105–139.

M. Fourmeau, et al. (2015). 'Influence of indexation and impact energy on bit/rock interface law in percussive drilling: an experimental study'. In *49th US Rock Mechanics/Geomechanics Symposium*. OnePetro.

R. Ghosh, et al. (2017). 'Monitoring of Drill System Behavior for Water-Powered In-The-Hole (ITH) Drilling'. *Minerals* **7**(7).

W. Goldsmith (2001). *Impact*. Courier Corporation.

K. F. Graff (2012). *Wave motion in elastic solids*. Courier Corporation.

B. Haimson (1965). *High Velocity, Low Velocity and Static Bit Penetration Chracteristics in Tennessee Marble*. Ph.D. thesis, University of Minnesota.

W. Hustrulid (1971). 'The percussive drilling of quartzite'. *Journal of the Southern African Institute of Mining and Metallurgy* **71**(12):245–268.

W. Hustrulid & C. Fairhurst (1971a). 'A theoretical and experimental study of the percussive drilling of rock Part II—force-penetration and specific energy determinations'. In *International Journal of Rock Mechanics and Mining Sciences & Geomechanics Abstracts*, vol. 8, pp. 335–356. Elsevier.

W. Hustrulid & C. Fairhurst (1972a). 'A theoretical and experimental study of the percussive drilling of rock part III—experimental verification of the mathematical theory'. In *International Journal of Rock Mechanics and Mining Sciences & Geomechanics Abstracts*, vol. 9, pp. 417–418. Elsevier.

W. Hustrulid & C. Fairhurst (1972b). 'A theoretical and experimental study of the percussive drilling of rock Part IV—application of the model to actual percussion drilling'. In *International Journal of Rock Mechanics and Mining Sciences & Geomechanics Abstracts*, vol. 9, pp. 431–442. Elsevier.

W. A. Hustrulid (1965). *A study of energy transfer to rock and prediction of drilling rates in percussive drilling*. University of Minnesota.

W. A. Hustrulid & C. Fairhurst (1971b). 'A theoretical and experimental study of the percussive drilling of rock part I—theory of percussive drilling'. In *International Journal of Rock Mechanics and Mining Sciences & Geomechanics Abstracts*, vol. 8, pp. 311–333. Elsevier.

M. R. Islam & M. E. Hossain (2020). *Drilling Engineering: Towards Achieving Total Sustainability*. Gulf Professional Publishing.

R. Karimi Bakhshandi, et al. (2022). 'Failure analysis of two cylindrical impact pistons subjected to high velocity impacts in drilling applications'. *Engineering Failure Analysis* **140**.

L. G. Karlsson, et al. (1989). 'Experimental study of a percussive process for rock fragmentation'. In *International Journal of Rock Mechanics and Mining Sciences & Geomechanics Abstracts*, vol. 26, pp. 45–50. Elsevier.

D.-J. Kim, et al. (2020). 'Prediction model of drilling performance for percussive rock drilling tool'. *Advances in Civil Engineering* **2020**.

D.-J. Kim, et al. (2019). 'Design study of impact performance of a DTH hammer using PQRSM and numerical simulation'. *Journal of Mechanical Science and Technology* **33**(11):5589–5602.

S. B. Kivade, et al. (2015). 'Experimental Investigations on Penetration Rate of Percussive Drill'. *Procedia Earth and Planetary Science* **11**:89–99.

LabVIEW (2023). 'LabVIEW (version LV2019)'.

X. Li, et al. (2000). 'Analysis of impact hammer rebound to estimate rock drillability'. *Rock Mechanics and Rock Engineering* **33**(1):1–13.

Y. Li, et al. (2021). 'Hard Rock Fragmentation in Percussion Drilling Considering Confining Pressure: Insights from an Experimental Study'. *International Journal of Rock Mechanics and Mining Sciences* **148**.

H. Liu, et al. (2008). 'Numerical studies on bit-rock fragmentation mechanisms'. *International Journal of Geomechanics* **8**(1):45–67.

B. Lundberg (1973a). 'Energy transfer in percussive rock destruction—I: Comparison of percussive methods'. In *International Journal of Rock Mechanics and Mining Sciences & Geomechanics Abstracts*, vol. 10, pp. 381–399. Elsevier.

B. Lundberg (1973b). 'Energy transfer in percussive rock destruction—II: supplement on hammer drilling'. In *International Journal of Rock Mechanics and Mining Sciences & Geomechanics Abstracts*, vol. 10, pp. 401–419. Elsevier.

B. Lundberg (1982). 'Microcomputer simulation of stress wave energy transfer to rock in percussive drilling'. In *International Journal of Rock Mechanics and Mining Sciences & Geomechanics Abstracts*, vol. 19, pp. 229–239. Elsevier.

B. Lundberg (1985). 'Microcomputer simulation of percussive drilling'. In *International Journal of Rock Mechanics and Mining Sciences & Geomechanics Abstracts*, vol. 22, pp. 237–249. Elsevier.

B. Lundberg & P. Collet (2010). 'Optimal wave with respect to efficiency in percussive drilling with integral drill steel'. *International Journal of Impact Engineering* **37**(8):901–906.

B. Lundberg & P. Collet (2015). 'Optimal wave shape with respect to efficiency in percussive drilling with detachable drill bit'. *International Journal of Impact Engineering* **86**:179–187.

B. Lundberg & J. Huo (2017). 'Biconvex versus bilinear force-penetration relationship in percussive drilling of rock'. *International journal of impact engineering* **100**:7–12.

B. Lundberg & M. Okrouhlik (2001). 'Influence of 3D effects on the efficiency of percussive rock drilling'. *International Journal of Impact Engineering* **25**(4):345–360.

B. Lundberg & M. Okrouhlik (2006). 'Efficiency of a percussive rock drilling process with consideration of wave energy radiation into the rock'. *International Journal of Impact Engineering* **32**(10):1573–1583.

R. G. Lundquist (1968). *Rock drilling characteristics of hemispherical insert bits*. Ph.d.

Y. Luo, et al. (2016). 'Development of a specially designed drill bit for down-the-hole air hammer to reduce dust production in the drilling process'. *Journal of Cleaner Production* **112**:1040–1048.

W. C. Lyons (2000). *Air and gas drilling manual*. McGraw Hill Professional.

R. W. Marjoribanks (1997). *Mineral Exploration Drilling*, pp. 39–69. Springer Netherlands, Dordrecht.

MathWorks (2023). 'MATLAB (version R2021b)'.

MinEx (2018). 'Mineral and Exploration (MinEx) CRC'.

L. Mishnaevsky (1995). 'Physical mechanisms of hard rock fragmentation under mechanical loading: a review'. *INTERNATIONAL JOURNAL OF ROCK MECHANICS AND MINING & GEOMECHANICS ABSTRACTS* **32**(8).

S. Pang, et al. (1989). 'A force-indentation model for brittle rocks'. *Rock mechanics and rock engineering* **22**(2):127–148.

J. P. Peck (1989). *Performance monitoring of rotary blasthole drills*. Ph.D. thesis, McGill University.

T. Saksala (2011). 'Numerical modelling of bit–rock fracture mechanisms in percussive drilling with a continuum approach'. *International Journal for Numerical and Analytical Methods in Geomechanics* **35**(13):1483–1505.

T. Saksala (2013). '3D numerical modelling of bit–rock fracture mechanisms in percussive drilling with a multiple-button bit'. *International Journal for Numerical and Analytical Methods in Geomechanics* **37**(3):309–324.

T. Saksala, et al. (2014). 'Numerical and experimental study of percussive drilling with a triple-button bit on Kuru granite'. *International Journal of Impact Engineering* **72**:56–66.

H. Schunnesson (1998). 'Rock characterisation using percussive drilling'. *International journal of rock mechanics and mining sciences* **35**(6):711–725.

S. Shaw (1965). 'Effects of farying degrees of rotation on rate of penetration of percussion drill bits'. *Unpublished Report* .

Q. Shen, et al. (2022). 'Efficiency evaluation of a percussive drill rig using rate-energy ratio based on rock drilling tests'. *Journal of Petroleum Science and Engineering* **217**.

R. Simon (1963). 'Digital machine computations of the stress waves produced by striker impacts in percussion drilling machines'. In *Rock mechanics*, p. 137. Pergamon Press Oxford.

R. Simon (1964). 'Transfer of the stress wave energy in the drill steel of a percussive drill to the rock'. In *International Journal of Rock Mechanics and Mining Sciences & Geomechanics Abstracts*, vol. 1, pp. 397–411. Elsevier.

C. Song, et al. (2018). 'Optimal Design Parameters of a Percussive Drilling System for Efficiency Improvement'. *Advances in Materials Science and Engineering* **2018**:1–13.

X. Song (2020). *Study of An Optimal Weight-on-Bit in Percussive Drilling*. Ph.d.

X. Song, et al. (2019a). 'A Phenomenological Model of Percussive Drilling: Review of Experimental Evidence'. In *ARMA-CUPB Geothermal International Conference*. OnePetro.

X. Song, et al. (2021). 'Influence of weight-on-bit on percussive drilling performance'. *Rock Mechanics and Rock Engineering* **54**(7):3491–3505.

X. Song, et al. (2019b). 'A dynamic model of the drilling action of percussive tools'. In *53rd US Rock Mechanics/Geomechanics Symposium*. OnePetro.

B. R. Stephenson (1963). *Measurement of dynamic force-penetration characteristics in Indiana limestone*. Ph.D. thesis, University of Minnesota.

A. Taheri, et al. (2016). 'Drilling penetration rate estimation using rock drillability characterization index'. *Journal of The Institution of Engineers (India): Series D* **97**:159–170.

X. Tan, et al. (1998). 'Application of the DDM and fracture mechanics model on the simulation of rock breakage by mechanical tools'. *Engineering Geology* **49**(3-4):277–284.

G. Tuomas (2004). 'Dynamic model of water driven rock drill hammer'. *Journal of Sound and Vibration* .

H. F. Unger & R. R. Fumanti (1972). *Percussive drilling with independent rotation*, vol. 7692. US Department of Interior, Bureau of Mines.

S. Wang, et al. (2011). 'Numerical simulation of the rock fragmentation process induced by two drill bits subjected to static and dynamic (impact) loading'. *Rock mechanics and rock engineering* **44**(3):317–332.

Z. Zhao, et al. (2014). 'Effects of Working Angle on Pneumatic Down-the-hole Hammer Drilling'. *Rock Mechanics and Rock Engineering* **48**(5):2141–2155.